Métamatériaux opto-électroniques

Quynh Le-Van

NNT : 2016SACLS082

THESE DE DOCTORAT
DE L'UNIVERSITE PARIS-SACLAY,
préparée à l'Université Paris-Sud

ÉCOLE DOCTORALE N° 572
Ecole Doctorale Ondes & Matière (EDOM)

IEF - Institut d'Electronique Fondamentale

Spécialité de doctorat : Optique et Photonique

Par

Quynh Le-Van

Métamatériaux opto-électroniques / Optoelectronic Metamaterials

Thèse présentée et soutenue à Orsay, le 3 Mars 2016 :

Composition du Jury :

M. GREFFET Jean-Jacques	IOGS, Univ. Paris-Sud	Président du jury
M. BOUHELIER Alexandre	LICB, Univ. Bourgogne	Rapporteur
M. COOLEN Laurent	INSP, UPMC	Rapporteur
M. EBBESEN Thomas	ISIS, Univ. Strasbourg	Examinateur
M. DEGIRON Aloyse	IEF, CNRS	Directeur de thèse

Abstract

A next generation of electronic and optoelectronic devices with high performances and low cost is expected to take off with colloidal quantum dots (CQDs) thanks to their unique electrical and optical properties. CQDs are semiconducting nanocrystals synthesized in solution that behave as artificial atoms. Substantial progresses in CQD film-based optoelectronics has been made over the past decade, but the performances are still limited and governed by the merit and inherited properties of CQDs. Another type of artificial medium, metamaterials, is generating a considerable interest from the nano-optics community because of its promises for beating the diffraction limit, realizing invisible cloaks, and creating negative refractive of index at optical regime. However, many of the potential applications for optical metamaterials are limited by their losses and the lack of active functionalities driven by electricity.

Although films of CQDs and metamaterials are studied independently and associated to two distinct fields, their properties are mainly determined by their inner geometry. In addition, the difficult hurdles from each field can be surmounted by cooperating with the other one. This dissertation establishes the first bridge to connect CQDs and metamaterials and is a first attempt at exploiting the synergy of different types of artificial media.

Firstly, we study plasmonic nanoantenna arrays capable of enhancing the spontaneous photoluminescence of CQDs and provide new fundamental insights into these interactions. Secondly, we report the fabrication and characterization of the first all-inorganic top-emission infrared quantum dot light-emitting-diodes (QDLEDs). The diodes are developed to serve as a solid platform for studying the CQDs film/metamaterial hydrids. Finally, we insert the plasmonic nanoantenna arrays studied at the beginning of this thesis in our QDLEDs and demonstrate a novel form of electroluminescence in which light is emitted by discrete nanoscale pixels that can be arranged at will to form complex light emitting metasurfaces. Other advantages associated with our metamaterial QDLEDs will also be presented i.e. greatly enhanced brightness, extremely low turn-on voltage, emissive color tunability, and polarized electroluminescence. A series of control experiments to probe the operational mechanisms of metamaterial QDLED will be discussed.

This demonstration illustrates the enormous synergy of combining different types of artificial matter and suggests that many other opportunities will arise by taking an unified view of the various artificial media developed in physics, chemistry and engineering.

Résumé

Les métamatériaux sont des composés artificiels permettant de réaliser des propriétés électromagnétiques n'existant pas dans la nature, ou alors seulement très difficilement réalisables avec des matériaux naturels. Parmi les nouvelles possibilités offertes par les métamatériaux, on peut citer les milieux à indice négatif qui inversent les lois de l'optique classique et permettent de réaliser des lentilles parfaites, des absorbeurs performants, et des capes d'invisibilité. Ces avancées spectaculaires ont été permises par le fait que les propriétés des métamatériaux ne proviennent pas uniquement de leur composition chimique, mais également de leur géométrie interne qui offre de nouveaux degrés de liberté pour la conception d'effets électromagnétiques innovants. Historiquement, les métamatériaux ont été introduits aux fréquences micro-ondes au début des années 2000 et se développèrent rapidement, tant du point de vue fondamental qu'applicatif. Ce dynamisme s'explique par le fait que les structures sont très faciles à fabriquer à ces fréquences (la taille des éléments du métamatériau doit être de l'ordre d'un dixième de la longueur d'onde, ce qui correspond à plusieurs millimètres dans le régime micro-onde), ce qui a permis aux chercheurs et ingénieurs de se focaliser uniquement sur la nouvelle physique et les applications. Petit à petit, la communauté s'est mise à développer des métamatériaux à des fréquences plus élevées, en régime Térahertz, puis en infrarouge (IR), et enfin en optique (proche IR et visible). Très vite, il est apparu que les enjeux en optique sont bien différents de ceux des basses fréquences : les structures sont extrêmement difficiles à fabriquer (nécessité d'avoir recourt à la nanofabrication en salle blanche), les matériaux utilisés dans leur composition absorbent considérablement plus, et il n'existe pas de stratégie pour fabriquer des métamatériaux actifs commandés électriquement. Il convient donc d'inventer de nouvelles approches et de nouvelles stratégies afin que les métamatériaux optiques réalisent leur plein potentiel. Le but de cette thèse est d'imaginer ce futur, en introduisant les tous premiers métamatériaux optoélectroniques. Comme nous le décrirons plus loin, ceux-ci seront obtenus en hybridant boîtes quantiques colloïdales (BQCs) et réseaux de nanoparticules métalliques d'or. Les BQCs sont des cristaux semiconducteurs synthétisés en solution déjà très étudiés en optoélectronique car ils offrent une alternative bas coût et de plus en plus performante aux semiconducteurs épitaxiés pour la fabrication de LEDs, de détecteurs et de cellules solaires. Dans ce manuscrit, nous montrerons comment transformer des LEDs BQCs conventionnelles en des métamatériaux ayant des propriétés optoélectroniques très innovantes. Après un premier chapitre d'introduction

résumant le contexte que nous venons d'esquisser, le deuxième chapitre de cette thèse est consacré à des études fondamentales sur les interactions entre réseaux de nanoparticules métalliques d'or et des BQCs en sulfure de plomb émettant dans le proche infrarouge dans la gamme 1000-1500 nm. Plus précisément, cette première partie est entièrement consacrée à la modification de la luminescence des BQCs dans une matrice diélectrique en présence des nanoparticules, c'est-à-dire l'effet Purcell. Il s'agit d'un phénomène très connu et qui consiste dans le fait que la densité locale d'états photoniques varie fortement au voisinage de nanoparticules métalliques. En particulier, les nanoparticules peuvent piéger le champ électromagnétique avec leur nuage d'électrons libres et former un mode résonant appelé résonance plasmon. A la résonance, la densité d'états photoniques est maximum, ce qui augmente le nombre de canaux radiatifs pour les émetteurs et donc leur luminescence. Dans cette thèse, nous avons apporté de nouvelles contributions fondamentales sur ce sujet en montrant par toute une série d'expériences que le modèle théorique généralement utilisé pour décrire l'effet Purcell ne s'applique pas au cas d'un ensemble de BQCs dans une matrice diélectrique en contact avec des nanaparticules, qui constitue pourtant l'un des systèmes les plus connus et les plus simples à fabriquer et à caractériser. Nous montrons en particulier qu'il est important de prendre en compte l'élargissement inhomogène des émetteurs ainsi que le fait qu'ils puissent émettre non seulement par recombinaison excitonique, mais également par des états de surfaces, deux paramètres non pris en compte dans le modèle précédemment évoqué. Notre thèse introduit un nouveau modèle développé par J.-J. Greffet permettant d'expliquer nos mesures. Nous avons ensuite appris à fabriquer des LEDs à BQCs en sulfure de plomb qui serviront de plateforme au développement de métamatériaux optoélectroniques à la fin de la thèse. Il s'agit d'une compétence qui n'était pas maîtrisée dans l'équipe. Le développement de ces LEDs, les difficultés que nous avons rencontrées et les performances des dispositifs finalement fabriqués font l'objet du chapitre 3 du manuscrit. L'architecture finale est un empilement comprenant une cathode en aluminium, une couche de transfert d'électrons en oxyde de titane, une couche de BQCs, une couche de transfert de trous en oxyde de molybdène et finalement une anode transparente en ITO. Les caractéristiques électriques des échantillons ont bien le comportement rectificateur que l'on attend d'une diode et nous avons vérifié que la lumière émise provient bien des boîtes quantiques. Nes structures commencent à émettre au-delà d'une tension de seuil de 5 ou 6 Volts environ, ce qui est un peu élevé par rapport à l'état de l'art. Cela s'explique par le fait que contrairement aux groupes reconnus dans le domaine, nous n'effectuons aucune étape de chimie pour optimiser les boîtes (tel qu'un échange de ligand) et que nous fabriquons tous les dispositifs sous at-

mosphère ambiante alors que la plupart des structures décrites dans la littérature sont élaborées sous atmosphère inerte. Néanmoins, nos LEDs sont stables dans le temps et reproductibles ; elles jouent en cela parfaitement leur rôle qui consiste à servir de point de départ pour développer les nouveaux métamatériaux optoélectroniques présentés dans le quatrième chapitre. Dans ce chapitre, nous montrons comment hybrider les réseaux de nanostructures métalliques étudiés au cours du chapitre 2 avec les boîtes quantiques colloïdales de nos LEDs, le tout pour créer un type nouveau d'électroluminescence artificielle. Celle-ci se traduit par l'émission de lumière par des nanopixels discrets composés des nanoparticules d'or et des BQCs qui les recouvrent. Les propriétés des dispositifs peuvent être contrôlées par la seule géométrie de ces pixels qui déterminent, à l'échelle nano, la plupart des paramètres d'émission et d'injection électrique (tension de seuil, spectre d'émission, brillance, contrôle total de la polarisation...). Ces pixels peuvent être arrangés de façon arbitrairement complexe afin de générer toute une gamme de fonctionnalités. De plus, les performances de ces dispositifs sont bien meilleures que nos LEDs du chapitre 3 puisqu'elles affichent des tensions de seuil à l'état de l'art mondial (moins de 1.5 V). Comme les pixels et leur espacement sont fortement sub-longueur d'onde, tout se passe comme si la lumière provenait d'une couche électroluminescente effective continue. Autrement dit, l'hybridation de BQCs et de nanoparticules métalliques répond bien à la définition d'un métamatériau puisqu'il s'agit de structures fortement inhomogènes dont la géométrie contrôle les propriétés mais qui, d'un point de vue macroscopique, se comportent comme un milieu actif continu. Pour illustrer les possibilités offertes par cette luminescence structurelle (c'est-à-dire contrôlée par la géométrie des nanopixels), nous avons notamment fabriqué une LED affichant deux mots différents selon la polarisation à travers laquelle on l'image. Nous avons également entrepris une étude systématique pour comprendre d'où provenaient ces propriétés nouvelles. De nombreuses expériences de contrôle ont été réalisées (comme par exemple supprimer la couche de boîtes quantiques, remplacer les réseaux de nanostructures d'or par des films d'or continus, varier l'épaisseur des couches d'injection de charges, etc...) qui ont toutes pointé vers une explication comprenant deux facteurs complémentaires : (i) le fait que l'électroluminescence soit exaltée par les résonances plasmon des nanoparticules d'or et (ii) le fait que la présence de ces nanoparticules induise des chemins de résistance moindre à travers l'empilement, ce qui favorise l'injection électrique. Le dernier chapitre de la thèse est consacré aux conclusions et perspectives offertes par ces travaux. Il est important de noter en particulier que tous les échantillons ont été fabriqués dans la salle blanche de l'IEF sans concours extérieur. Sur le court terme, il importera d'élucider plus finement les mécanismes à

l'œuvre dans les LEDs à métamatériaux présentées au chapitre 4, en particulier pour expliquer pourquoi l'incorporation de nanoparticules métalliques dans une architecture de LED modifie de façon si drastique ses propriétés électriques. Ces investigations passeront par l'élaboration de modèles numériques et théoriques ainsi que par des expériences de sonde locale (électroluminescence sous pointe STM par exemple) afin de mesurer plus précisément l'hybridation des boîtes quantiques avec les nanostructures métalliques. Il sera également intéressant d'étendre cette approche à d'autres applications telles que la détection, ce qui peut se faire en opérant les dispositifs en polarisation inverse. Plus généralement, ces travaux élargissent la notion de matière artificielle puisque nous avons combiné deux types de matériaux composites pour réaliser les métamatériaux optoélectroniques du chapitre 4—des réseaux de résonateurs plasmoniques et des boîtes quantiques colloïdales qui sont considérées comme des atomes artificiels en électronique. Ces travaux montrent donc tout l'intérêt d'une synergie entre différents types de milieux artificiels et nous espérons qu'ils seront à ce titre une source d'inspirations pour de nombreux autres domaines en dehors de la seule optoélectronique.

Acknowledgments

First I would like to express my sincere gratitude to the members of my thesis comitee: Professors Laurent Coolen and Alexandre Bouhelier who have accepted the role of rapporteurs and Professors Jean-Jacques Greffet and Thomas W. Ebbesen.

I would gratefully like to acknowledge the financial support from Ecole Doctorale Ondes et Matière during the time of this thesis.

This thesis could not be possible without the support from many people. First and foremost, I would like to express my deep gratitude to my supervisor, Aloyse Degiron, for his tremendous guidance, encouragement, and discussions.

Many thanks also go to great staffs at CTU for their terrific jobs of educating and assisting students to have the best conditions to work in cleanroom. Fabien Bayle for his assistance and instructions with SEM and EDX. Jean-René Coudevylle, Abdelhanin Aassime, and Xavier Le Roux for the helps and useful discussions of e-beam lithography. Abdelhanin Aassime and Antoine Martin for instructions to sputtering systems and your kind tolerance when I had made the most stupid mistake you have ever seen. David Bouville for cuting substrates. Nathalie Isac, Jean-Luc Perrossier, François Maillard, Marie-Paule Planté, and Cédric Villebasse for their assistance in thermal annealing, metal evaporations, electrical and mechanical characterizations.

I would like to acknowledge Professor Jean-Jacques Greffet for developing the theoretical frameworks explaining the experimental findings in Chapter 2.

I would like to express many thanks to Professor Niko Hildebrandt and members (Dr. Oya Tagit, Shashi Bhuckory, Xue Qiu, Dr. David Wegner) in his group for their generosity providing me chemical substances and access to his lab equipments.

Other past and present IEF members were helpful throughout this study. Dr. Tatiana V. Teperik for developing a simulation model in Comsol. Dr. Hong-Ha Cao and Heizi Zhang for helps in cleanroom. Dr. Maria Tchernycheva and Dr. Pierre Lavenus for their assistance with the cryogenic experiments.

Last but not least, I would like to grateful my family in Vietnam for their unquestioning love and supports.

Publication

1. Q. Le-Van, X. Le Roux, T. V. Teperik, B. Habert, F. Marquier, J.-J. Greffet, and A. Degiron. "*Temperature dependence of quantum dot fluorescence assisted by plasmonic nanoantennas*", Phys. Rev. B. **91**, 085412 – Published 12 February 2015. This article is a part of Chapter 2.

2. Q. Le-Van, X. Le Roux, A. Aassime, A. Degiron. "*Electrically driven optical metamaterials*", Nature Commun. in review, Submitted November 5, 2015. The results of this article are selected from Chapter 3 and Chapter 4.

dedicated to my parents: bố Quân and mẹ Đàm

my brothers and my sisters: Đoàn, Hoàng, Lệ, and Trang

Contents

Chapter 1

Introduction

Progresses in materials have always shaped the evolution of human civilization. The Stone, Bronze and Iron Ages were all defined by the most advanced materials of these eras. Quite early in modern human history, people have also successfully combined several materials so as to obtain new properties that Nature does not provide. The discovery of concrete during the Roman Empire, for example, had an important role for the expansion of the Empire through Europe. This composite comprised of cement, sand and aggregates was exploited in numerous constructions including the Roman Colosseum, the Pantheon and the Pont du Gard. Although the ancient concretes are very strong in compression, they are fragile due to poor tensile resistance. Modern concretes overcome this limitation by embedding steel bars or structural steel within concretes. This invention has transformed architecture and construction alike since the use of reinforced concrete is now ubiquitous and has enabled the construction of landmark buildings that would have been impossible to construct otherwise such as the Sydney opera house, the Christ statue atop the Corcovado in Rio de Janeiro, as well as the tallest building currently existing on earth, the Burj Khalifa tower (829.8 m in height) in Dubai [1].

There are of course many other examples of composite media that have transformed our life, from plywood to lightweight carbon fiber composites used in highly demanding environments (e.g. for aeronautic and space applications). In nanotechnology also, a

number of breakthroughs were achieved with the composite approach. Such is the case for example with the advent of efficient thermoelectric devices [2, 3, 4, 5], metamaterials that provide novel electromagnetic properties and composite semiconducting films made of colloidal quantum dots (CQDs). However, it is striking to note that each different subfield of nanotechnology and nanoscience develops its own artificial media without much regard to what other communities are doing. Although it can be understood by the fact that the physics, motivations and challenges of each specialty are very different, taking a unified view at artificial composite media would probably lead to very fruitful cross-pollination and radically new developments. For example, metamaterials have been introduced from the start as artificial media capable of exhibiting electromagnetic behavior not found in natural substances: this very idea of going radically beyond what nature has to offer does not seem to have permeated other research fields since composite media other than metamaterials are mainly developed to improve and/or leverage existing properties.

The goal of this dissertation is to establish a first bridge between different classes of composite media in nanoscience. To this aim, we will hybridize two well-known classes of artificial atoms–the unit cells of optical metamaterials and CQDs–and demonstrate in the last chapter of this dissertation how their synergy leads to novel and enabling optoelectronic functionalities. We have chosen optical metamaterials and CQDs because the former are artificial media for light while the latter are artificial atoms for electrons and holes: both play an important role in tailoring light-matter interactions and therefore appeared as good candidates for hybridization.

At the beginning of my PhD program, the metamaterial team that I joined at Institut d'Electronique Fondamentale had an established expertise in the design, fabrication and characterization of optical metamaterials but had only started to work with CQDs. Therefore, an important part of my thesis has been to develop the colloidal quantum dot experience of the group. As a result, I have not directly started to work on hybrid metamaterial/CQD optoelectronic devices and first performed a series of preliminary studies to understand how to manipulate CQDs and how they evolve over time, how to make

them interact with metallic nanostructures and how to pump them electrically. These progresses are described in chapters 2 and 3 of the present manuscript. Although they were conceived as learning steps, they also lead to new fundamental knowledge as we will see later.

In the remaining of this chapter, we will present the salient concepts pertaining to metamaterials and CQD-based optoelectronics. We then further discuss why we have chosen these two systems in the context of this study and finally present the outline of this thesis.

1.1 Metamaterials

1.1.1 Definition and historical aspects

The concept of metamaterial has been introduced after David R. Smith realized an artificial medium exhibiting a negative index of refraction in the GHz regime in 2000–a property that has never been observed in conventional materials [6]. Before elaborating on this discovery, it is important to note that the concept of artificial medium in itself was not new at the time. It can be traced all the way back to 1892 when Sir L. Rayleigh proposed an arrangement of spherical obstacles that behaved as if they formed a continuous medium [7]. A few years later, in 1898, Bose demonstrated artificial chirality at microwave frequencies using an assembly of twisted jute elements [8]. Progresses in artificial electromagnetic composites have experienced a growth after World War II, with the introduction of a variety of structures having artificial positive indices [9, 10], negative permittivities [11, 12] and even negative permeabilities without using magnetic media [13]. Most of these ideas were subsequently forgotten until John Pendry relaunched the whole field at the end of the 1990s with seminal papers on the wire medium with artificial negative permittivity [14, 15] and the split ring resonator medium with artificial negative permeability [16].

What makes metamaterials distinct from all the previous artificial electromagnetic

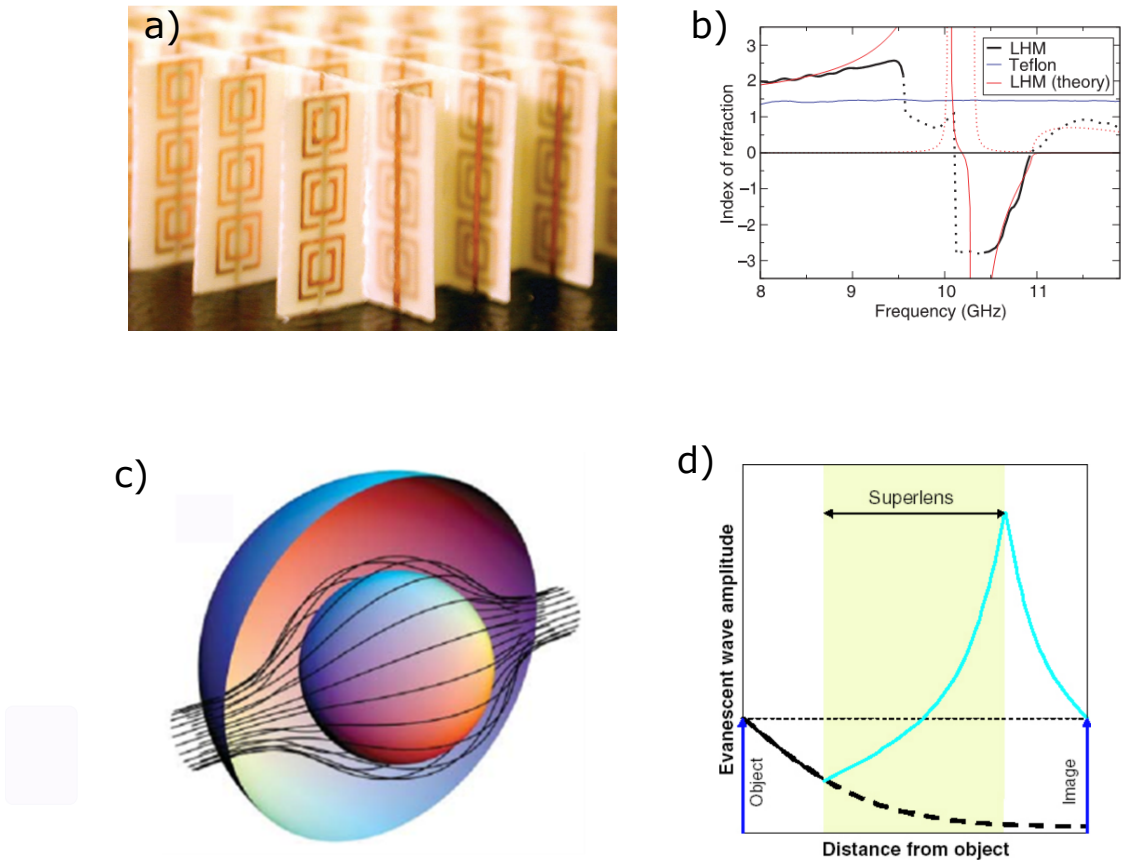

Figure 1.1: Experimental demonstration and potential applications of metamterials. a) A photograph of a metamaterial sample comprising square copper split ring resonators and copper wire strips on a fiber glass circuit board material [17]. b) The refractive index versus frequency of the corresponding metamaterials. c) Trajectories of rays in an invisibility cloak [18]. d) The principle of superlens [19, 20].

media is that they are capable of exhibiting properties that do not necessarily exist in nature. Such is the case for negative index media which were well understood theoretically by the time Smith made his discovery. In 1968, the theoretical physicist Victor G. Veselago realized that such media inverted all the laws of classical electromagnetism, leading to spectacular and non-intuitive effects. He noted for example that the phase and group velocities propagate in opposite directions (meaning that the electric field, magnetic field and wavevector form a left-handed triplet) and that convex and concave lenses had the opposite behavior of traditional positive index lenses. In addition, he showed that a slab of negative index substance was able to create an image of an object placed in its vicinity

[21]. The importance of this latter discovery was not fully assessed and understood until J. Pendry realized years after that the negative index slab acts as a perfect lens capable of restoring both the far field but also the near field of an object. Such are some of the few extraordinary properties of negative index media. However, Veselago noted at the time that his research was most likely to remain in the realm of theoretical curiosities since the condition to obtain a negative index medium was to have a material with simultaneous negative permeability and permitivity, which is something that do not happen in known natural substances.

The work of D. R. Smith in 2000 radically changed this vision. Following the prescriptions of Veselago, he constructed an artificial medium with an effective negative index at microwave frequencies by combining the wire medium (producing an effective negative permittivity) and split ring resonators (producing a negative permeability), which were both two types of artificial media recently rediscovered by Pendry in 1996 [14] and 1999 [16]. Soon after, he and others were able to experimentally demonstrate the many non-intuitive and spectacular properties of such structures, including negative refraction [6] and perfect lensing [19]. Figure 1.1a shows the picture of a negative index metamaterial comprising a copper Split-Ring Resonator (SRR) separated from a copper thin line by a spacer. This design allows one to obtain the negative refractive index at the gigahertz frequencies as shown in Figure 1.1b. The community soon realized that the metamaterial approach was a fantastic tool to expand the range of electromagnetic behavior and many new structures were introduced in addition to negative index composites. Figures 1.1c and 1.1d show the promising applications of metamaterials in realizing invisible cloaks and superlensing, respectively. In particular, it is relatively straightforward to fabricate microwave metamaterials with complex gradients in their permittivity and permeability tensors. Such possibilities have been exploited, among others, to demonstrate the first invisibility cloak in 2006 [18]. Other spectacular achievements allowed by metamaterials are hyperbolic media which, among others, exhibit a very high local density of photonic states [22, 23], as well as epsilon-near zero [24, 25] and chiral structures [26]. Those

breakthroughs, and many others have generated a considerable attention, to the point that metamaterials are now a sub-field of electromagnetism on its own right, with thousands of researchers around the world working in this specialty for both fundamental and applied purposes.

Most of the breakthroughs briefly discussed in the previous paragraph have been obtained at microwave frequencies. This spectral domain plays a special role for metamaterials because of the convergence of several fundamental and applied reasons. First, as in any previous artificial media demonstrated in the past, it is necessary that the inner structure of the metamaterial be much smaller than the wavelength, otherwise the structure does not behave as if it were a homogeneous substance. In this respect, the gigahertz range (1-20 GHz) is close to ideal for experiments: the wavelength is on the order of a few centimeters at most so the metamaterial unit cells do not need to be smaller than a few millimeters. Such dimensions are neither too big nor too small and therefore perfectly suited for tabletop experiments. Most designs introduced by the community rely on cheap and fast PCB technology, that is, by defining the metamaterial patterns in Cu-coated PCBs with a simple UV mask copier. Such elementary and fast technology has been key to explain the explosive growth of the metamaterial field since highly sophisticated electromagnetic behavior could be obtained with fabrication tools technically and financially available to everyone. Three other reasons explain why the gigahertz range has been privileged. First, the most interesting metamaterial responses are typically obtained with metallic resonators that exhibit very low losses at these frequencies. Second, experimental characterization can be performed with network analyzers that make it possible to measure both the amplitude and the phase of the electromagnetic wave. Last, there are many potential applications for metamaterials at these frequencies since it is a privileged band for a range of telecommunication and radar systems. From the beginning of the metamaterial adventure, the industry and military have been keen to collaborate with the academic laboratories to reap the many promises offered by this new generation of artificial media (super-lensing [27, 28], cloaking [29, 18, 30, 31], perfect absorbers [32, 33]

and other stealth technology, miniaturized antennas [34, 35].

There has also been a keen interest to extend the metamaterial approach to higher frequency regimes since many of the concepts initially demonstrated in the gigahertz range have been gradually adapted to THz, infrared and visible frequencies [36]. A first strategy initially pursued in all these regimes was simply to scale down the metamaterial structure so that it remains commensurate with the smaller wavelengths. It has proven very successful at THz frequencies, where archetypal metamaterial unit cells (i.e. metallic wires and split ring resonators) behave in much the same way as their lower frequency counterparts. However, the scaling law gradually breaks down as one increases the frequency up to the infrared and visible regime, mostly because metals become absorptive and transition from a conducting behavior (dominated by a large imaginary permittivity) to a lossy plasmonic behavior (dominated by a large real negative permittivity and significant absorption losses). Moreover, it becomes increasingly complicated to fabricate the structures as the frequency increases. In the infrared and visible part of the spectrum, in particular, the inner structure of metamaterials become sub-micronic, requiring elaborating nanofabrication tools. These challenges have pressed the community to come up with new designs and strategies adapted to these wavelengths as will be detailed in the following section.

1.1.2 Optical metamaterials

Figure 1.2a summarizes the progress in bringing the operating frequency of metamaterials to the visible spectrum for frequently investigated structures. In this figure, the operating frequencies of metamaterials with negative magnetic permeability μ (empty triangle) and negative index of refraction n (solid triangle) are shown on a logarithmic scale from microwave to visible wavelengths. Colors at the bottom of each image inset are the same color code as used for the triangle [36].

While fabricating 3D metamaterials is straightforward in the gigahertz range, the opposite is true for optical metamaterials due to the submicronic size of their inner con-

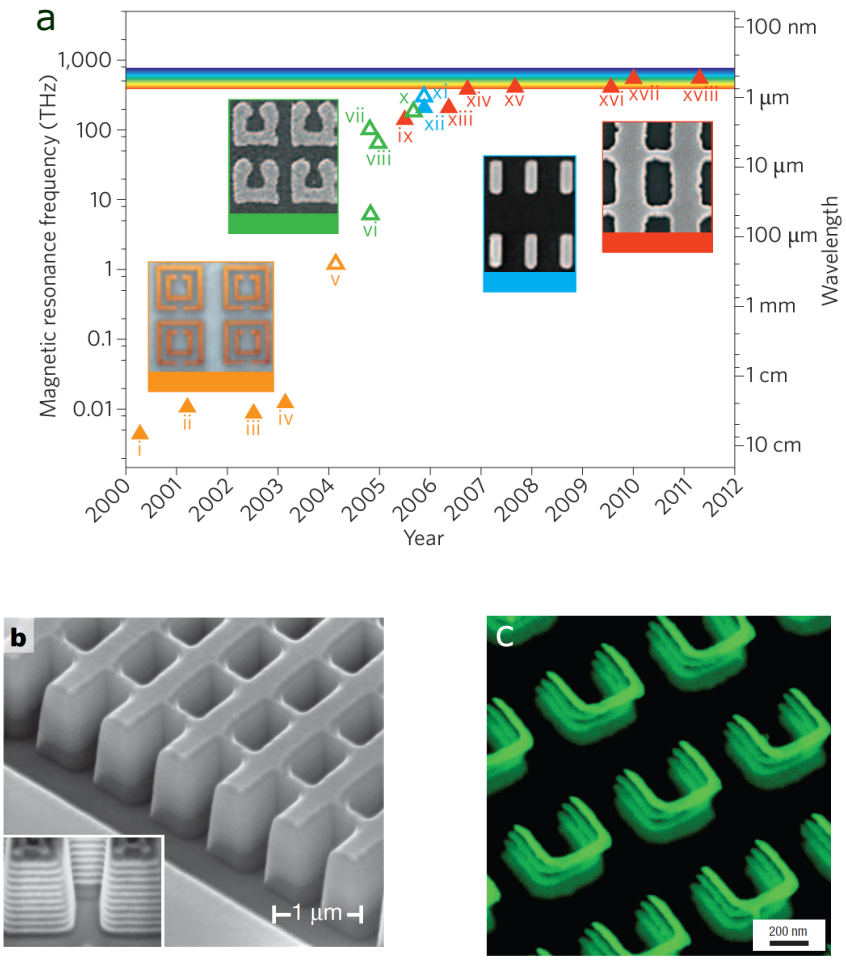

Figure 1.2: The progress in fabrication of metamaterials. a) The progress summary of operating frequency of 2D metamterials [36]. b) SEM of 3D fishnet metamterials containing 21 vertical layers exhibiting a negative refractive index n = -1.23 at 1775 nm [37]. c) SEM image of 3D optical metamaterials consist of four-layer SRR structure [38].

stituents. Conventional nanofabrication techniques such as focused-ion beam (FIB) and stacked electron beam lithography (EBL) have been privileged in early demonstrations [37, 38]. Figure 1.2b and 1.2c illustrates some examples of accomplished 3D metamaterials, i.e. cascaded fishnet structures [37] and stacked split ring resonators [38] that were fabricated by FIB and EBL, respectively. However, these techniques are often applied for small scale fabrication. To fabricate structures on a larger scale, it is necessary to consider other methods such as laser interference lithography [42] or nanotransfer printing [43]. Other useful approaches for fabricating 3D optical metamaterials include direct laser printing [44] (which is especially suited for fabricating chiral structures, although the min-

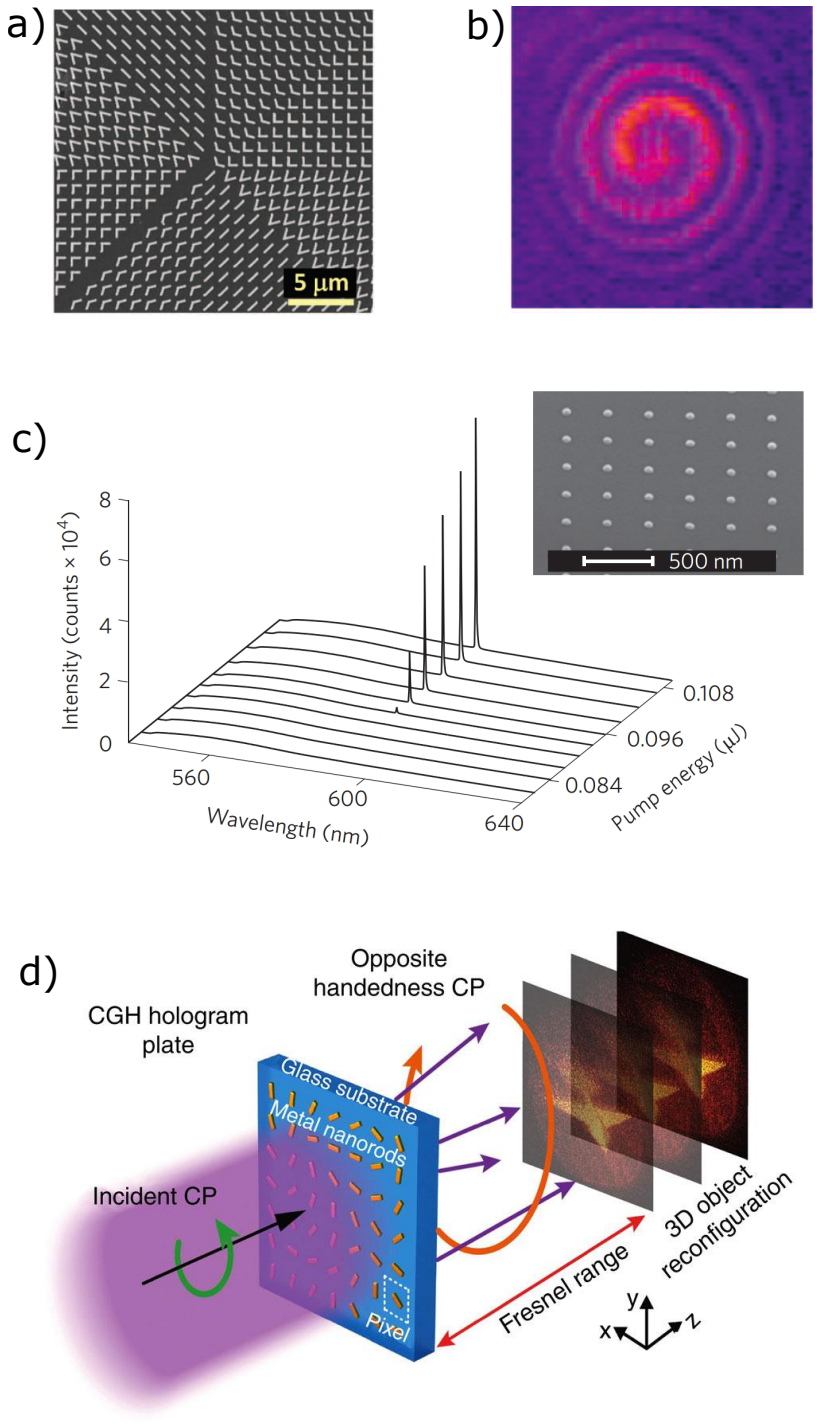

Figure 1.3: Two-dimensional optical metamaterials are used in a number of configurations. a) SEM image of a fabricated plasmonic metasurface that creates an optical vortex. b) measured spiral pattern created by the plasmonic metasurface [39]. c) Image of Ag nanoparticle array laser and its emission spectra with different pump pulsed powers [40]. d) A metasurface in with each meta-atoms is carefully placed and oriented to generate holograms.[41].

imum feature size is limited by the wavelength used for writing) as well as self-assembled techniques, for example by using block copolymers and metal electrodeposition [45].

Although significant achievements have been made for 3D optical metamaterials, their potential applications are hindered by several factors. This can be mostly ascribed to the persistent reliance on resonant metallic unit cells to produce interesting behaviors because metals are very absorptive at optical wavelengths. In addition, the fabrication of 3D optical metamaterials still faces many physical and technological challenges as explained above, and no one has ever demonstrated active structures driven by electricity–a much needed step towards practical applications. However, some of these problems can be alleviated by working with a single layer of optical metamaterial. Figure 1.3 shows a few examples of using a planar metallic surface for realizing a useful functionality. Figure 1.3a displays a metasurface comprised of metallic nanostructures placed deliberately in a certain order to show an effect of optical vortex, as illustrated in Figure 1.3b [39]. Figure 1.3c shows an image (inset) of Ag nanoparticle array laser. The lasing comes from the coupling of the diffractive plasmonic mode of the particle array and the Rhodamine 6G dyes and arises rapidly as the pumping power is increased [46]. Figure 1.3d shows a metasurface structure comprising carefully placed and oriented nanorods acting as a hologram plate to reconstruct a 3D image. Each metallic element of the metasurface, acting as a pixel, is encoded with computer generated hologram (CGH) to generate the desired continuous local phase profile under illustration of a circularly polarized (CP) light. By collecting only the transmitted handedness CP light in the Fresnel range, 3D image of the object can be reconstructed only with a single engineered metasurface [41]. Beside these examples, metasurfaces provide opportunities to modify the spontaneous emission of quantum emitters [47, 48] because each elements of the metasurface can be considered as an optical antenna.

1.1.3 Optical antennas

Optical antennas, analogues of microwave and radiowave antennas, are devices that provide an interface between freely propagating optical signals and confined photonic and/or electronic states. Most optical antennas are either dielectric or metallic resonators that localize energy in a certain region of space. Metallic antennas, in particular, have been the object of a keen interest because their resonances are highly confined modes that result from the coupling between the electromagnetic field and the free electrons of the metal [49, 50]. These so-called localized plasmonic resonances (LSP) can be sustained by virtually any type of metallic particles, including those of nanoscale dimensions, and are accompanied by very high local field enhancements in their immediate vicinity [51]. The excitation of a LSP considerably increases the local density of photonic states, providing additional radiative decay channels for quantum emitters placed in its proximity. As a result, the emitter can emit more photons than in the absence of the antenna. Moreover, these photons are not directly emitted in free space: rather, they are converted into LSPs that are eventually radiated back by the antenna so that the characteristics of the light emission are primarily those of the antenna rather than those of the emitter. The efficiency of this process depends on the losses of the system: all emitters are partially subject to non-radiative decays that generate phonons rather than photons. The presence of an optical antenna can substantially change the competition between these losses and the radiative decay rate, producing boosts in light emission than can even exceed 1000 for certain configurations [52, 53]. However, it should be reminded that this enhancement is also counterbalanced by the fact that a certain fraction of the energy carried by the LSPs is converted into heat rather than being re-emitted away from the antenna. For this reason, it is generally assumed that plasmonic antennas are all the more efficient than the emitter emits poorly in the first place. In the limit of a perfect emitter, free of non-radiative decay, the presence of a plasmonic antenna can only degrade the emission due to the introduction of losses in the system (note, however that we will challenge this affirmation in the case of an ensemble of colloidal quantum dots in chapter 2).

The mechanism described in the previous paragraph is a special case of a more general phenomenon discovered by Purcell in 1946 [54]. Before his discovery, it was believed that the ratio between non-radiative and radiative decays was an intrinsic property of an emitter. Purcell was the first researcher to realize that it was not the case and that the emission characteristics were directly influenced by the environment. The competition between losses and radiative processes is usually characterized with the so-called quantum yield $\eta_i = \Gamma^0_{\text{Rad}}/\Gamma^0_{\text{Tot}}$, where Γ^0_{Rad} is the radiative decay rate and Γ^0_{Tot} is the total decay rate, namely $\Gamma^0_{\text{Tot}} = \Gamma^0_{\text{Rad}} + \Gamma^0_{\text{Nonrad}}$. The quantum yield of an emitter in vacuum is known as the intrinsic quantum yield and the quantum yield of the same emitter in the presence of a inhomogeneous environment such as an optical antenna is called the modified quantum yield. The Purcell factor is defined as the ratio between the total decay rates in the presence and absence of the antenna. In the most simplest form, it is expressed as $f = 3Q\lambda^3/4\pi^2V$, where λ is the wavelength associated with the transition, Q is the quality factor of the resonator and V is its volume. In essence, this formula predicts that the Purcell effect will be maximized if the Q factor is high and/or if the volume of the antenna is small. In the case of a plasmonic resonator, the Q factor is very small, on the order of 2 [55] (as opposed to $\approx 10^6$ for the best dielectric cavities [56]). However, f can still be very high because the volume V of a plasmonic antenna is much smaller than the volume of a dielectric cavity. We note in passing that the definition of the volume V is somewhat problematic for a plasmonic resonator because the latter is an open cavity, with the field extending outside the metal boundaries. For this reason, there has been attempts at proposing a more rigorous definition of the Purcell factor in the case of plasmonic antennas [55, 57].

As a corollary of the Purcell effect, it is possible to design antennas that shape and/or polarize the light emission. This property arises because we have seen that light is not directly emitted from the source but from the LSPs sustained by the antenna. By exploiting plasmonic modes having well-defined radiation patterns, it is possible to radically alter the dipolar pattern typical of a point-source emitter, as was demonstrated with fluo-

rophores coupled with Yagi Uda antennas [58], split ring resonators [48], rings [59], Bull's eye antennas [60, 61, 62].

Last, optical antennas can also be used as a mean to boost the excitation of emitters pumped optically. In this operation regime, the plasmonic resonance is adjusted to the pumping wavelength. Because the excited LSP concentrates the incoming field, the local electromagnetic intensity at the location of the emitter is significantly enhanced compared with a pumping in free space. This mechanism is very efficient and most of the records in terms of spontaneous emission enhancements have been obtained in configurations in which optical antennas were primarily used as a mean to boost the pumping intensity. In the most general case, optical antennas can be designed for dual operation, i.e. for boosting the pumping intensity and for enhancing the emission through the Purcell effect [50].

The literature on plasmonic optical antennas can be dated from the late 1970s-early 1990s with experimental studies on the spontaneous emission of molecules above islandized metal films [63]. All the salient effects described above were already discussed at this time, at least in a qualitative way. There has been a renaissance of the field in the second half of the 1990s thanks to the advent of modern nanofabrication and nano-characterization tools. It has suddenly become possible to investigate single antennas or antenna arrays with well controlled shape and size, which constitutes a tremendous advance compared to the islandized metal films studied in the past that were obtained by arbitrary and ill-controlled nucleation in evaporation chambers. Two strategies were successfully applied to investigate the interaction between antennas and emitters: one approach consisted in fixing a nanosize antenna at the tip of an AFM probe and study the interaction between this resonator and a surface with adsorbed fluorophores [64]. The second approach was relying on fabricating well-defined samples by mean of electron beam lithography [65, 66]. In these samples, the fluorophores were either randomly distributed around the antennas or placed in well-defined positions by embedding them in a patterned resist. Throughout the years 2000s, both strategies led to major results both in terms of light enhancement,

beam shaping and advances in the fundamental understanding of light manipulation at the nanoscale and new developments are still regularly published these days [67]. It is worth noting for example that there has been very recent reports on optical antennas acting as a direct interface between light and electricity without mediating the exchange through a fluorophore [68, 69].

In this context, it is little wonder that the field of plasmonic antennas has crossed the path of optical metamaterials: as explained earlier, most optical metamaterials and metasurfaces operate with subwavelength metallic inclusions which, when they become resonant, sustain LSPs that can be used for tailoring the spontaneous emission of point-like sources. For this reason, there have been studies in the literature in which the emission of fluorophores has been enhanced with plasmonic metamaterials [48, 70]. However, there is an ambiguity in these studies because the Purcell effect that they exploit is intrinsically a near-field phenomenon, as explained above. In this regime, the metamaterial structure does not behave as an effective homogeneous medium for the fluorophores: it is indeed the individual LSPs on each metallic inclusion that are responsible for the enhancement rather than a hypothetical effective response of the whole structure. In other words, a given structure can be a genuine metamaterial that behaves as an effective homogeneous medium in a certain context (e.g. when it interacts with a plane wave) and as a highly inhomogeneous structure in other contexts (e.g. for the Purcell effect). For a plane wave, a genuine metamaterial behavior arises when the period and size of the metallic inclusions are very small compared to the free space wavelength. In the reciprocal space, it is equivalent to say that the first Brillouin zone of the structure must be very large with respect to the free space wavevector. Clearly, such condition is typically not satisfied when a metamaterial is used for enhancing the spontaneous emission of fluorophores because it relies on near-field effects that include wavevectors that are much larger than the free space wavevector. To the best of our knowledge, this ambiguity is never discussed in the literature: the term metamaterial (or metasurface) is often used with the same meaning as plasmonic antenna array while in the strictest sense the two expressions do not denote

the same thing. A plasmonic antenna array can act as a metamaterial (or a metasurface) when homogenization conditions are met but this is usually not the case when it is used to enhance the spontaneous emission of fluorophores. In this dissertation, we will take a special care to avoid the confusion: in chapter 2, for example, we will study the interaction of colloidal quantum dots with nanoparticle arrays outside the homogenization regime so we will not call these structures metamaterials. In chapter 4, we will explain why the same structures used in a different context can be considered as genuine metamaterials.

1.2 Quantum dots

The second artificial medium that I have studied during my thesis is colloidal quantum dots. Quantum dots (QDs) are defined as a semiconductor nanocrystals with all the dimensions comparable with or smaller than the exciton radius of its respectively macroscopic semiconductor. One of the most remarkable properties of QDs is their size-dependent optical properties discovered independently in the early years of 1980s by Ekimov *et al*, Henglein, and Brus [71, 72, 73]. In these studies, they found that the color of nanocrystals strongly correlates with their size.

1.2.1 Quantum Confinement Effect

The size of QDs is generally in a range of 2-10 nm in diameter, corresponding to a few hundreds to a few thousands of atoms. The size dependence of their optical properties originate from quantum confinement effect which causes a discreteness of the energy levels for the carriers in the QDs. In a ideal spherical nanocrystal surrounded by a infinite potential barrier, the energy levels of electron and hole, characterized by angular momentum quantum number l, can be obtained by solving the Schrödinger equation of the carrier in a three-dimensional box [74]:

$$E_{l,n}^{e,h} = \frac{\hbar^2 \phi_{l,n}^2}{2m_{e,h}a^2} \tag{1.1}$$

where $\phi_{l,n}$is the n^{th} root of the spherical Bassel function of the order l, $j_l(\phi_{l,n}) = 0$, $m_{e,h}$ is the electron and hole effective mass, respectively, and a is the radius of the nanocrystal. Although Equation 1.1 indicates that the allowed energy levels of quantum dots become quantitized as the size of the dots reaches nanoscale dimensions, adding or subtracting a single atom to the quantum dots is unlikely to change these energy levels. Consequently, quantum dots are regarded as artificial atoms, a class of intermediate materials between bulk semiconductor and atoms since they own the characteristics of a small crystal and those of a large ensemble of atoms as illustrated Figure 1.4 [75].

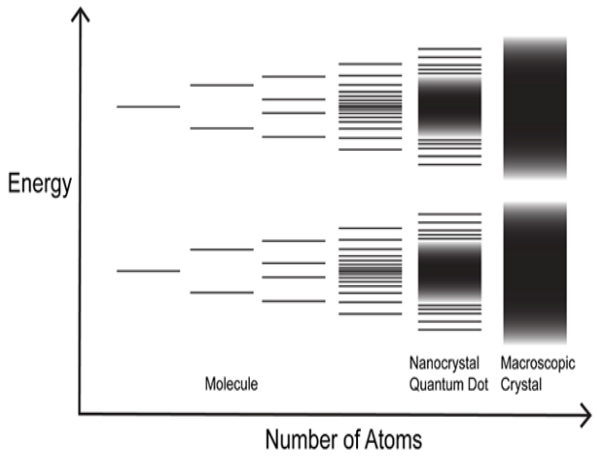

Figure 1.4: QDs with a small number of atoms show discrete energy levels. As the number of coupled atoms increase, energy levels become more densely packed, eventually forming bands in macroscopic crystals. Reproduced from Ref [75].

The energy between the lowest electron and hole levels increases with decreasing nanocrystal size leading to an increased total energy of band edge optical transitions. For example, figure 1.5 shows that the bandgap of PbS quantum dots is increased by 1.4 eV as the dot dimensions diminishes from 10 nm to 2 nm. However, the quantum confinement effect is not the only factor that determines the optical properties of the nanocrystals. When electrons and holes are generated in the nanocrystals, the optical properties of the nanocrystal will also depend on the Coulomb interactions since the carriers exist within the same volume. While quantization energy varies as a function of $1/a^2$,

the Coulomb energy is only proportional to $1/a$; hence, the impact of Coulomb interaction on the optical properties is relatively small to small nanocrystals and becomes bigger for large nanocrystals. Theoretical analysis shows that the optical properties of nanocrystals depend on the ratio between a and a_B, in which a is the radius of the nanocrystal, and a_B is the Bohr radius of the exciton defined as $a_B = \hbar^2\kappa/\mu e^2$ with κ is the dielectric constant of the semiconductor and μ is the reduced mass of the exciton. For the PbS quantum dots that will be used throughout this thesis, the exciton Bohr radius is 20 nm. This value is much larger than the typical radius of PbS quantum dots (2-4 nm), hence they are categorized in strong confinement regime [76].

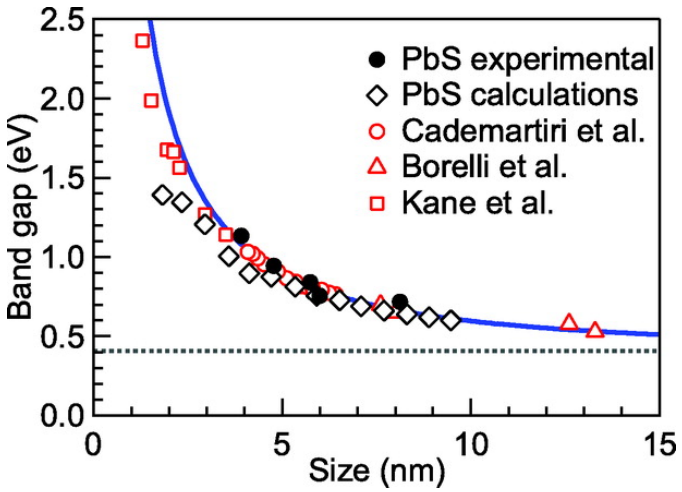

Figure 1.5: Relation between the PbS quantum dot bandgap and the particle size. The experimental data (•), tight-binding calculations (◇), and compared with literature works ([77] (*O*), [78] (△), [79] (□)). The blue line is a fitted sizing curve and the dotted line denotes the bulk PbS bandgap, E_g(bulk) = 0.41 eV. Reproduced from Ref [80].

In a strong confinement regime, when $a \ll a_B$, the optical properties of nanocrystals are primarily determined by the quantum confinement effect with a minor perturbation from the Coulomb interaction. In this case, the selection rules governing the interband transitions between lowest electron and holes levels requires the same quantum numbers

to be transitionable between levels. Hence, the absorption spectra are given by[74]:

$$\hbar\omega_\nu = E_g + E_v h(a) + E_v^e(a) - 1.8\frac{e^2}{\kappa a} \tag{1.2}$$

where E_g is the energy bandgap of the bulk semiconductor, E_v^e and E_v^h are the electron and hole energy level, respectively. The Coulomb correction is calculated in first order perturbation theory since in this regime it has a modest contribution factor on the energy bandgap expansion.

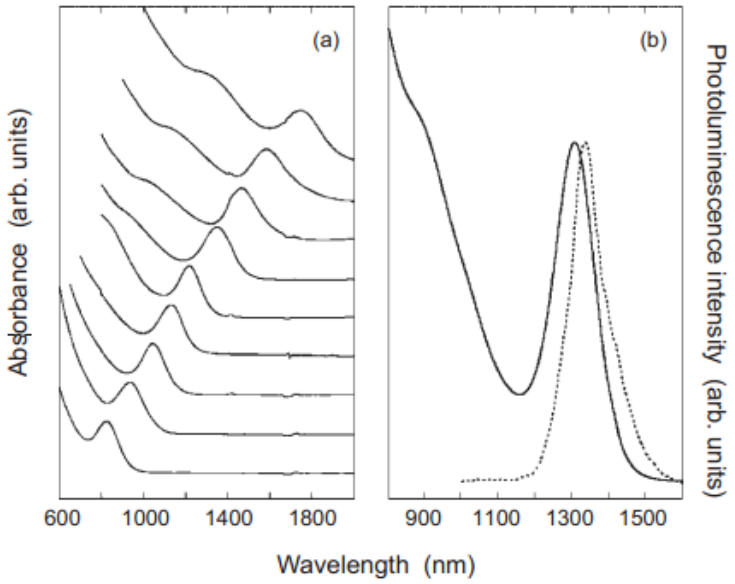

Figure 1.6: Room-temperature optical characterization of PbS QDs in toluene solution. a) Absorption spectra spanning the range of tunable sizes. b) Band-edge absorption and photoluminescence peak for a sample of average ≈ 6.5 nm in diameter. Taken from Ref [81].

Equations 1.1 and 1.2 have showed that the bandgap of colloidal quantum dots is dependent of the size of the dots. Figure 1.6 illustrates the size dependence of optical properties of nanocrystals. In this figure, the absorption peak shifts to lower energy as the size of the dots increases. One can also note that the photoluminescence (PL) spectra are red-shifted with respect to the first absorption peak, a phenomenon called Stockes shift that is ascribed to the energy difference between the first bright exciton and dark

exciton [74].

It has been shown that the PL spectral peak of nanocrystal ensembles is determined by the main size of the whole quantum dots solution, yet its spectral breadth is not always dictated as the combination of the sample inhomogeneity and spectral linewidths of the single nanoparticles. Recent work has proved that while the linewidth of each single nanocrystal of different materials are nearly identical (50-60 meV), the inhomogeneously broadened PL linewidth of the nanocrystal ensembles varies from material to material [82, 83].

The chemical composition of QDs is also the critical factor determining their radiative lifetime. For example, the radiative lifetime of CdSe quatum dots $\tau_R \approx 20$ ns [84], whereas fluorescence lifetime of PbS is two orders of magnitude longer $\tau_R \approx 1\mu$s [85]. There are several interesting phenomena associated with optical properties of colloidal quantum dots such as photoluminescence intermittency (blinking) [84, 86, 87], but it will not be discussed in this thesis.

1.2.2 Growths of quantum dots

QDs can be formed by a variety of techniques and from different materials. Growing QDs inside glass matrices is one possible way [88, 89]. This method relies on diffusion of semiconductor ions during annealing process where the ions with opposite signs combine and form a nucleus that continues to grow in size as a function of annealing duration. An acceptable monodisperse size distribution can be achieved via this method, yet large energy consumption and slow growing pace are the main drawbacks of this technique.

Another method to grow QDs has been the object of many studies, that is, molecular beam epitaxy (MBE) [90, 91, 92]. The principle of this technique is based on exploiting self-organization and island-like growth within the first deposited monolayers. In ultrahigh vacuum systems, atoms from ultrapure substances impinge upon the substrate, diffuse across the surface, form a cluster with other atoms which gradually coalesce and develop towards two-dimensional monolayers. These monolayers are called wetting layers. Further

layers of atoms are added on the wetting layer that becomes increasingly strained (due to the lattice mismatch) to the point that they break apart and form islands, or quantum dots in our case. These quantum dots have typically a pyramid-like shape with the height of the dots being less than 10 nm but the base of the dots is generally longer than their height. Although MBE is suited for studies requiring in situ characterizations, it owns a number of drawbacks such as the need for appropriate substrates, high fabrication costs, broad size distribution, and low surface densities.

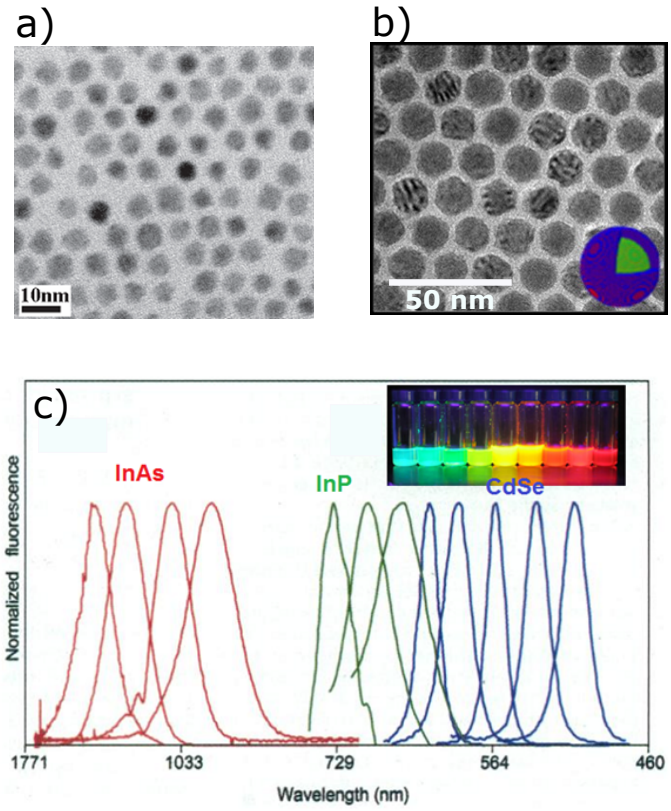

Figure 1.7: Photoluminescence emission color depends on the size of QDs. a) TEM image of PbS quantum dots suspension with a mean size equals to 5.7 nm [80]. b) TEM image of PbSe-PbS core-shell quantum dots produced in large scale synthesis with mean size distribution smaller 10% [93]. c) Normalized photoluminescence of different quantum dots compounds emitting from UV to NIR. Each QD compound can tune emission in a certain range of wavelengths, inset is the picture of different colors of the solution corresponding to different size CdSe solutions under UV light [94].

Most of these limitations can be overcome by employing solution phase chemical methods [95, 96, 97]. Colloidal Quantum Dots (CQDs) synthesized by chemical reactions have

become a common practice for making quantum dots thanks to their ease of manipulation and wide range of applications. The chemicals used for synthesis are typically organometallic precursors and their reactions take place in solution. As a result, the prepared quantum dots can be suspended in either polar or nonpolar solutions depending upon the preparation procedures. A good advantage of CQDs prepared by this technique is that their shape and size can be controlled easily and, in general, the dots appear in a nearly spherical shape, as shown in Figure 1.7a and 1.7b. Compared to the above mentioned techniques, dots by chemical synthesis are characterized by better monodisperse size distribution, faster and low-cost preparation, and especially they are compatible for a wide range of research and applications. On the other hand, CQDs are surrounded by organic ligands that contribute to complicate the physics of these objects. In particular, they contribute to complex surface states that are responsible for unwanted effects such as non-radiative exciton recombination by e.g. Auger effects.

1.2.3 Applications of colloidal quantum dots

Although many researches are conducted for fundamental studies, a belief in potential for many applications drives CQDs research beyond chemistry societies. CQDs can be blended in a number of materials and live tissues and also self-arrange into solid granular films, offering a range of applications from biology to solar cells.

In biology, CQDs can compete with more conventional fluorophores for imaging purposes [98, 99, 100] due to their superior brightness [101] in the two bio-windows regimes [102](the first window: 650 nm to 900 nm and the second window: 1000 nm to 1350 nm) where the tissues scatter and absorb light the least. Although CQDs are usually made of toxic materials, they are embedded in a protective shell that makes them compatible to living tissues. CQDs are also increasingly investigated in engineering sciences: for example, they are used to harvest small amounts of energy in thermoelectric devices [93] and to improve the electrochemical properties of electrodes for rechargeable batteries [103, 104, 105].

But one of the most interesting features of CQDs is the fact that they can form compact granular semiconducting films by simple coating techniques. In fact, most CQD films studied so far were obtained by spin-coating a liquid solution of CQDs on a variety of substrates. Such composite films can advantageously replace bulk semiconductors as they do not require expensive processing steps such as MBE. In addition, they offer an unprecedented flexibility of design because their semiconducting properties do not only depend on their chemical composition, but also on their shape, size and local arrangement. In other words, the geometry plays an important role in their properties, in a similar way as what we have seen for optical metamaterials. Among the advantages offered by CQD films is the possibility of forming complex heterojunctions of various bandgaps by superimposing several layers of CQDs with different diameters. Also, it is easy to fabricate CQD films with bandgaps adjusted for near-infrared applications whereas conventional optoelectronic devices are typically very expensive in this frequency range (e.g. InGaAs or MCT detectors).

Over the past 15 years, CQD-based electronics and optoelectronics have gained a considerable popularity. CQD films are being investigated in the context of light emitting diodes (QDLEDs), solar cells, photodiodes and photodetectors. Quantum dot light-emitting-diodes (QDLEDs) are showing high efficiency with superior color quality [106, 107]. High-quality QDLEDs have in turn opened a new generation of display devices with large-size flexible panels, longer lifetime, and low-power consumption [108, 109]. Photodectors based on CQDs show outstanding sensitivity and resolution [110, 111, 112]. CQD films with infrared bandgaps are capable of matching most of the sun's spectrum reaching Earth with high absorption efficiency [113]. The first solar cells based on CQD films demonstrated in 2005 [114], reached efficicency 5% in 2009 [115], and rising to 9.9 % in 2015 [116]. Most of these breakthroughs have not yet reached the consumer market but it is worth noting that high-tech giants such as Samsung, Sony and Siemens are active players in this international competition, highlighting the huge potential of CQD films.

Despite these advantages, CQD films also suffer from limitations on their own. CQDs

are surrounded by insulating organic ligands that are good for avoiding aggregation and making them solution processable. However, in CQD films, ligands create insulating interstices amid CQDs that result in a poor electrical conductivity. This is one of the major causes limiting the performance of CQD-based devices. Researchers can reduce the distance between the dots to enhance the charge transport by performing ligand exchange in solution or post-deposition. However, recent studies have shown that ligand exchange modifies the energy levels of the quantum dot film [117], therefore it might be difficult to apply a universal technology protocol to fabricate all the desired devices. In other words, each film of quantum dots with a certain ligand type requires a specific architecture to maximize the performance of the devices.

1.3 Two artificial media with common and complementary properties

Both optical metamaterials and CQD films have this in common that their properties are not solely defined by their chemical composition, but also by the size, shape and arrangement of their inner constituents, offering enormous advantages to design complex structures (Figure 1.8). On the other hand, they are both afflicted by severe limitations that prevent them from fulfilling the largest part of their promises.

A first motivation to combine these two objects comes from the realization that the drawbacks of CQD films may be minimized with optical metamaterials and vice-versa. Because optical metamaterials made of metallic inclusions are very good at concentrating light fields, they may solve some of the limitations of CQD-based devices related to the production or detection of light. Inversely, CQD-films are active media that may, if not suppress the ohmic losses of metallic metamaterials, provide tunable and/or electrically-driven functionalities that would bring these structures a step closer to practical applications.

But perhaps the main reason as to why we chose to study metamaterial/CQD hybrids

is that metamaterials and CQDs are each excellent model systems of artificial matter: the former are effective atoms for light, the latter are effective atoms for electrons, both offer new opportunities to tailor light-matter interactions, so they appear as natural candidates to generalize the concept of artificial media in optoelectronics.

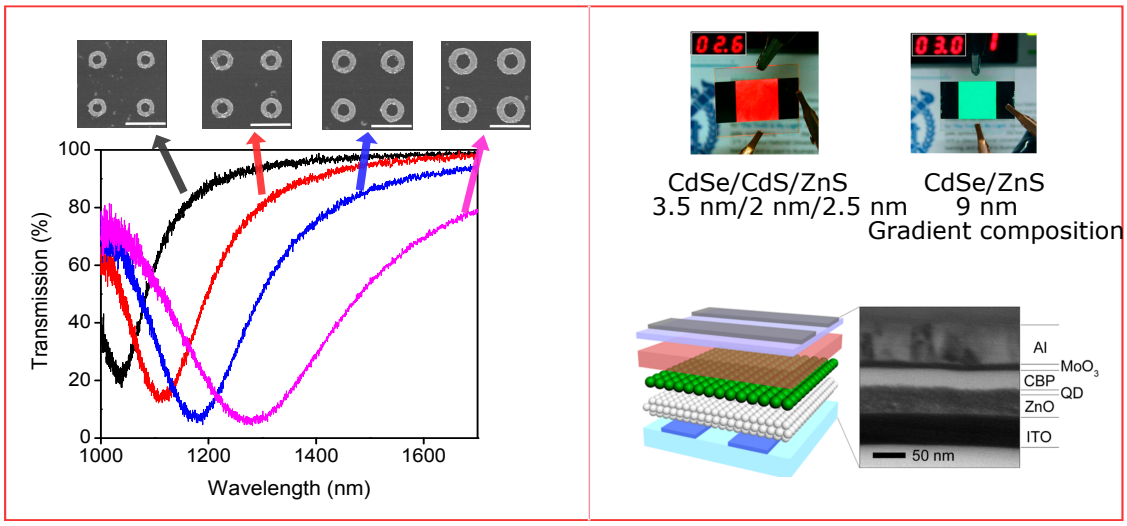

Figure 1.8: Concept similarity between the two artificial media. (Left) The functions of metamaterials determined by the size of inner geometry. White scale bar: 500 nm. (Right) The luminescence color of QDLED is determined by size of quantum dots [118].

1.4 Overview of the next chapters

The ultimate goal of this dissertation is to show the synergy of hybridizing different classes of artificial matter in optoelectronics. To this end, we will focus on LED architectures and demonstrate a new form of artificial electroluminescence. Before reaching this goal, it has been important to learn how to work with CQDs (the expertise of the team on this subject was limited at the beginning of my thesis), understand how these objects interact with metallic nanostructures and how to pump them electrically. These intermediary steps are explained in chapters 2 and 3.

In chapter 2, I will study the interactions between plasmonic nanoparticle arrays and colloidal quantum dots embedded in a dielectric host matrix. To gain insight, we have

performed photoluminescence experiments in which we have varied all the relevant parameters, including the distance between the CQDs and the plasmonic nanoparticles, the optical excitation power and the temperature of the system. We will show that our experimental results challenge the predictions of the two-level model that is usually invoked to understand such systems and present a new theoretical framework developed by Prof. Jean-Jacques Greffet to account for our findings.

The third chapter focuses on the fabrication of CQD films and near-infrared light emitting diodes (QDLEDs) operating with PbS CQD films. Contrarily to most QDLEDs developed in the literature that produces light through a transparent substrate, we propose an architecture that emits through the top of the structure in order to have a system compatible with our experimental setup and the final goals of our thesis.

In the fourth chapter, we will finally introduce a new type of QDLEDs in which a hybrid CQD-metamaterial layer plays the role of the active media. This hybrid layer is obtained by combining the nanoparticle arrays studied in chapter 2 with the CQD films used in chapter 3. We will explain why, in this case, the ensemble acts as an active metasurface that can be tailored at will to emit complex light patterns. We will also show that the coupling with the metallic nanostructures significantly improves the optical as well as electrical properties of the CQDs, to the point that we have been able to set a new world-record low threshold voltage for QDLEDs operating with PbS quantum dots.

Finally, chapter 5 will summarize the key results of this thesis and discuss outlooks and future directions that can be beneficial from this study.

Chapter 2

PbS CQDs coupled with metallic inclusions

To accomplish the goal of this thesis demonstrating a hybrid device bringing the gap between optical metamaterials and CQD films, we have divided our work into smaller aims. The fabrication and characterization of optical metamaterials was mastered in our group before I arrived, but the expertise of manipulating and understanding CQDs was limited. Our first aim was therefore to learn how to work with CQDs and how to control their emission with arrays of metallic inclusions. This task is the central discussion in this chapter. Figure 2.1 illustrates the side view of the full sample that will be used to study the interactions between the plasmonic nanoantennas and CQDs. The sample consists of arrays of nanorings fabricated on glass substrate, a layer of SiO_2 acting as a spacer, a layer of PbS CQDs doped hydrogen silsesquioxane (HSQ), and finally a pure HSQ layer on top. This figure is presented only for the introducing purpose of the system that will be the core discussion in this chapter, details on how the layers are made will be presented later when they are needed. Although similar systems have been studied [47, 48], here we thoroughly investigate the interactions between CQDs and plasmonic nanoantennas with respect to a number of conditions from the distance between the nanoantennas and CQDs, the optical excitation power, the influence of temperature on the interaction, and

the stability of the interaction over the time.

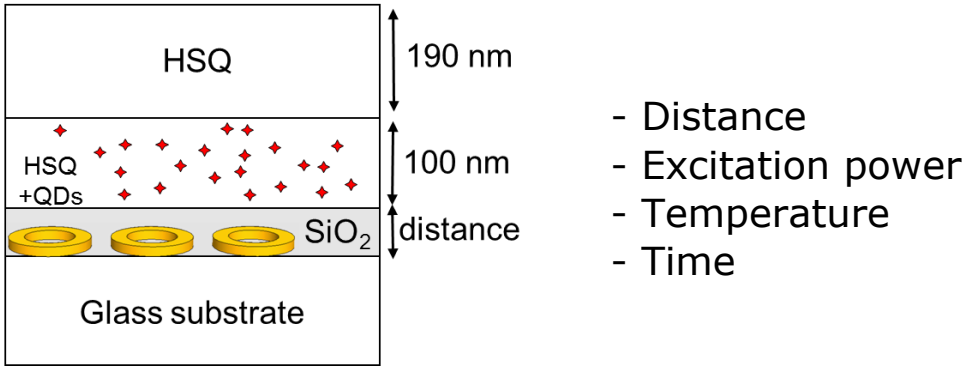

Figure 2.1: Schematic of the full sample used to investigate the coupling between plasmonic nanoantennas and quantum dots. A thorough study will be conducted as a function of several parameters: distance between the nanoring arrays and layer doped with quantum dots, excitation power to the system, temperature, and time.

This chapter starts with a study of the essential photoluminescence characteristics of PbS CQDs as they are embedded in a dielectric host matrix. Physical properties of plasmonic nanoantennas are also presented before they are coupled in a single sample. We then introduce the mainstream theoretical model used in the literature to describe the coupling between plasmonic nanoantennas and CQDs and show with a series of experiments that this model is not adapted to our system. Finally, the last part of this chapter presents a new theoretical framework to qualitatively account for the new findings.

2.1 Experimental setup for micro-PL measurement

The study in this chapter is conducted mainly through PL measurements regardless of the parameters varied. Figure 2.2 sketches the micro-PL setup used throughout this chapter to collect the PL signal. The laser source utilized for the measurement is He-Ne laser (Melles Griot) emitting a continuous (CW) red laser light at 632.8 nm with a maximal power of 3 mW. The wavelength of the laser light provides a suitable energy not only for high non-resonant absorption of CQDs but also for avoiding the Auger ionization and multi-exciton generation [119] - the two mechanisms that degrade the PL quantum

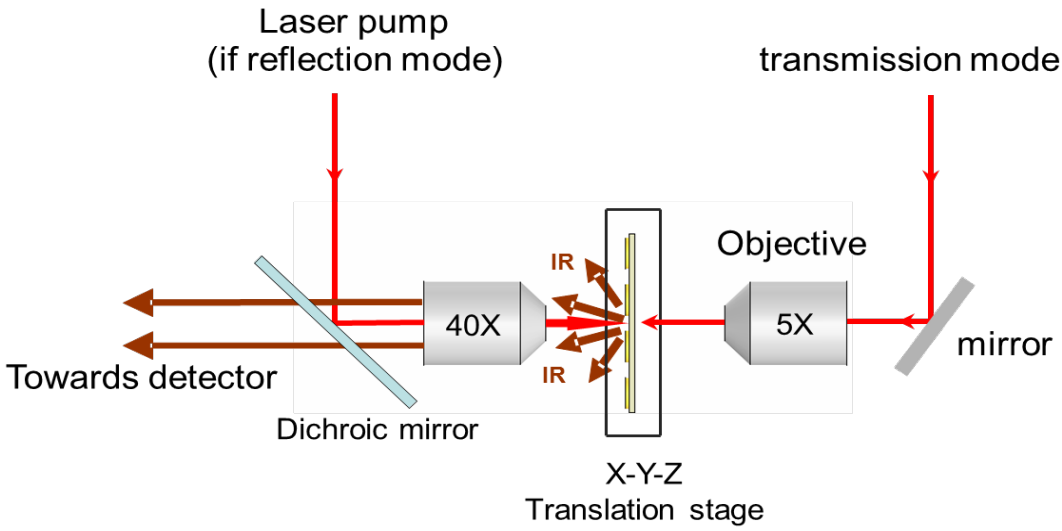

Figure 2.2: Schematic of micro-Photoluminescence measurement. This setup allows to focus the laser beam in transmission mode (5X objective used) and in reflection mode (40X objective used). A dichroic mirror is placed just behind the 40X objective to select the infrared signal of the sample and direct it toward the detector. In addition, this setup allows to vary the temperature of the sample with He liquid flow.

yield of CQDs. This setup is built to record signal in both transmission and reflection modes. In transmission mode, the light is focused through the glass substrate with 5X objective and collected by a higher numerical aperture objective (40X, Nachet, N.A. = 0.6), whereas in reflection mode the light is focused and collected from the surface of the sample by only one objective (40X). Regardless of the measurement mode, the infrared signal from the sample is collected by a 40X objective; hence, the spectral features do not change as one switch back and forth from transmission and reflection collection modes. The IR photoluminescence signal from the sample is separated from visible laser light with a dichroic mirror and directed towards a monochromator (Jobin Yvon iHR320) and an InGaAs detector (Jobin-Yvon Symphony II). Samples are attached to a movable stage so as to mechanically transit it in three directions, x, y and z. In the case of temperature-dependent measurements, the sample is inserted inside a Helium flow cryostat (Oxford Instrument MicrostatHires2) attached to a translation stage so that the laser beam can shine in any spot onto the sample. It is noted that because the sample is mounted in a

cryostat for varying the temperature, it is only possible to perform the recording in the reflection mode.

2.2 PbS CQDs in a homogeneous medium

As mentioned in the previous paragraph, it is crucial to understand basic characteristics of CQDs before we study their interactions with the plasmonic nanoantennas. This section presents PL properties of CQDs embedded in a host matrix response under different conditions to which they have to be exposed frequently. It includes monitoring the evolution of the PL properties of CQDs over the time, with different pumping powers and different temperatures.

The quantum emitters used through the study are PbS CQDs purchased from commercial company Evidot Technologies. They are suspended in Toluene solution at concentration 30 mg/ml. The diameter of the dots is 5 nm on average and they are surrounded by 2 nm long of ligands.

The commercial batch of PbS CQDs is diluted in toluene until it reaches a 5 mg/ml concentration. The PbS QDs in glass matrix are prepared by mixing PbS QDs at 5mg/ml with a hydrogen silsesquioxane (HSQ) based resist (XR1541 electron-beam resist, Dow Corning) and methyl isobutyl ketone (MIBK, MicroChem). The final solution of PbS QDs (1 mg/ml) is then spincoated on a glass substrate and baked at 150 °C for a few minutes to achieve a 100 nm thick layer. A layer of SiO_2 sol-gel (190 nm) was added by spincoating the pure XR1541 resist and a soft bake at 150°C on top of the CQDs doped matrix so that PbS QDs experience a symmetric environment with the refractive of index is nearly identical, as illustrated in Figure 2.3a. It is noted that at this stage, it is not highly necessary to add a thick layer of pure SiO_2 sol-gel because we still measure a significant signal without the presence of this layer [120]. However, this thick top layer of SiO_2 sol-gel will play a critical role when the dots are coupled with the nanorings structures, as will be discussed in more details in Section 2.4.

2.2.1 Photoluminescence of PbS CQDs a host matrix

The first characterization of CQDs embedded in a glass matrix is the measurement of the evolution of their PL characteristics. The sample as illustrated in Figure 2.3a will be stored in air and measured over time.

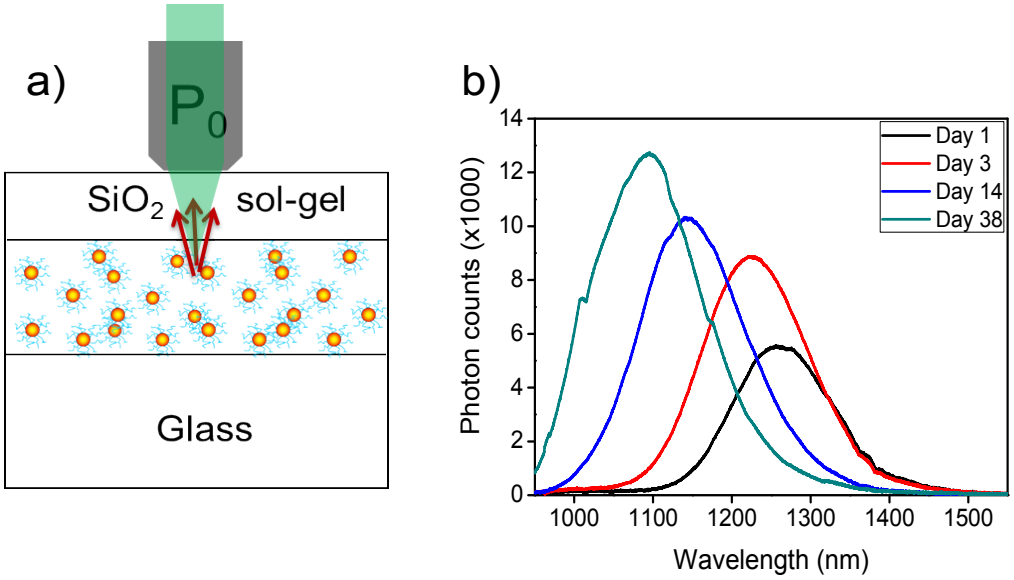

Figure 2.3: A cartoon of PbS QDs buried in SiO_2 environment (a) and their photoluminescence change over more than one month that was routinely recorded (b). PL of PbS in matrix measured at the day of preparation (black), after 3 days (red), after 2 weeks (blue), and after one month and a week (dark green). The sample is pumped with the same power in all these measurements.

Figure 2.3b shows the PL of the PbS QDs in SiO_2 host matrix at different time intervals. In all these measurements, taken over several days, the dots are illuminated with the same intensity and the intensity here is relatively weak to avoid any unwanted deterioration happening to the dots. One can see that the PL of PbS dots changed dramatically over time. It is remarked that the PL spectral peak shifted to shorter wavelength, PL intensity increased, and its Full Width at Half Maximum (FWHM) slightly broadened with time. In particular, within two weeks stored in air, the PL peak shifted nearly 120 nm to the blue, the luminescence intensity increased approximately two-folds, and the FWHM expanded 10 nm.

These observations are consistent with other works [121, 122, 123] on CQDs embedded in dielectric matrices. The evolution of the PL spectra results from the oxidization process of the dots. The cross-linking of HSQ was performed in ambient environment (oxygen) at 150°C, hence it was very likely that oxygen was able to penetrate inside the host matrix. The penetration of oxygen oxidized the surface states and the outermost layers of the dots. As a result, the average size distribution reduced, resulting in a blue-shift of the PL of the dots due to larger quantum confinement in smaller dots.

The oxidization of the outerlayer of the dots had also another impact on the passivation the dots. Because an oxide layer was formed around the dots, the number of trap states and/or surface states decreased. Consequently, luminescence intensity of the dot assembly increased—a phenomenon known as photoactivation.

Lastly, the larger width of PL can be attributed to the inhomogeneous oxidization of the outer shell of dots. It is apparent that PL line width reflects the size distribution of the assembly of quantum dots. When the oxidization of the outer shell occurred, the process was not at the same level to all the dots, i.e. some might have a thinner layer of oxide and some might have a thicker oxide layer, leading to a broader range of dots size distribution. Therefore, the increased PL width was original from the larger size distribution of the quantum dots due to the oxidization process over the time.

2.2.2 Photoluminescence of PbS CQDs as a function of pumping power

Another important parameter that dictates the behavior of the dots alone or coupled with other objects is the excitation power of the laser light [124, 125]. As is well documented, the spontaneous emission varies linearly with the pump power for low pumping intensity and then saturates when the pumping excitation rate starts to exceed the decay rates of the emitters.

Figure 2.4a shows the PL intensity as a function of the pumping power density. The

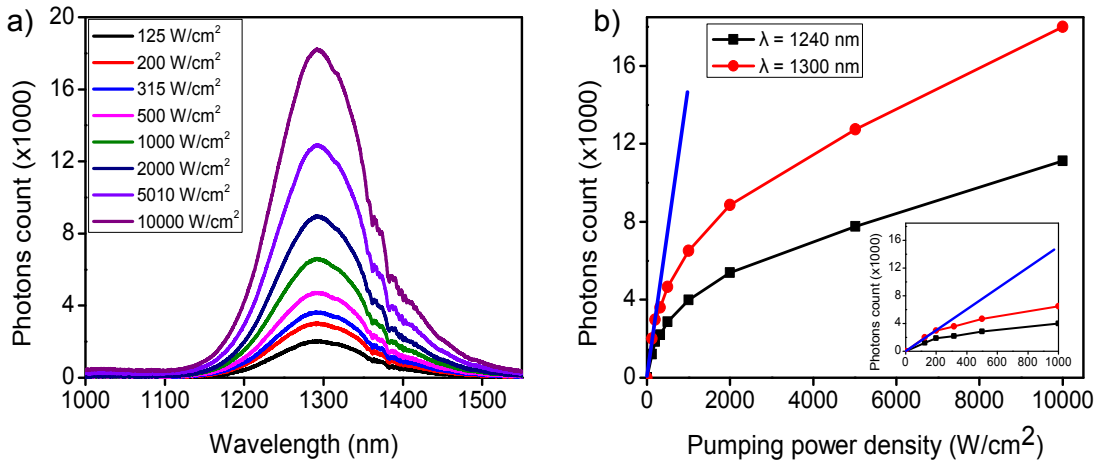

Figure 2.4: PL of PbS QDs as a function of pumping power. (a) PL spectra intensity of PbS in host matrix as the pumping power density is varied from 0.125 MW/cm^2 to 10 MW/cm^2 on the same day of measurement. (b) The saturation curve of QDs at PL peak position λ = 1300 nm (red line) , and at the blue side of the PL curve λ = 1240 nm (black line). The straight blue line is a guide to the eye of linear regime. A better look into the linear response of the PL as a function of power density can be found in the inset. Because the thresholds are the same for both wavelengths, only one line is plotted for the sake of clarity.

measured maximum power of 3 mW from the He-Ne laser and focusing the laser beam by 40X (NA = 0.6) provides us the maximum power density at 10 MW/cm^2. In this set of experiments, we modulate this intensity with a set of neutral density filters. It is shown in Figure 2.3a that the PL intensity of QDs increased while the excitation density was tuned from 0.125 MW/cm^2 up to 10 MW/cm^2. This power dependence of the luminescence can be quantitatively displayed in Figure 2.4b. In this figure, the number of counted photons (integration time: 10 seconds) as a function of pumping power density was plotted for two different wavelengths: one, in red, is selected at the peak of QD emission (λ = 1300 nm) whereas the other, in black, is a wavelength on one side of the QD emission curves (λ = 1240 nm). The straight blue line is a guide for the eyes to show the linear regime of luminescence. We only plot one blue line for the sake of clarity because this linear behavior of QD emission as a function of power is the the same for two investigated wavelengths.

The inset graph in Figure 2.3b is a zoom-in view of PL intensity as a function of

the power density (0 - 1 MW/cm^2). It is clear that the QD PL behaves linearly with excitation density until 200 W/cm^2. The PL intensity of PbS QDs deviates from the linear regime after 200 W/cm^2. However, with the laser source that we used and its maximal power density of 10 MW/cm^2, we were never able to fully reach the saturated regime. This characteristic is different compared to the saturation of some molecules, where a moderate excitation power (2 MW/cm^2 is sometimes sufficient to saturate the emitters [126].

From now, for all the experiments with CQDs where a linear response of the emission rate is required, a maximum power of 200 W/cm^2 will be employed to keep a good quality of the sample, avoid Auger-correlated nonradiative process, and maintain a good signal to noise ratio.

2.2.3 Photoluminescence of PbS CQDs as a function of temperature

The last environment condition that we investigate in this study is the temperature that we vary from cryogenic to ambient values. During this series of measurements, the sample was mounted inside a helium flow cryostat (Oxford Instrument MicrostatHires2). The excitation energy was kept at 200 W/cm^2 to maintain a linear response of QDs emission, and the PL was recorded in reflection mode due to the design of the cryostat.

Figure 2.5a shows the changes of PL spectra of PbS QDs with varying temperatures. The major alterations of PL spectra observed as the temperature is varied from 4K to 300K are the following:

(i) The shape of the PL spectra changes.

(ii) The PL intensity decreases around ten-fold.

(iii) The PL emission peak shifts to higher energy.

(iv) The PL width becomes wider.

To characterize the effects of the temperature, we reploted the spectra of Figure 2.5a as

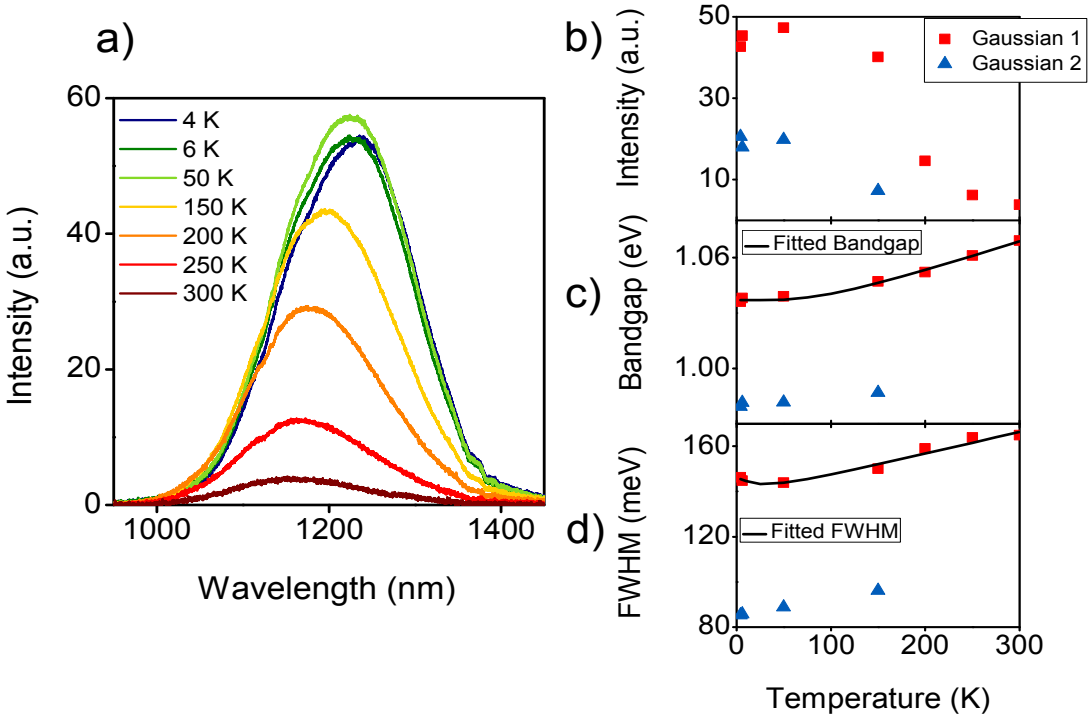

Figure 2.5: PL of QDs as a function of temperature and their Gausian fits. (a) PL spectra of PbS QDs in a host matrix subjected to different temperatures, from 4K to 300K. (b) The intensity of each gaussian as a function of temperature. Gaussian 1 (red squares) appears at all the temperatures and has higher intensity compared to Gaussian 2 (blue triangle) that only appears at low temperature (below 200K). (c) The energy bandgap corresponding to each gaussian as a function of temperature. Black solid line is the fitted curve of semiconductor's bandgap according to Equation 2.1. (d) PL widths of these gaussians as a function of temperature. The temperature dependence of PL width is fitted by Equation 2.2 and shown in black solid curve.

a function of the energy and performed a gaussian fit on the data. While a single gaussian perfectly fits the PL spectra at high temperature (from 300K - 200K), a sum of two gaussians was necessary to reproduce the spectra at lower temperatures, as summarized on Figures 2.5b-d.

Figure 2.5b shows the maximum PL intensity used in the fits as a function of the temperature. It can be seen that the second gaussian curve (blue triangle-up) appears below 200K, and that its PL intensity becomes significant from 150K to 4K. This drove us to a hypothesis that the two gaussians actually represent two disctinct channels of emission. One, which is associated with the first gaussian, is the excitonic recombination

of the semiconductor nanocrystals PbS QDs. The other channel, which corresponds to the second gaussian, is the emission from radiation of the trapped states since there are many surface or trapped states of PbS QDs due to the fact that they are surrounded by long ligands.

In order to confirm this hypothesis, we continue to examine the two gaussian fits by plotting their energy bandgap as a function of the temperature, Figure 2.5c. The energy bandgap of the first gaussian (red square) increases while the energy bandgap of the second gaussian (blue triangle-up) is quite independent of the temperature, as is expected from emission through trap states.

Now we see whether the first gaussian is really associated with the energy bandgap of the semiconductor nanocrystals. It has been documented that the semiconductor energy bandap is strongly influenced by the electron-phonon interactions that in turn depends on the temperature [127, 76, 128, 129, 130]. At a moderate temperature, a large number of lattice phonons are excited since their energies are relatively small (4 meV: acoustic phonon and 26 meV: longitudinal optic phonon for PbS [76]). The phonons influence the chemical bonding through various orders of electron-phonon interactions. O'Donnell and Chen [127] proposed a relation for the temperature dependence of semiconductor bandgap as followed:

$$E_g(T) = E_g(0) + S\langle\hbar\omega_{ph}\rangle[coth(\frac{\langle\hbar\omega_{ph}\rangle}{2k_BT}) - 1] \tag{2.1}$$

where $E_g(0)$ represents the bandgap at zero temperature. In our case, $E_g(0)$ is the energy gap of 1S-1S exciton state at zero temperature. S is a dimensionless coupling constant usually referred to as Huang-Rhys parameter.$\langle\hbar\omega_{ph}\rangle$ is an average phonon energy. An excellent fitting is found with $Eg(0) = 1.038$ eV, $S = 0.9838 \pm 0.289$, and $\langle\hbar\omega_{ph}\rangle = 22.81 \pm 10$ meV. The first two fitting parameters are in good agreement with results published elsewhere [130], but there is a discrepancy of our fitting parameter for the average phonon energy, specifically our fitting parameter is higher than those reported. This is consistent

with the excellent fitting that we achieved at high temperatures, whereas in other works a poor fitting is observed at high temperatures. We attribute these differences with the literature to the fact that each study utilizes a different dielectric host matrix to embed the CQDs, resulting in different phonon interactions. In any case, the very good agreement of Eq. 2.1 with the evolution of the first gaussian of Figure 2.5c is a strong indicator that this gaussian corresponds to the excitonic recombination of the dots. As a corollary, we attribute the second gaussian of Figure 2.5c that is almost independent of the temperature to a radiative recombinaton channel through defect states.

Another feature associated with the temperature is the increasing line width of the PL spectra. Figure 2.5d shows how the FWHM of the two gaussians varies as a function of temperature. Until now, we know that the first gaussian is the emission channel of PbS QD bandgap, and the second gaussian is the emission through the trapped states due to the ligands. Therefore, we will focus on the PL width of the first gaussian. The existence of crystal lattice of QDs creates vibrational modes (like longitudinal optical (LO) and acoustic (LA) phonons) which interact with the carriers of semiconductor, hence influencing the PL line width of QDs. This naive picture can be quantitatively analyzed by fitting with the following formula:

$$FWHM(T) = \Gamma_{inh} + \sigma T + \gamma e^{E_{LO}/k_B T} \tag{2.2}$$

where Γ_{inh} is the temperature-independent inhomogeneous linewidth. Γ_{inh} represents the size and shape distribution of the PbS QDs as the temperature approaching 0K. σ is the exciton-acoustic phonon coupling efficient. γ is the exciton-LO phonon coupling coefficient, E_{LO} is the energy of the LO phonon energy. A good fit from this equation gives us Γ_{inh} = 150.3±1.3 meV, σ = 38.9±10 μeV/K, γ = 26.37±27.8 meV/K, and E_{LO} = 16.38±6 meV.

The last PL feature modified as the temperature went from 4 K to 300 K was the PL intensity. It was seen that the PL slightly increased from cryogenic temperature and

reached a maximum at 50K. This trend has been already observed in other studies and attributed to the fact that a moderate increase of the temperature was able to activate carriers out of trapped states, contributing to an enhancement of radiative recombinations. Further increase in temperature up to ambient one led to a decrease of PL intensity around tenfold due to the activation of the phonon population. The observation was compared and found consistent with other published work [129].

To conclude, as the temperature dropped from 300K down to 4K, the results proved that there are two channels of emission. One with higher energy level is associated with the excitonic recombination of PbS nanocrystals while the other with lower energy level is the emission through the defects/or trapped states at surfaces of QDs. Thermal expansion was also the origin of an increase of PbS nanocrystal bandgap and a widening of PL linewidth.

So far, we have characterized the basic responses of PbS QDs embedded in a homogeneous glass matrix. We have seen the PL of PbS QDs blue shifted and higher quantum yield over time. We also examined how the dots emit with different excitation power and determined a threshold power ($200 W/cm^2$) where the dots emission rate behaves linearly with the pumping power. Lastly, we investigated their PL as a function of the temperature.

2.3 Plasmonic nanoantennas: arrays of nanorings

Before studying the interactions between CQDs and plasmonic antennas, it is important to discuss the properties of the latter alone. Here we work with nanoring arrays, in which the dimension of each plasmonic antenna is typically in the range from a few tens to a few hundreds nanometers. The exact size and periods have been chosen according to two criteria: first, the period is always chosen to be subwavelength so as to remove any diffraction effects that would otherwise complicate the interpretation of the results. Second, the plasmonic resonances must occur in the same spectral range as the emission

of our PbS CQDs in their dielectric host matrix, namely in the 1000 - 1500 nm window. Before I began my PhD project, a number of investigations have been performed on the nanoring geometry [131, 132, 133, 59, 134, 135]. These studies showed that nanorings sustain a wide variety of plasmonic resonances in the visible and near-infrared and that the wavelength of the fundamental resonance is typically more than 5 times larger than the diameter of the structures. Last, but not least, previous calculations in our group [59] revealed that because of their centrosymmetric geometry, nanorings are well suited to PL studies in which fluorophores are randomly distributed around them because their spectral response is largely independent from the exact position of point-source emitters.

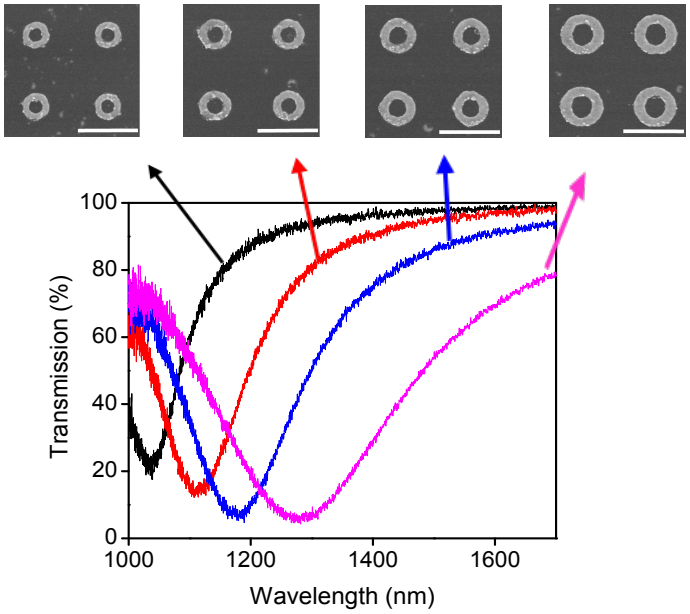

Figure 2.6: SEM images of different nanorings fabricated by e-beam lithography and their transmission spectra. SEM images of the nanorings are cropped views of a 100 µm x 100µm array of nanorings. Those rings have the same pitch (p = 600nm) and 35 nm of height, yet different radii. The far-field transmission spectra of these nanorings arrays on a glass substrate indicate that their plasmonic resonances can be tuned by varying the geometrical parameters, or in general by altering the filling factor. White scale bar: 500 nm.

In this thesis, we usually fabricate arrays of nanorings with lateral dimensions of 100µm x 100µm. The arrays of nanorings are fabricated by e-beam lithography. A layer of positive-tone resist is exposed to an e-beam where structures are written according to a designed mask. After exposure, the resist is developed and followed by e-beam evaporation

of gold. The sample is then immersed in 2-Butanone solution to remove the unexposed areas, see Appendix A for the details of fabrication process. Figure 2.6 shows the SEM cropped images of the fabricated nanoring arrays and their far-field transmission spectra. The cropped images in Figure 2.6 are nanorings with different geometrical parameters but the same pitch p = 600 nm. Magnified images of the nanorings (not shown in picture) indicate that the fabricated nanorings meet the initial parameter design, where the inner ring radius is increased and their ring wall thickness (ring wall thickness is defined as the difference between outer radius and inner radius) is kept constant. To complete geometrical verification, an AFM characterization is performed and showed that the ring surface is fairly uniform and there is a slight difference between the Au nominal height (35nm) and actual height of gold nanoring (40nm-including 2nm of Ti adhesion layer). The small deviation indicates that the metallic deposition step is well-controlled.

The localized surface plasmon resonance associated with a given array is determined by Fourier Transform Infrared (FTIR) spectrometer (Agilent 670 IR) coupled with an optical microscope. Figure 2.6 also shows the transmission spectra of the different nanoring arrays. The dips of transmission spectra are the fundamental surface plasmon resonances (LSPR) of the different arrays, where most of the energy of the external infrared signal are converted into the LSPR rather than passing through the structure.

The curves of the transmission spectra reveal that the plasmonic resonances can be easily tuned by changing the dimensions of the nanorings. Particularly, as the outer radius of nanoring is varied from 108 nm (left) to 165 nm (right), the plasmonic resonance of the corresponding structure is tuned from 1035 nm (black) to 1280 nm (pink). Besides, the resonance line width also expands considerably while we keep the unit cell constant and enlarge the size of the nanoring. This resonance broadening is a signature of increased damping due to the lateral dipole-dipole coupling amid neighboring nanorings.

2.4 Probing the interaction between Au nanoring arrays and PbS CQDs

In this section, PbS QDSs in a sol-gel matrix and arrays of Au nanorings are brought together, as depicted in Figure 2.7a. Au nanoring arrays and QDs embedded in a SiO_2 are buried under a 190 nm thick layer of SiO_2, hence they experience a symmetric environment. To probe the coupling mechanisms of the dots with the nanorings, the distance between the nanoring arrays and the layer of QDs is varied by introducing a thin spacer of silica (see Appendix A for complete fabrication recipe). To quantify the coupling between the dots with the rings, we measure the PL spectrum above each structure and normalize the data with the luminescence of a neighboring region without metallic pattern. The resulting ratio provides the relative PL enhancement above the metallic structures as a function of the wavelength. By performing this normalization procedure, we obtain relative PL enhancement spectra that are not affected by the spectral evolution of the dots in HSQ evidenced in Figure 2.3. Appendix B provides all the details about this procedure.

Figure 2.7b summarizes the relative PL enhancement as the distance between the nanorings and the CQD-doped layer of HSQ varies from 0 to 75 nm. All samples have a period P = 600 nm and the nanoring inner, outer radii and height are 56 ± 3 nm, 110 ± 2 nm, and 35 ± 2 nm, respectively. One can see that the PL enhancement is the highest when the HSQ layer with embedded QDs is the closest to the rings and that the enhancement decreases significantly as the distance between this layer and the rings increase. This result is consistent with the literature: it indicates that, as the CQDs are placed farther away from the rings, they interact less with the plasmonic resonance and its exponentially decaying fields. It is also worth noting that since we work with CQDs embedded in a 100 nm thick layer of HSQ, the enhancement values recorded here correspond to an average of all the dots dispersed in HSQ.

To gain quantitative insight into these interactions, we now focus on two samples that represent two distinct regimes of PL enhancement: one in which the separation distance

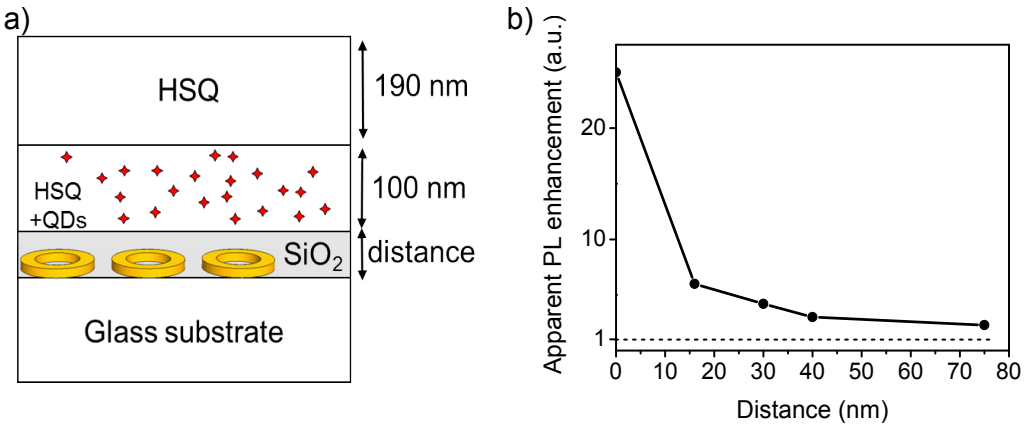

Figure 2.7: Schematic of full sample and PL enhancement as a function of SiO_2 thickness. (a) The diagram of fully-layered sample prepared for studying the interactions between QDs and nanoring arrays. As illustrated in the diagram, Au nanorings arrays are made by e-beam lithography on a glass substrate. A layer with variable thickness of SiO_2 is deposited by PECVD at 300^{o}C, a 100 nm thick layer of embedded PbS QDs is spincoated, followed by a 190 nm thick of SiO_2 sol-gel transferred from HSQ. This thick top SiO_2 layer is very crucial to achieve enhancement of PL because it helps QDs and nanorings experience a symmetric SiO_2 environment. (b) The apparent enhancement of PL with a varied space thickness from 0 nm to 75 nm.

between the Au nanorings and the CQD-doped layer of HSQ is set to 40 nm and another sample in which the Au nanorings are directly in contact with the CQD-doped layer.

Figure 2.8a shows the PL enhancement spectrum for the first sample of interest (i.e. with a SiO_2 spacer of 40 nm between the Au nanorings and the CQD-doped layer of HSQ). We have recorded the same relative spectrum over several days and did not observe significant changes: in all cases, a broad peak centered on 1225 nm corresponding to the excitation of the fundamental plasmonic resonance of the rings is observed and the maximum spectral enhancement is around 3. These experiments demonstrate that it is possible to perform quantitative and reproducible antenna experiments with CQDs embedded in a dielectric host matrix, even though we have seen previously that the spectral signature of the dots blueshifts over time, see Figure 2.3. This is because we plot here the *relative* PL enhancement, defined by the ratio of the PL above and outside the metallic structure and this ratio remains the same regardless of the absolute spectral signature of the dots. To get a more quantitative view of this stability, we plot in Figure

2.8b as a function of time the maximum value of the PL enhancement, as well as the quantity $\Delta\lambda' = \lambda_{LSPR} - \lambda_{Enhancement}$, corresponding to the difference between the spectral position of the plasmon resonance (as measured by FTIR measurements) and the spectral position of the relative PL enhancement peak.

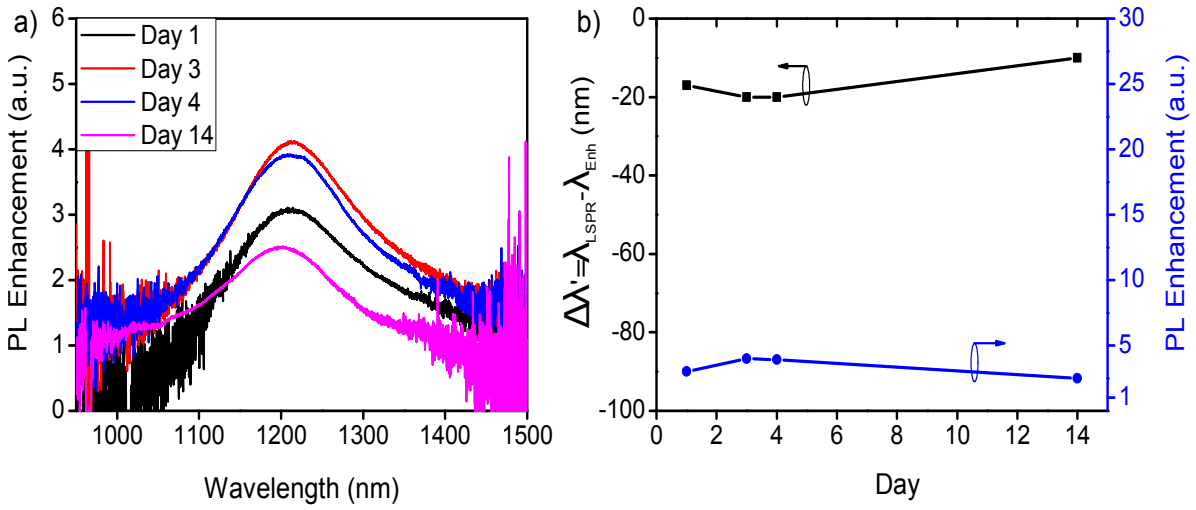

Figure 2.8: PL enhancement evolution overtime for a SiO_2 spacer thickness d = 40 nm. (a) PL enhancement spectra of one representative nanoring array (Period = 600 nm, ring parameter: inner, outer diameters and height are 120, 210, and 35 nm, respectively.) coupled with PbS QDs over two weeks of monitoring. (b) The difference, $\Delta\lambda' = \lambda_{LSPR} - \lambda_{Enhancement}$, between plasmon resonance wavelength and PL enhancement peak position and amplitude of PL enhancement were traced as a function of time.

We now perform the same experiments for the second sample, that is, the sample in which the layer of CQD-doped HSQ is directly coated onto the Au nanorings. Figure 2.9a shows that this sample exhibits a radically different behavior: when measured just after fabrication, the PL enhancement spectra has a very high amplitude and asymmetric shape. Then, when the measurement is repeated in the following days, one notice a very sharp decline of the enhancement and a blueshift of the peak. Eventually, the PL enhancement spectrum becomes stable after approximately 10 days. In the stable regime, the PL enhancement spectrum is very reminiscent of the spectra of Figure 2.8 corresponding to the sample where a spacer of 40 nm was inserted between the Au nanorings and the CQD-doped layer of HSQ.

Figure 2.9b provides another view of this dramatic evolution by plotting the maximum

PL enhancement and the quantity $\Delta\lambda' = \lambda_{LSPR} - \lambda_{Enhancement}$ over time. When the sample reaches stability after 10 days, one can see that $\Delta\lambda'$ is small, indicating that the PL enhancement spectrum has the signature of the plasmonic resonance.

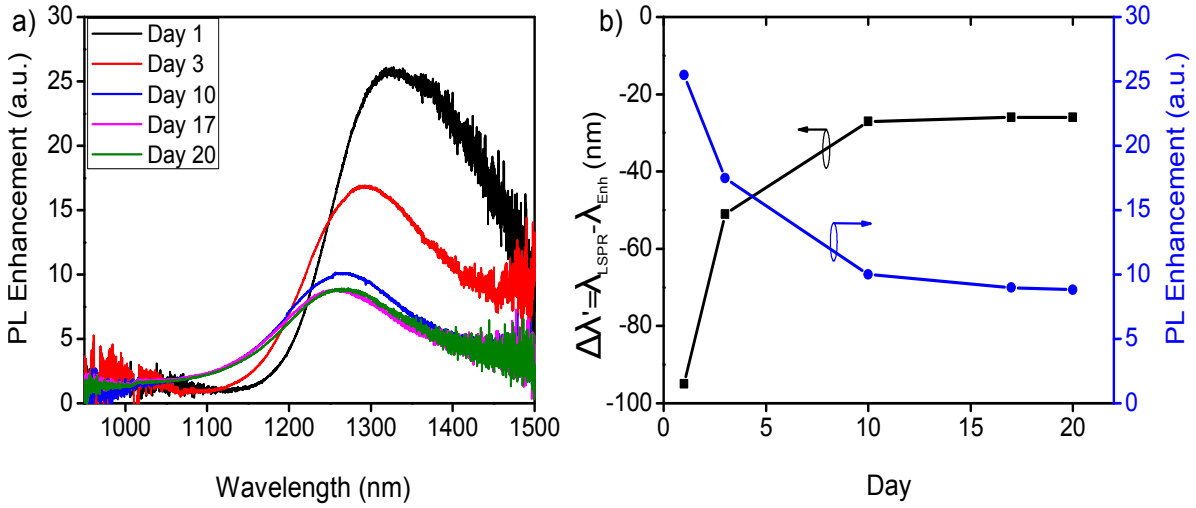

Figure 2.9: PL enhancement overtime for spacer thickness d = 0 nm. (a) PL enhancement of the same nanoring array as in Figure 2.8 interacting with PbS QDs over nearly three weeks of monitoring. (b) a similar graph like Figure 2.8b, $\Delta\lambda' = \lambda_{LSPR} - \lambda_{Enhancement}$ and the amplitude of the PL enhancement were tracked over time.

We interpret the results of Figure 2.9 by the fact that the CQDs are embedded in a 100 nm thick layer of HSQ. When the sample is fresh, the PL enhancement is mainly due to the dots in direct vicinity of the nanorings since they are in the direct near-field of the plasmonic resonances. In contrast, the contribution of the QDs that are far from the rings is weak in comparison. Then, the spectral changes observed in Figure 2.9a and the sharp decrease in the PL enhancement indicate that the dots in direct proximity of the nanorings are degraded and gradually cease to play a role in the light emission. The origin of this quenching is not clear to us: it arises probably because the HSQ matrix is not stable, allowing complex photoreactions to occur due to the high local fields of the surface plasmon resonances. Eventually, after 10 days, all the dots in direct proximity of the nanorings are quenched and only the dots in the upper part of the HSQ layer, those that are the farthest from the nanoring arrays, contribute to the PL. Thus, in this latest evolution stage, the sample is very similar to the one previously studied in Figure 2.8: it

consists of a collection of CQDs that are separated from the rings by a dielectric spacer. As we have shown with Figure 2.8, this configuration is very stable over time, the PL enhancement is rather modest but there is a clear peak corresponding to the excitation of the plasmonic resonance that do not evolve as the sample continues to get older.

Based on these considerations, we will now only focus on samples in which the CQD-doped layer of HSQ is separated from the nanorings by a small dielectric spacer. This configuration is stable, reproducible. In addition, it ensures that the interactions between the CQDs and the nanoring arrays are mediated by the electromagnetic field rather than by complicated, non-radiative effects that are known to occur when the distance between the dots and the plasmonic particle is smaller than 5-10 nm. Before investigating these interactions in detail, we first remind in the next section the theoretical model that is almost universally used to understand the radiative coupling between quantum emitters and optical antennas.

2.5 Quantum emitter interacting with a metallic nanoparticle : Theoretical Model

We consider here a generic emitter with three energy levels without degeneracy. The level 1 is ground state, level 3 is a highly excited state and level 2 is the excited state with lowest energy. Exciting the emitter into the level 3 can be achieved with an proper external light source. It is generally considered that the de-excitation from highly excited level 3 to lower excited level 2 happens extremely fast, as a result the population on level 3 is negligble at all times. As relaxing to the ground level from level 2, they re-radiate light that is satisfied transition $E_2 - E_1 = \hbar\omega_f$. With these assumptions, our model is that of a two-level emitter [136, 126, 67].

In a weak and continuous excitation regime which corresponds to the illumination conditions used in our experiments, the fluorescence collected by the detector can be

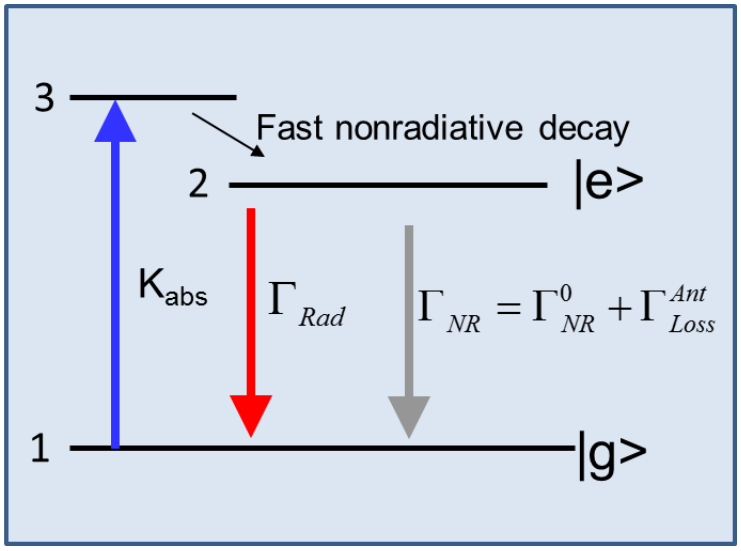

Figure 2.10: Schematic of a two-level model. In general, this model is utilized to describe fluorophore-metal interactions. It is common to neglect the extremely fast non-radiative decay process within excited level from level 3 (top level) to level 2 (middle level), hence only two levels (level 1 and level 2) are considered.

written as:

$$P(\omega_f) = k_{det}(\omega_f) N_{exc} \Gamma_R(\omega_f) \tag{2.3}$$

where $k_{det}(\omega_f)$ is the response of the detector (including the effects due to its finite collection angle of the objectives) integrated over the acquisition time of the measurement, $\Gamma_R(\omega_f)$ is the radiative decay rate at the fluorescence frequency ω_f, and N_{exc} is the number of the emitters in the excited states. As we neglect the population at level 3, the total population of the emitters under the continuous wave and week field regime is:

$$N(t) \simeq N_g(t) + N_{exc}(t) \tag{2.4}$$

In this regime, we can neglect the stimulated coefficient so that the variations of N_{exc} at all time is equal to the difference between the radiative recombinations and excitations:

$$\frac{dN_{exc}}{dt} = -(\Gamma_R(\omega_f)) + \Gamma_{NR}^{ant} + \gamma_{nr0}) N_{exc} + N_g \sigma_{abs}(\omega_{abs}) I_{inc} |K(\omega_{abs})|^2 \tag{2.5}$$

where Γ_{NR}^{ant} represents the rate of photons extracted from the emitter that are eventually absorbed due to the metallic losses,γ_{nr0} is the intrinsic nonradiative decay rate of the sources, N_g is the population of emitters in the ground state, $\sigma_{abs}(\omega_{abs})$ is the cross section absorption of the emitter at the pumping frequency ω_{abs}, I_{inc} is the pumping intensity, and $|K(\omega_{abs})|^2$ is the modified irradiation at ω_{abs} due to the presence of the antenna. Because we assume that the pumping light is a continuous-wave laser, or $dN_{exc}/dt = 0$, hence we obtain:

$$N_{exc} = N_g \frac{\sigma_{abs}(\omega_{abs}) I_{inc} |K(\omega_{abs})|^2}{\Gamma_R(\omega_f)) + \Gamma_{NR}^{ant} + \gamma_{nr0}} \tag{2.6}$$

Filling equation of N_{exc} into equation of $P(\omega_f)$ we have:

$$P(\omega_f) \propto k_{det}(\omega_f)\eta(\omega_f)|K(\omega_{abs})|^2 \sigma_{abs}(\omega_{abs}) I_{inc}(\omega_{abs}) N_g \tag{2.7}$$

where $\eta(\omega_f)$ is the modified quantum yield of the emitter due to the Purcell effect [137]

$$\eta(\omega_f) = \frac{\Gamma_R(\omega_f)}{\Gamma_R(\omega_f)) + \Gamma_{NR}^{ant} + \gamma_{nr0}} \tag{2.8}$$

The luminescence of the emitter alone can be described by:

$$P_0 \propto k_{det}(\omega_f)\eta_i \sigma_{abs}(\omega_{abs}) I_{inc}(\omega_{abs}) \tag{2.9}$$

where η_i is the intrinsic quantum yield of quantum emitter ($\eta_i = \gamma_{r0}/(\gamma_{r0} + \gamma_{nr0})$). By writing this expression, it is supposed that the detector response k_{det} is the same in the presence and in the absence of nanoantennas. We can make this assumption because we have verified that the PL enhancement spectra do not significantly vary when we repeat the experiments with a microscopic objective having a different numerical aperture.

$$\frac{P}{P_0} \propto \frac{1}{\eta_i} \frac{\Gamma_R/\Gamma_R^0}{\Gamma_R/\Gamma_R^0 + \Gamma_{NR}^{Ant}/\Gamma_R^0 + \frac{1-\eta_i}{\eta_i}} |K(\omega_{abs})|^2 \tag{2.10}$$

For optical antennas predominantly operating through the Purcell effect, the contribution $|K(\omega_{abs})|^2$ is small and Eq. P/P_0 clearly predicts that P/P_0 strongly varies with η_i. If η_i is close to one, corresponding to bright emitters with little non-radiative decay channels, the fluorescence rate can only drop because any increase in Γ_r is offset by the absoption losses Γ_{NR}^{Ant} of the plasmonic antenna itself. In contrast, an increase of Γ_R via the Purcell effect can substantially boost the luminescence of low η_i emitters. Figure 2.11 illustrates this discussion with an electrical dipolar emitter coupled to a Au nanotorus supporting a localized plasmon resonance at 1160 nm. The quantities Γ_R/Γ_R^0 and $\Gamma_{NR}^{Ant}/\Gamma_R^0$ have been calculated by Dr. Tatiana Teperik with the boundary element method (BEM) using a lossless classical dipole [59, 134, 135] and we represent in Figure 2.11 the ratio P/P_0 given by Eq. 2.10 for two different quantum yields: η_i = 0.95 (black curve) and η_i = 0.1 (grey curve). One can clearly see that the antenna enhances the spontaneous emission of the poor emitter and degrades the luminescence of the bright one; in addition, the spectral shape of P/P_0 considerably changes with η_i even though the remaining parameters have been kept constant.

When strong pumping power is applied leading to the saturated emission, the rate equations change in such a way that the enhancement through the Purcell effect does not depend on η_i:

$$P \propto \Gamma_R \sigma_{abs} I_{inc}(\omega_{abs}) \tag{2.11}$$

In this regime, the ration P/P_0 becomes:

$$\frac{P}{P_0} \propto \frac{\Gamma_R}{\Gamma_R^0} \tag{2.12}$$

which is now independent of the intrinsic quantum yield η_i. The red curve of Figure 2.11 plots the ratio P/P_0 given by Eq. 2.12 for the same system considered previously. These calculations show that, in the saturation regime, the PL enhancement is significantly higher, the spectrum become narrower, and the peak position of normalized P/P0 has

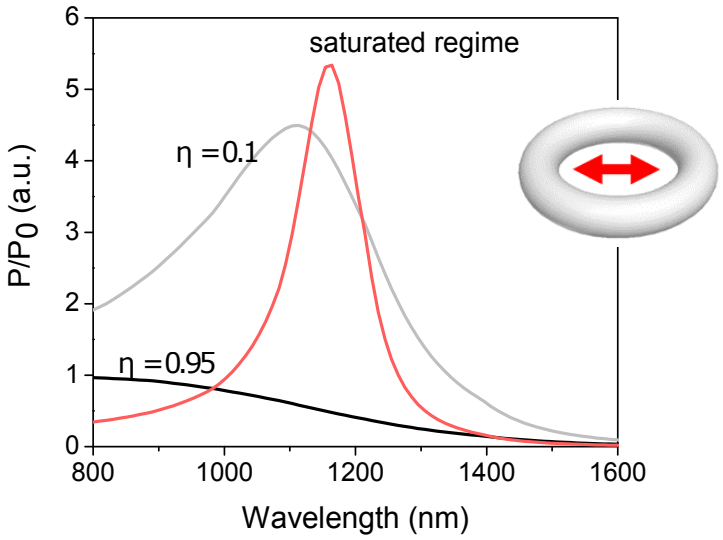

Figure 2.11: Two-level model prediction. This quantitative prediction is calculated for a gold toroidal nanoantenna sustaining a plasmonic resonance at 1160 nm interacting with a single emitter which is placed on its symmetric axis of the toroidal nanoantenna. Red curve is the spectral prediction for the nanoantenna coupled with a single emitter with a saturated emission rate. Light grey curve is the spectral prediction for the nanoantenna coupled with a bad emitter (its intrinsic quantum yield $\eta_i = 0.1$. Lastly, the black curve is the spectral prediction of the nanoantenna coupled with a good emitter (its intrinsic quantum yield $\eta_i = 0.95$

shifted to the wavelength of the plasmonic resonance.

In conclusion, the two-level model predicts that the metallic nanoparticles have a substantial influence on the spontaneous emission spectra of quantum emitters as they are coupled to each other through Purcell effect. If a normalized ratio is used to characterize the emission modification, the model tells us that the spectral ratio is considerably changed with the excitation power and intrinsic quantum yield of the emitters.

2.6 Experiments to test predictions of the two-level model

The two-level model described in the previous section is widely used to make educated guesses on antenna systems but its validity has never been checked for the systems of CQD embedded in dielectric host matrices and interacting with nanoparticle arrays studied in this chapter. Here we carry two series of experiments to test this model, one in which

we study the PL enhancement as a function of the pump power and the other in which we vary the intrinsic quantum yield of the PbS QDs with the temperature. As explained earlier, we consider here samples in which the layer of CQD-doped HSQ is separated from the nanoring arrays by a thin SiO_2 spacer. This spacer ensures that we are in the conditions of the two-level model (namely, that the dots and the antennas interact through the electromagnetic field only) and also that the samples are stable over time (see Figure 2.8).

2.6.1 PL enhancement as functions of pumping power

The first series of experiments that we conducted to check whether the generic two-level model is suitable to describe the behavior of our system are power-dependent measurements that will test two equations: 2.10 and 2.12. As before, the laser we used for these measurements is a He-Ne laser (Melles Griot) emitting a continuous (CW) red laser light at 632.8 nm with maximal power that we measured at 632.8 nm is 3 mW.

As discussed in Section 1.2.2, by varying the power of the laser with neutral density filters, we can switch from the linear regime to a new regime evolving towards saturation (although it should be noted that the limited power of our laser prevented us from achieving full saturation).

We fabricate a sample which has a schematic like in Figure 2.7a with a spacer SiO_2 layer between the nanorings and dots of 30nm. This value is selected to make a compromise working only with the Purcell effect while maintaining a decent enhancement. For this study, we fabricate different arrays of nanorings where we keep the unit cell of nanoring unchanged at 600 nm, but we change the size of nanorings as illustrated in SEM inset images in Figure 2.12.

After having a completed sample with all necessary layers on, we perform the far-field FTIR of nanorings arrays to determine their plasmonic resonances. Top and bottom spectra of Figure 2.12 show the transmittance and reflectance of the corresponding nanorings. The color code is the same for both transmittance and reflectance spectra.

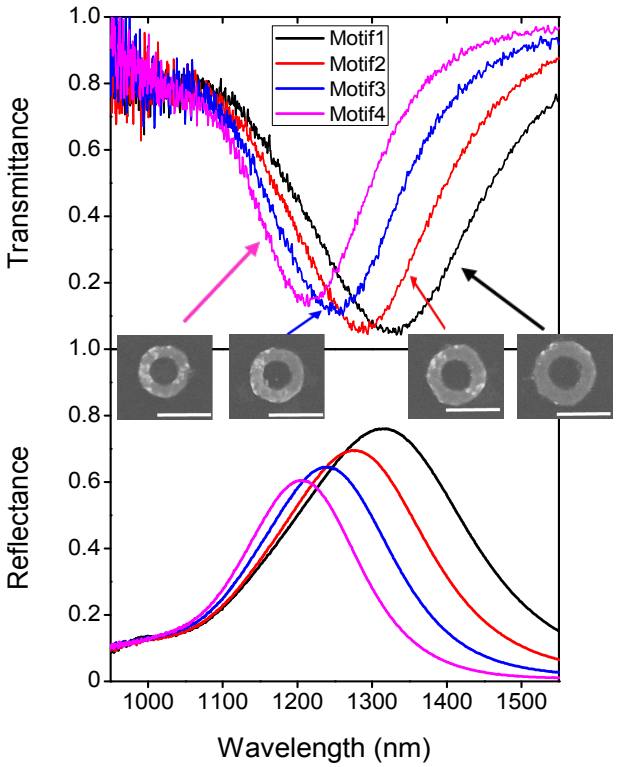

Figure 2.12: SEM images and FTIR spectra of the metallic inclusions. White scale bar: 250 nm. Top graph is the far-field transmission spectra of different rings, named Motif 1, 2, 3, 4. SEM images of single nanoring antenna are the cropped view of the corresponding array. Bottom graph is the far-field reflection spectra of the nanoring arrays with the same color codes of transmission spectra.

The dips in transmittance and peaks in reflectance are associated with the plasmonic resonances of the nanorings. As we vary the outer diameter of the nanorings from 230 nm to 280 nm, the plasmonic resonance is tuned from 1200 nm to 1350 nm. As the dimension of the rings is larger, their plasmonic resonances not only shift to the higher wavelength, but also become broader due to increased dipole-dipole coupling [138].

Figure 2.13 shows the PL enhancement of the nanorings coupled with PbS QDs. The top and bottom graphs are associated with the PL enhancement when the system is excited with weak power density (0.2 MW/cm^2, corresponding to the linear regime of spontaneous emission) and high power density (10 MW/cm^2, where the dots are not fully saturated but still far from the regime of linear spontaneous emission). It can be seen that the PL enhancement spectra in both excitation conditions have profiles similar to those of the corresponding FTIR spectra, which is a strong evidence that the emission

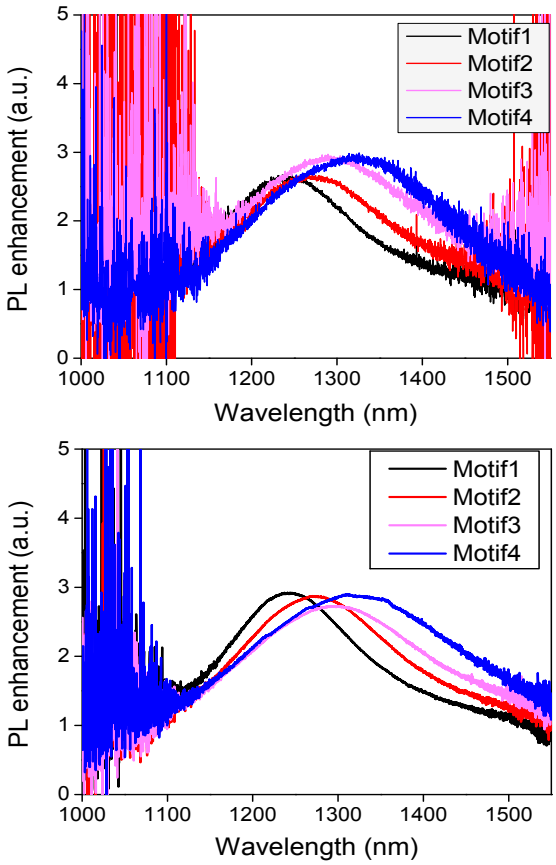

Figure 2.13: PL enhancement with low pumping power and high pumping power. Top graph shows the PL enhancement with weak pumping power for the nanorings, which are characterized in Figure 2.11, coupled with PbS QDs in host matrix. Bottom graph is the PL enhancement for the same system but with a power close to the saturated emission regime of PbS QDs. Again, color codes are kept the same for Figure 2.12 and 2.13.

of PbS QDs is modified through the Purcell effect. Another interesting feature as we compared the PL enhancement spectra at two pumping conditions is that their amplitude of enhancement are almost constant at around three-fold regardless of the structures. Lastly, PL enhancement profiles look similar for both pumping conditions. This can be shown better in Figure 2.14a.

Figure 2.14a superimpose the PL enhancement for two representative structures with weak (light grey color) and high (light red color) excitation power. One cans clearly see that the PL enhancement is almost completely identical no mater what the excitation power is. This behavior is not only true for these two selected structures, but also true

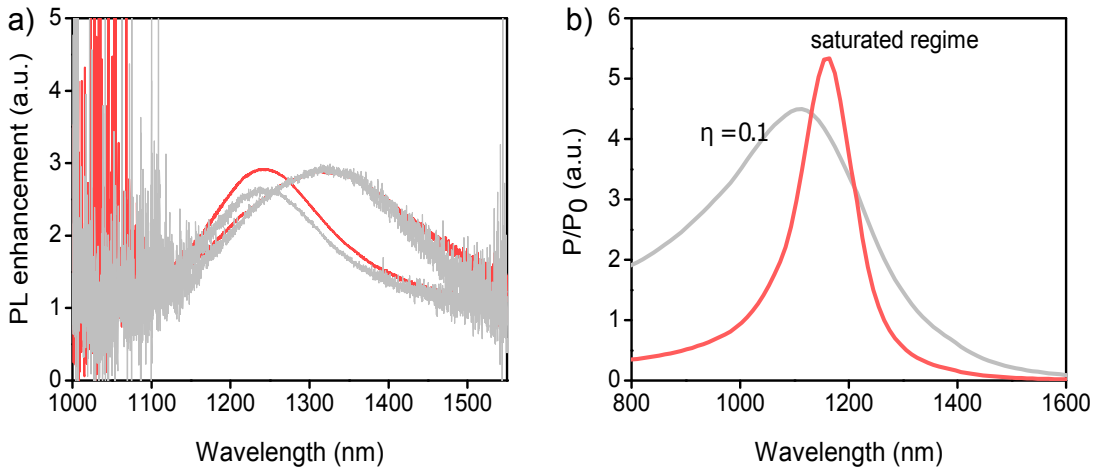

Figure 2.14: A comparison of our experimental data with the theoretical prediction of the two-level model. Left graph is the superposition of two structures with different pumping powers and measured at room temperature. The red curves are PL enhancement of two structures with a power approaching the saturated regime of QD emission. The light grey curves are PL enhancement of the same motifs in linear regime of pumping power. The superposition shows that PL enhancement spectra do not change at all regardless of the pumping power. Only the superposition of two arrays are plotted for the sake of clarity, however, these features are the same for other structures that are not plotted. Right graph is the theoretical prediction from the two-level model of the nanoantenna coupled with a saturated emitter (in red) and an unsaturated emitter (in gray) similar to experimental conditions.

for the two other structures not shown in Figure 2.14a for the purpose of clarity. From this comparison, we can draw the conclusion that the PL enhancement is independent of the pumping regime, i.e. it does not depend whether the dots are in the linear regime of spontaneous emission or in a (near-) saturated state. This fact is in contradiction with the predictions from the two analytic formulas of the two-level model. The model states that there should be a considerable change in terms of shape, position, and amplitude of emission modification spectra for two different cases of optical excitation power. This predicted picture is replotted in Figure 2.14b, where we calculate the influence of the nanotorus on the classical dipole. The grey curve in Figure 2.14b shows the influence of nanoantenna on quantum dot's emission with week excitation (Eq. 2.10) and η_i = 0.1, whereas the influence with the saturated pumping condition (Eq. 2.12) is represented by red curve. It is noted here that the spontaneous emission modification of the system in

equation 2.10 is calculated with $\eta_i = 0.1$ which is the closest value of the intrinsic quantum yield of PbS QDs used in this experiment [128].

Figure 2.14 is an overview picture of the comparison between what we were expecting to see by following theoretical predictions from two-level model (Figure 2.14b) and the real measurement (Figure 2.14a). Despite the input parameters in experiments and calculation are carefully chosen to match, there is still a clear disagreement of experimental data with theoretical predictions from model. Nonetheless, it can be argued that the dots are not fully saturated in our experiments (cf. Figure 2.4) but only far from the linear regime, which may explain the discrepancy with Eq. 2.12 which assumes full saturation. The following temperature-dependent experiments will bring additional evidence that the two-level model is in fact not valid for our systems.

2.6.2 PL enhancement as a function of temperature

In this series of experiments, we perform temperature-dependent PL measurements for the same type of samples, except that the nanorings that we consider here have fixed dimensions (inner radius, outer radius, and height are 55, 110, and 35 nm, respectively), whereas the period of each array is varied from 700 nm to 350 nm; top image (p = 700 nm), middle image (p = 500 nm) and bottom image (p = 350 nm), illustrated in the left panel of Figure 2.15. Otherwise, the stacking is the same as previously, with a 30 nm spacer of SiO_2 between the Au nanostructures and the QD-doped HSQ layer.

Specifically, this study will test equation 2.10. The coupling degree between our nanoring arrays and PbS CQDs is still determined by the ratio P/P_0. P is the PL intensity of QDs on top of the nanorings, whereas P_0 is the PL intensity of QDs alone in a region that is far from the Au nanoring arrays. Last, the pumping power is maintained at weak power density (0.2 MW/cm^2) so that we are working in the linear regime of spontaneous emission.

Figure 2.15, on left panel, shows cropped images of some selective arrays fabricated for this study. The localized surface plasmon resonance associated with a given array is

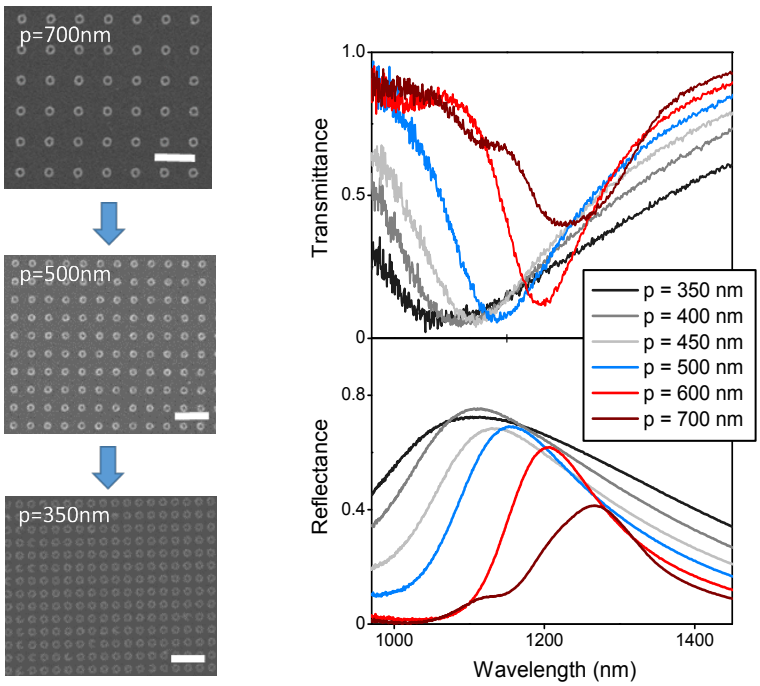

Figure 2.15: SEM images and FTIR of the structures used for the temperature dependent study. White scale bar: 1 μm. Left panel is the SEM images of cropped view of the arrays. In these images, geometrical parameters of the nanorings are kept unchanged (inner, outer radius and height are 56 ±3 nm, 110±2 nm, and 35±2 nm, respectively), but distance between the nanorings is altered by varying the period. Three images are representative images of some periods used with p =700 nm (top left), p = 500 nm (middle left), and p = 350 nm (bottom left). Right panel is the far-field FTIR spectra of the nanoring arrays. Again, the transmittance and reflectance of each structure is used with the same color code.

determined by FTIR measurement in both modes: transmission and reflection, right panel in Figure 2.15. Well-defined peaks in reflection and dips in transmission are the signature of the fundamental plasmonic resonances of the nanoring arrays. We see that as the period of nanorings diminishes from 700 nm to 350 nm, the dips and peaks are shifted to higher energy and become broader, indicating that the localized plasmonic resonance are increasingly coupled as the nanorings getting closer [138]. Note that the complex spectral shape obtained for P = 700 nm is an artifact from our experimental setup: the structures are illuminated with a converging beam that induces unwanted diffraction effects for this large period.

Figure 2.16a replots the PL of pure PbS QDs on a glass substrate as a function of

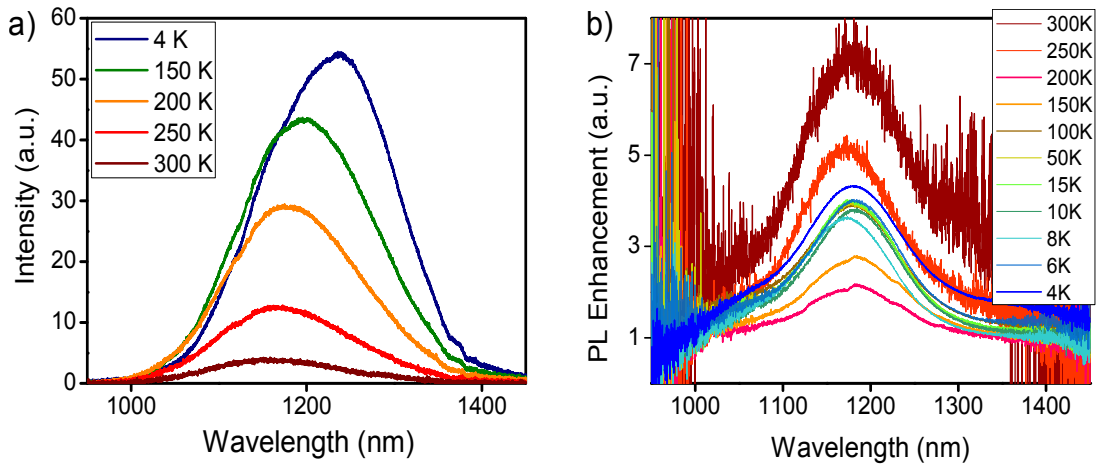

Figure 2.16: PL enhancement at different temperatures. Left graph is the replotted PL of solely QDs at several temperatures. Right graph is the PL enhancement as a function of temperature for one representative structure (p = 600nm) coupled with PbS QDs with 30 nm of SiO_2 spacer. The sample is pumped at low power, in the linear regime of spontaneous emission.

temperature. In this graph, we only choose some representative temperatures to demonstrate that the intrinsic quantum yield η_i of PbS QDs can be varied in a large range by adjusting the temperature. As discussed in Section 2.2.3, as we decreased the temperature from 300K to 4K, we see approximately a ten-fold increase of the PL intensity. It has been pointed out in other works that at room temperature the quantum yield of PbS QDs $\eta_i \approx 0.1$ [128]. In a rough approximation, we can therefore say that the quantum yield of PbS QDs can be tuned from $\eta_i \approx 0.1$ at 300K and $\eta_i \approx 1$ at 4K.

We determine the PL enhancement for one representative array of nanorings with period p = 600 nm as a function of temperature. Figure 2.16b shows PL enhancement spectra for the nanoring array with period p = 600 nm as the temperature is increased from 4 K to 300 K. It can be seen that the nanoring array enhances the luminescence of PbS QDs, albeit the amplitude is different from one to another, and the PL enhancement spectra seem to have a similar profile in terms of the peak position and line width.

Figure 2.17a summarizes the results of the measurements for different arrays of nanorings at room temperature. This figure shows that the amplitude of the PL enhancement

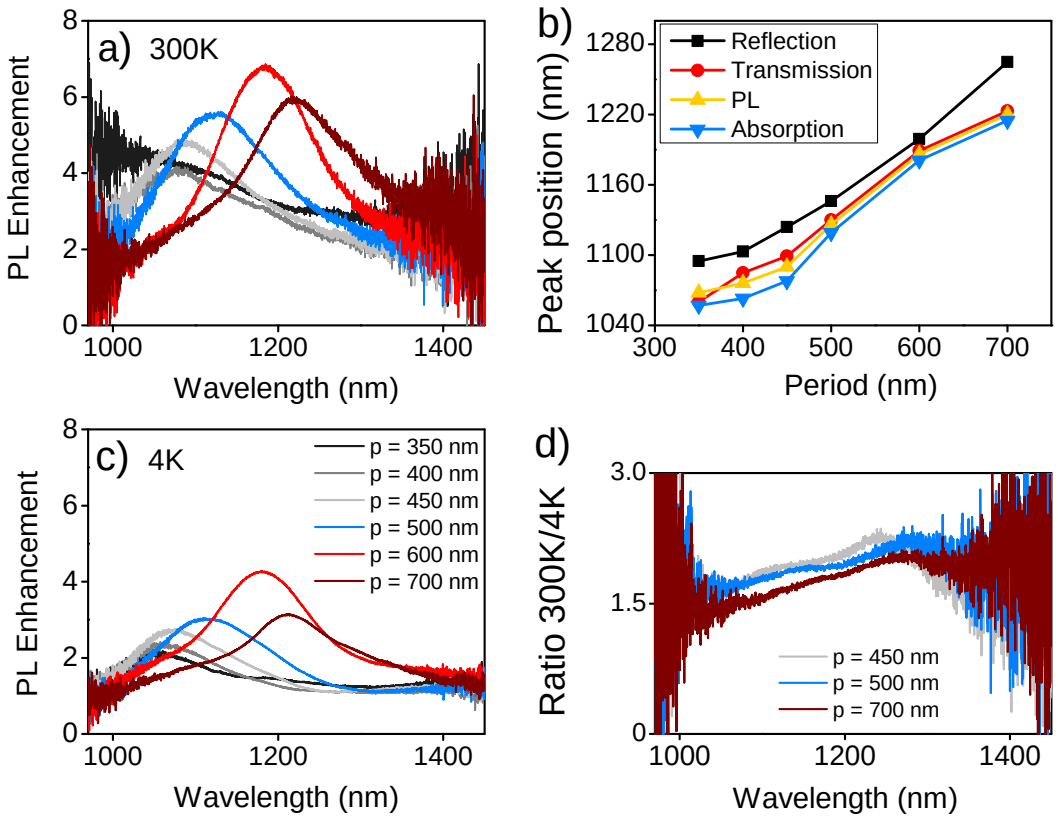

Figure 2.17: PL enhancement at different temperatures and comparison of plasmonic resonance with PL enhancement. (a) PL enhancement for different structures at room temperature and (c) at cryogenic temperature (4K). (b) Superposition of peak positions of different measurements as a function of period: black square points are reflectance peaks, red closed circle points are transmittance dips, yellow up-triangles are PL enhancement peaks and light blue down-triangles are the absorption peaks defined as 1-R-T. (d) Ratio of PL enhancement at room and at cryogenic temperatures for three selective structures (Bordeaux: p = 700 nm, light blue: p = 500nm, and light grey: p = 450nm).

is varied from one structure to the other structure. The variation of PL enhancement can be understood as a competition between processes. As the period is reduced from 700 nm to 350 nm, the total number of CQDs interacting with the plasmonic resonance increases because the density of nanoring increases, so that we expect more light. However, as the rings are getting closer, their mutual coupling induces a broadening of the resonance, or lowering the quality factor, which in turn leads to a reduction of the PL enhancement. This trade-off results in a optimized enhancement of approximately 7 for our rings with period 600 nm.

The PL enhancement spectra present the same general characteristics as the optical properties of the nanoring arrays, as shown in Figure 2.17b. For all the structures, the wavelength of maximum PL enhancement is confined between the transmission and reflection peaks on one side and the absorption peak (defined as 1-R-T) on the other side. Figure 2.17b displays the peak positions of reflection (black square), transmission (red circle), absorption (light blue triangle-down), and PL enhancement (yellow triangle-up) for different structures. It can be seen that the PL enhancement peaks are always followed by the absorption peaks of the corresponding structure. We also carefully analyzed that these PL enhancement are not the results of measurement artifacts i.e. the scattering effects of the nanorings on the emitters and finite angle of collection of the objective.

We next repeat the measurement at 4.2K so that the nanoring arrays can interact with very bright emitters, see Figure 2.16a and section 2.2.3. The PL enhancement spectra, plotted in Figure 2.17c, have much smaller amplitude, in good agreement with common wisdom that plasmonic antennas and their associated losses are less efficient when used in conjunction with bright emitters. However, there is another feature of Figure 2.17c that is much less expected, namely that the PL enhancement spectra have essentially the same shape as those recorded at room temperature in Figure 2.17a. Such an observation is not expected according to the theoretical predictions of the two-level model.

A quantitative comparison between room and cryogenic temperatures can be made by plotting the ratio of the PL enhancement spectra of Figures 2.17a and 2.17c. The resulting curves, represented in Figure 2.17d, are remarkably flat and nearly identical for all structures, regardless of the position of the localized surface plasmon resonance and the actual period of the ring array. This result indicates that the PL enhancement spectra of Figures 2.17a and 2.17c are essentially proportional. Again, for the purpose of clarity, we only select to plot the ratio for three structures with period p = 450 nm (light grey), p = 500 (light blue), and p = 700 nm (bordeaux), but the features are the same for other investigated structures.

The proportionality between the curves of Figures 2.17a and 2.17c can also be visual-

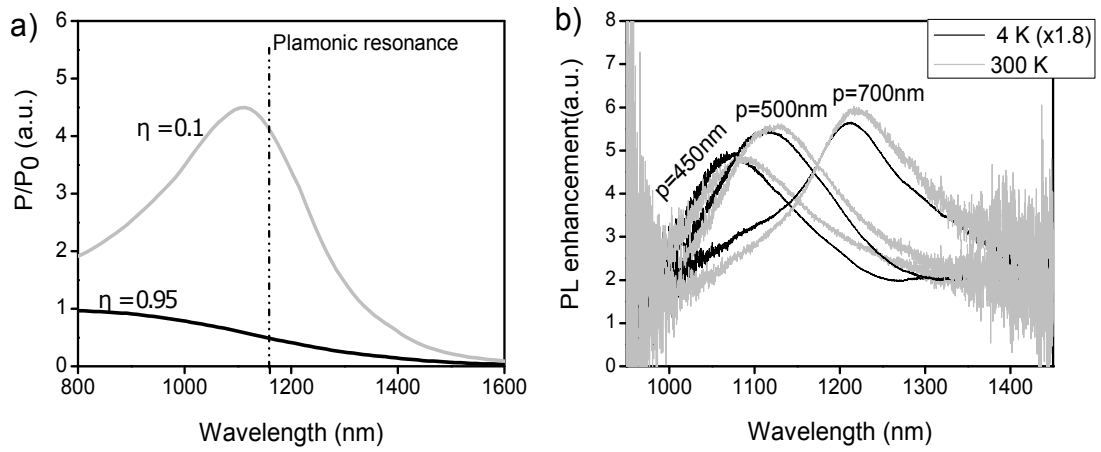

Figure 2.18: A comparison between the temperature-dependence measurements with theoretical predictions. (a) The theoretical prediction for spectral profiles of the metallic nanoparticle coupled with a bad ($\eta_i = 0.1$) and a good ($\eta_i = 0.95$) emitter in the condition of low pumping power. (b) PL enhancement for different structures at room and at cryogenic temperatures. It is reminded here that intrinsic quantum yield of the dots in host matrix at room temperature is almost $\eta_i \approx 0.1$), whereas their quantum yield at cryogenic temperature is nearly unity ($\eta_i \approx 1$).

ized on Figure 2.18b that superimposes the PL enhancements for the same three structures at room (light grey) and at cryogenic (black) temperatures. In this figure, all three PL enhancement at 4K are multiplied with a factor 1.8 – the factor is taken based on the Figure 2.17d. The proportionality between the curves measured at room and cryogenic temperatures is the central result of this study. The apparent simplicity of this observation is deceiving for one reason—it is at odds with the predictions of the two-level model discussed before and reproduced in Figure 2.18a. This figure says that the plasmonic antennas will only enhance the luminescence of a poor emitter, but that it will suppress the luminescence of very bright emitter like our PbS QDs at cryogenic temperature. This marked disagreement between our measurement data and theoretical predictions in Eq 2.10 proves that the currently used two-level model is not reliable to predict the behavior of the system – colloidal quantum dots that we are working on.

In fact, this conclusion is not so surprising since we have already established in section 2.2 that our PbS QDs in their HSQ matrix emit through two different radiative channels, namely their intrinsic excitonic recombination channel and a trap defect state. In other

words, our CQDs cannot be treated as two-level emitters. It is noticeable that the validity of the standard two-level model has also been challenged for fluorescent molecules [139]. The next section proposes a new theoretical model that accounts for these features. It has been developed by Professor Jean-Jacques Greffet as part of a collaboration on this project.

Before detailing this model, we note that a more critical examination of Figure 2.17d reveals that the measurements at room and cryogenic temperatures are not exactly proportional. To explain this result, it is important to note that we have neglected the influence of the temperature on the Au rings themselves in the discussion. As documented in a few studies, the plasmonic properties of nanoparticles with significant surface roughness such as our lithographied rings are only marginally affected by the temperature [140], except for a slight narrowing and blue shifting of the peak as T decreases. This is such a spectral evolution that we observe on Figure 2.18b.

2.7 Beyond two-level model

Our experiments indicate that PbS CQDs embedded in a sol-gel matrix have at least two radiative decay channels – one excitonic line and one defect state. To take this observation into account, we suppose in the following that each source emits light at two distinct frequencies ω_f and $\omega_f^{'}$ and suppose that there is no correlation between the two channels. The same conventions as above are used, except that all the quantities related to $\omega_f^{'}$ are identified with a prime (i.e. $\Gamma_R^{'}, \gamma_{r0}^{'}$, and so on ...). In this new model, the N emitters forming the system are characterized by the following distribution:

$$N = \int d\omega_f d\omega_f^{'} n(\omega_f, \omega_f^{'}) \tag{2.13}$$

where $n(\omega_f, \omega_f^{'})$ is the density of CQDs emitting at frequencies ω_f and $\omega_f^{'}$. The power radiated by the N sources at a given frequency ω_{f0} can be written as a contribution from

each channel:

$$P(\omega_{f0}) = k_{det}\Gamma_r(\omega_{f0}) \int d\omega_f n(\omega_{f0},\omega_f^{'})P(\omega_{f0},\omega_f^{'}) + k_{det}\Gamma_r^{'}(\omega_{f0}) \int d\omega_f^{'} n(\omega_{f0},\omega_f)P(\omega_{f0},\omega_f) \tag{2.14}$$

here $P(\omega_f,\omega_f^{'})$ is the probability of excitation of one CQD having the radiative decay channels ω_f and $\omega_f^{'}$. To calculate this quantity, we write the rate equation of the excited CQDs emitting at ω_f and $\omega_f^{'}$ under weak CW excitation:

$$\begin{aligned}\frac{d}{dt}[n(\omega_f,\omega_f^{'})P(\omega_f,\omega_f^{'})] = &-[\Gamma_r(\omega_f) + \Gamma_{nr}^{Ant}(\omega_f) + \gamma_{nr0}]n(\omega_f,\omega_f^{'})P(\omega_f,\omega_f^{'}) \\ &- [\Gamma_r^{'}(\omega_f^{'}) + \Gamma_{nr}^{Ant}(\omega_f^{'}) + \gamma_{nr0}^{'}]n(\omega_f,\omega_f^{'})P(\omega_f,\omega_f^{'}) \\ &+ \sigma_{abs}(\omega_{abs})I_{inc}|K(\omega_{abs})|^2 n(\omega_f,\omega_f^{'})\end{aligned} \tag{2.15}$$

Since this above equatiion is equal to zero for stationary regime, we have:

$$P(\omega_f,\omega_f^{'}) = \frac{\sigma_{abs}(\omega_{abs})I_{inc}|K(\omega_{abs})|^2}{\Gamma_r(\omega_f) + \Gamma_{nr}^{Ant}(\omega_f) + \gamma_{nr0} + \Gamma_r^{'}(\omega_f^{'}) + \Gamma_{nr}^{Ant}(\omega_f^{'}) + \gamma_{nr0}^{'}} \tag{2.16}$$

Let us introduce $\Gamma = \Gamma_r(\omega_f) + \Gamma_{nr}^{Ant}(\omega_f)$ and $\Gamma' = \Gamma_r^{'}(\omega_f^{'}) + \Gamma_{nr}^{Ant}(\omega_f^{'})$ to simplify the notation. We also note that the decay rates of both channels are subjected to the same enhancement factor in the presence of the antennas because the Purcell effect responsible for this enhancement is solely determined by the local density of photonic states of the system. We therefore have $\Gamma_r(\omega_f) = g(\omega_f)\gamma_{r0}(\omega_f)$ and $\Gamma_r^{'}(\omega_f^{'}) = g(\omega_f^{'})\gamma_{r0}^{'}(\omega_f^{'})$ so we can rewrite the equation $P(\omega_{f0})$:

$$\begin{aligned}P(\omega_{f0}) = k_{det}g(\omega_{f0})[\gamma_{r0}(\omega_{f0}) \int d\omega_f \frac{n(\omega_f,\omega_f^{'})}{\Gamma_r(\omega_f) + \Gamma_{nr}^{Ant}(\omega_f) + \gamma_{nr0} + \gamma_{nr0}^{'}}] \\ + \gamma_{r0}^{'}(\omega_{f0}^{'}) \int d\omega_f^{'} \frac{n(\omega_f,\omega_f^{'})}{\Gamma_r(\omega_f) + \Gamma_{nr}^{Ant}(\omega_f) + \gamma_{nr0} + \gamma_{nr0}^{'}}]\sigma_{abs}(\omega_{abs})I_{inc}|K(\omega_{abs})|^2\end{aligned} \tag{2.17}$$

This expression contains the terms γ_{nr0} and $\gamma_{nr0}^{'}$ which depend on the temperature —

but not on the frequency because they represent intrinsic characteristics of our emitters. In the limit where γ_{nr0} and $\gamma_{nr0}^{'}$ are much larger than any other terms of our integrals, they simply introduce a general scaling factor in the PL spectra since they do not depend in the frequency. In all other cases, their influence on the spectral shape of the photoluminescence is also weak because they appear in the integrals where their weight is minimized after integration over ω_f and $\omega_f^{'}$. We can make the latter statement because the spectral separation between the two emission bands is larger than the width of the plasmonic resonance, minimizing the contribution of γ_{nr0} and $\gamma_{nr0}^{'}$. Thus, this final equation correctly predicts that the PL signal is essentially proportional to the radiative enhancement $g(\omega_{f0})$, a result that remains true if we normalize this expression by the signal P_0 produced in the absence of the antennas (particularly, in this case $g(\omega_{f0})$, Γ and Γ' are set by 1).

The final equation provides a mathematical support to the main claims of this chapter. By taking into account the salient features of our CQDs including inhomogeneous broadening and the existence of at least two radiative channels per crystal, we obtain a boost in luminescence roughly proportional to the plasmonic enhancement, in a good agreement with the experimental results. However, it is also worth nothing that the final equation is a generic expression that does not necessarily capture the full physics of our experiments. In particular, we have neglected several factors such as the possible correlations between emission channels ω_f and $\omega_f^{'}$ and the fact that the antennas may also trigger additional radiative transitions.

2.8 Conclusion

In conclusion, we have performed a quantitative study on the interactions between a distribution of PbS QDs embedded in a host matrix that interacts with arrays of plasmonic antennas. Although similar structures have already been studied by others in a qualitative way [47, 48], we provide what we think is the first quantitative analysis on this class of

structures. The fact that the QDs are embedded in a dielectric host matrix represents a complication in the sense that complex chemical reactions continue to occur well after completion of the samples. Nevertheless, we were able to determine conditions in which the PL enhancement provided by the plasmonic antennas is remarkably stable over weeks. This stability enabled us to fully characterize the system and made us realize that it could not been described by the generic two-level model that is almost universally used to make educated guesses on the behavior of plasmonic antennas. The reason for this discrepancy is that the PbS QDs in their HSQ matrix are complex emitters that do not simply emit light through their excitonic emission line. Interestingly, the two-level model has also been challenged for a completely different system composed of plasmonic dimers interacting with organic fluorophores [139]. Although the emitters of this earlier study do not obey to the same emission dynamics as our PbS QDs and must be described a completely different theoretical model, the resulting PL enhancement follows the same behavior as in our experiments. It would be interesting to study other systems with other quantum emitters to explore the degree of universality of these results.

Chapter 3

All inorganic top-emission infrared QDLEDs

After the photoluminescence experiments of the previous chapter, I will now explain how to pump the same commercial PbS CQDs electrically. We have developed an architecture of quantum dot light emitting diode (QDLED) that is both compatible with our experimental tools and with the main objective of this thesis, namely the demonstration of hybrid metamaterial/CQD optoelectronic devices. The metamaterial/CQD hybrids will be introduced in chapter 4; here we will focus on the fabrication and characterization of reference QDLEDs without any metamaterials. As will be described in section 3.1, the community has introduced many variants of QDLEDs with ever-improving efficiency over the years. In this respect, the structures that we have fabricated are not fundamentally new, nor are their performances competitive compared to some of the best existing designs. Nevertheless, I have chosen to dedicate a whole chapter to QDLED fabrication and characterization because it was an expertise that did not exist in our group prior to my PhD thesis. In contrast to the rest of the QDLED community, our group has no expertise in chemistry and we also lack of some highly useful tools that other teams have, such as glove boxes with controlled/inert atmosphere. As a result, the challenges that I have encountered and the solutions that I have found are very specific to this particular

context and may serve as useful guidelines for others who wish to fabricate stable and reproducible QLEDs without having any specific infrastructure for it. While other groups synthesize their own CQDs and then fabricate QDLEDs in well-controlled environment, I worked with commercial PbS dots that are typically inferior in quality than house-made nanocrystals. Moreover, I had to devise a fabrication process and a QDLED architecture that is both reproducible and robust despite the fact that the fabrication was made under ambient air, i.e. with all the materials used subject to uncontrolled oxidation. Last, I had to imagine a QDLED design that emits light from the top of the structure, which is at odds with most QDLEDs introduced so far in the literature that produce light through a transparent substrate.

3.1 State of the art

QDLEDs are an evolutional type of LED where the p-n junction of traditional solid-state LEDs is replaced by a packed film of granular CQDs. The CQD thin film acts as an active layer emitting spontaneous light when the electrons and holes are electrically injected from the cathode and the anode, respectively. A typical QDLED also comprises an electron transport layer (ETL) and a hole transport layer (HTL) that are placed between the active QD layer and the electrodes. We will see later that these layers do not only transport carriers from the electrodes to the CQD film but also prevent unwanted electron-hole recombination outside the active layer.

3.1.1 QDLED as a next generation for many LED applications

Light emitting diodes based on colloidal quantum dots have received a great interest since the concept was introduced in 1994-95 [141, 142]. QDLEDs are a derivative of organic LEDs (OLEDs) invented in the late 1980s [143] and the first breakthrough after the initial demonstrations of the 90s came in 2002 when a record high external quantum efficiency $\eta = 0.52\%$ was achieved with a device architecture analog to that of an OLED in which the

active layer was a film of monolayer quantum dots [144]. Since then, the performances are improving regularly and state-of-the-art QDLEDs have external quantum efficiencies as high as $\eta \approx 20\%$ [108]. Nevertheless, it is admitted that QDLEDs are still in their infancy stage with laboratory research and development compared to commercial OLED technologies that have already entered the commercial market with the best OLEDs characterized by $\eta \approx 35.6\%$ [145]. Although the efficiency of OLEDs is still higher than that of QDLEDs, the latter are considered as having a higher potential for several reasons. In particular, QDLEDs can be made by solution process except from the electrodes and they do not require a high purity material to work. This is a significant advantage compared to OLEDs where the purity of the materials is key for operation, performance, and efficiency. It should also be stressed out that many aspects of QDLEDs have not been fully exploited and understood yet and thus there is a plenty of room for improvement of such devices. Here, I would like to briefly discuss some of the main properties that drive the research of people interested in QDLEDs. More details can be found in good reviews [146, 147, 148].

Among the QDLED qualities that sparks the interest of the community is their pure color of emission (narrow emission bandwidth), their color emission tunability over a significant spectral range and their brightness. As discussed in chapter 1, the electronic structure of CQDs is governed by the quantum size confinement. Thanks to the advances in chemical systhesis, it is now possible to obtain a solution of CQDs with monodisperse size distribution (the variation of the dots diameter is smaller than 5 %) [151, 81, 152], leading to a narrow spectra of emission and pure color emission.

The second set of advantages of using CQDs in LEDs or other optoelectronic devices is an economic reason and their versatility in use. High performance devices are still dominated by epitaxial structures that require expensive molecular beam epitaxy, high cost of operation, maintenance and expensive materials for certain frequency ranges. In contrast, CQDs are prepared by chemistry synthesis and can be fabricated at room temperature and pressure with low cost techniques like roll-off [153, 154], spin coating [106, 155], spray coating [156, 157], jet printings [158, 159], or even painting [160].

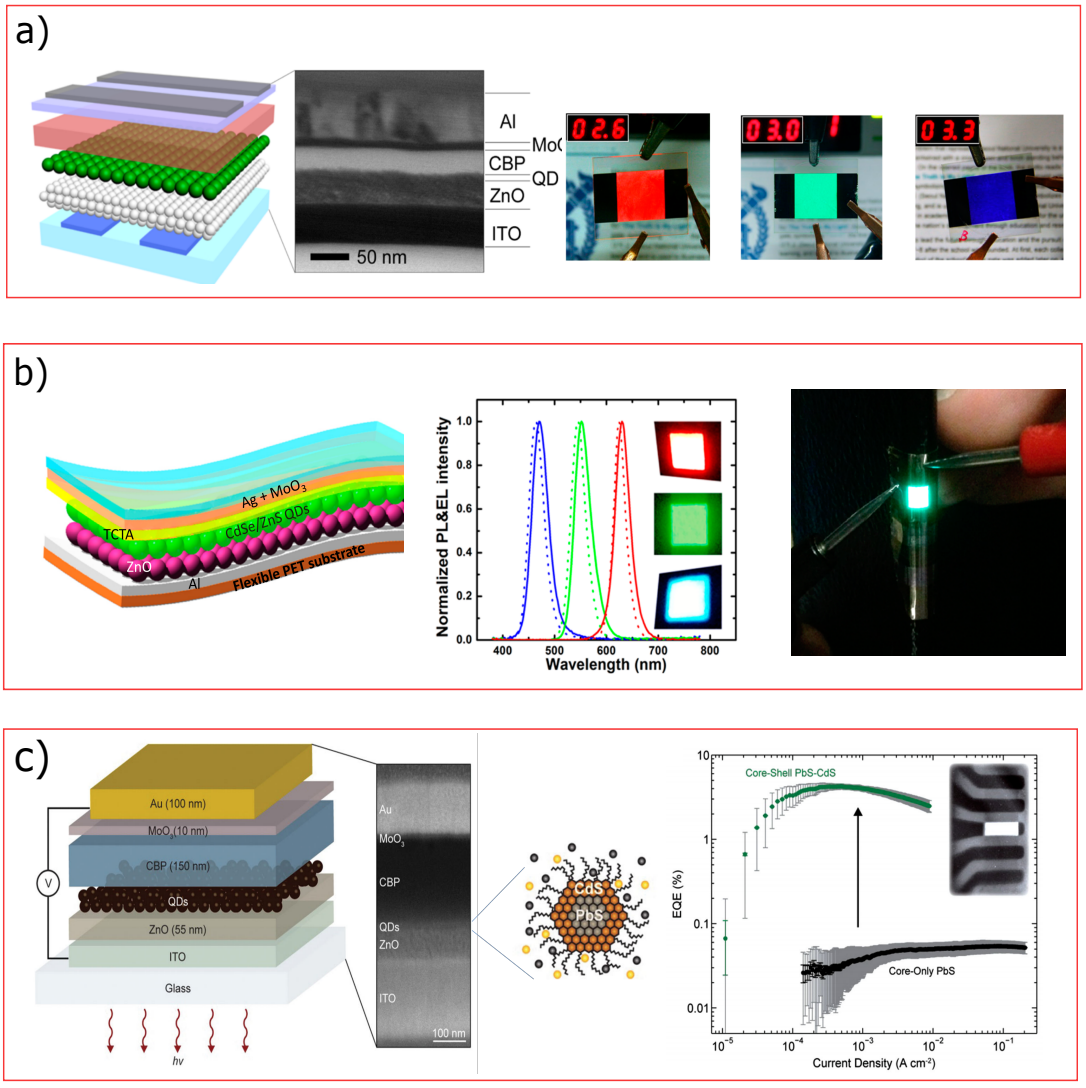

Figure 3.1: Capturing some of the state-of-the-art QDLEDs in the literature so far. a) An inverted device structure for bottom emission [118]. b) A flexible and top emission QDLED fabricated for sticker applications [149]. c) An infrared QDLED for bottom emission using core/shell structure to increase the efficiency [150].

Stability of CQDs to environmental conditions is also one of the properties attracting the attention of researchers. Although studies showed that photostability of CQDs is affected to a certain degree by the presence of oxygen and humidity, material scientists and chemists are able to preserve or even dramatically improve the photostability of CQDs by many strategies, for example by encapsulating the core CQD by a shell of a wider bandgap semiconductor , a radially graded alloy shell or by passivating the ligands

around the dots [161, 118, 162], or, more recently, by synthesizing the dots with inorganic ligands [163].

3.1.2 QDLED architectures

Similarly to OLEDs, QDLEDs are based on vertical stacking architectures with one electrode often made by a low workfunction metal and another electrode made of a transparent oxide. Two categories of QDLEDs can be defined depending on the emission direction. Regardless of the exact architecture, if the light is coming out of the device from the substrate, it is called bottom emission; if it is emitted towards the top of the stack, then it is called a top emitting diode. Here, in this section we review some pros and cons of each configuration.

Bottom emission QDLEDs

Bottom emission limits the light output coupling with other devices and also poses challenges if one wants to integrate QDLEDs in circuits. Despite these drawbacks, this configuration is still the mainstream in QDLED research because it is inherited from the more mature OLED technology and is much easier to implement than top emission QDLEDs. The typical architecture of bottom emitting devices can be seen in Figure 3.2a where a transparent anode is supported by a transparent substrate and the top electrode is an opaque metallic layer reflecting the light toward the substrate [106, 164, 155].

Top emission QDLEDs

In parallel to the bottom emission, there have also been a few examples of top emission QDLEDs [149]. For many display panels that require an active matrix to control the lighting, this can be achieved with top emission. In addition, this top emission configuration increases the light coupling capability and can be adapted to current dominant silicon technology since the cathode, typically made of opaque metal, is placed on the substrates. This will be a distinct advantage since it allows to integrate LEDs into a circuitry

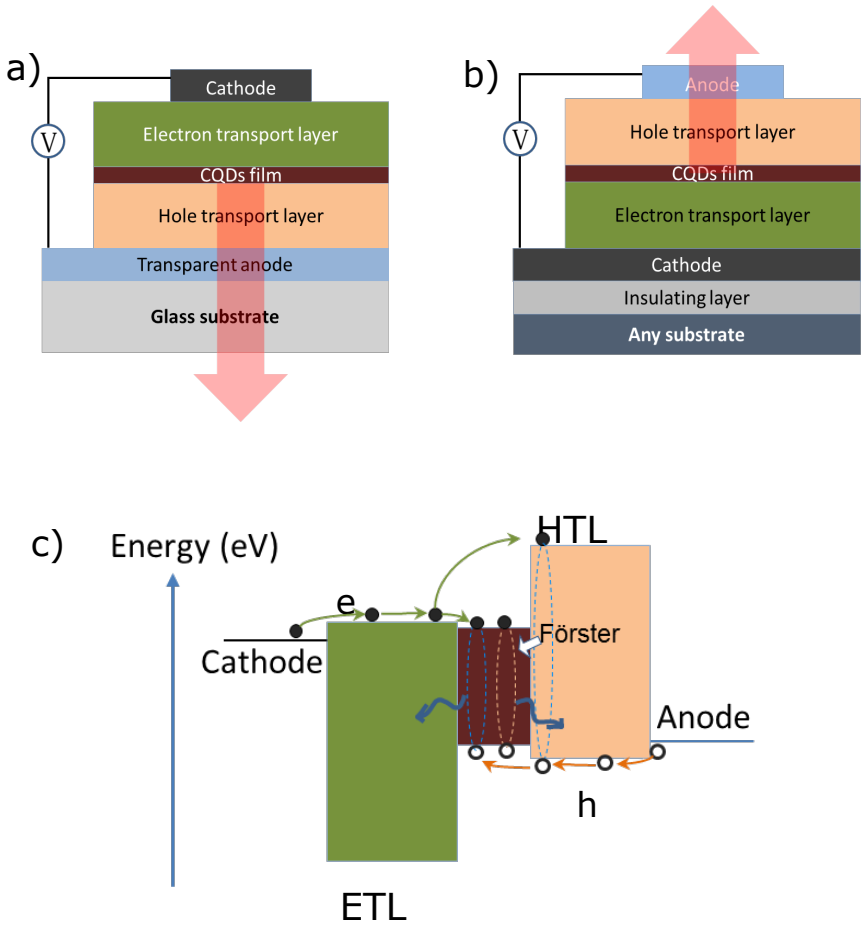

Figure 3.2: The two common architectures of QDLEDs. a) Bottom emision QDLED where the light is transmitted through a transparent anode and glass substrate. b) Top emission QDLED where light only travels through a transparent/semitransparent anode. This type of QDLED enables a higher light coupling and offers more versatility for fabrication on any type of substrate. c) The working principles of QDLEDs. Radiationless energy transfer and charge direct injection are the two main mechanisms behind the operation of the devices depending on the materials of the carrier transport layers.

with other components like transistors on a single Si substrate. The advantage of the top emitting devices can be illustrated in Figure 3.2b. The fabrication can be conducted on any kind of substrate as long as there is an insulating film so that the current from the cathode will not be leaked in the substrate. The thin transparent anode is the top layer and the reflecting cathode at the bottom can significantly reduce the absorption of the electroluminescence.

3.1.3 Working Principles

It was originally thought that the CQDs films serve as a recombination zone for the electrons and holes injected from the anode and the cathode [144]. However, Anikeeva *et al* showed that there are two mechanisms, direct charge injection and Förster energy transfer, see Figure 3.2c, impacting the recombination and luminescence efficiency of QDLEDs when the CQDs film is sandwiched between an organic electron transport layer and an organic hole transport layer [165, 166].

In direct charge injection, electrons and holes are generated from the cathode and anode, respectively, under a properly applied voltage. The transport layers bring their corresponding charges into the CQD layer, where they form an exciton that recombines radiatively or non-radiatively. The transport materials are chosen not only to carry one type of carriers towards the QD film, but also to prevent short-cicuit by blocking the migration of the charge carriers with opposite sign. Moreover, a study in which the CQD film was deliberately positioned at various positions within either the organic HTL or ETL revealed that the highest luminescence efficiency was achieved when the CQD film was slightly offset within the HTL [165]. This result indicated that there was another process which contributed significantly to the radiative recombination in addition to direct charge injection. To clarify this point, the authors of this work varied the distance between the CQD film and the interface of the organic HTL and ETL and found that the highest luminescence efficiency was obtained when the distance was smaller than the radius of Förster energy transfer. The systematic study illustrated that both direct charge injection and Förster energy transfer contribute to the external quantum efficiency of QDLED with organic transport layers.

Recently there has been an increasing interest for replacing the organic transport layers by inorganic layers that are air-stable and characterized by a higher conductivity [106, 167, 113]. Moreover, it has been shown in [113] that QDLEDs with inorganic transport layers operate through direct charge injection only. There has also been some unconventional way of using inorganic charge transport layers made of isolating materials

in which injection was obtained by a field-driven mechanism rather than direct charge injection [168, 169].

3.2 Fabrication of top-emission QDLEDs

3.2.1 Motivations and fabrication strategy

As discussed above, top-emission QDLEDs have been the object of recent interest because of certain advantages compared to the bottom-emission QDLED such as light output coupling, versatile substrates to use, feasibility to integrate into several technologies. Besides, a practical reason that drove us to pursue top-emission LEDs is that our characterization tools are well adapted to this configuration. However, building QDLEDs with top emission poses many difficulties. When I started to work on QDLEDs in October 2013, no top-emission QDLEDs has been reported at that time to the best of my knowledge. To define a fabrication strategy, we first looked at the OLED literature in which a few top-emission architectures have been published [170, 171, 172, 173]. However, the materials and the fabrication methods of these studies were impossible for us to implement at that time. Some of these structures have more than 5 layers and it did not seem reasonable to pursue such highly complicated architectures for a starting point. Other designs were much simpler but the materials used were not compatible with our fabrication facilities. Because of these difficulties, we abandoned the idea of adapting an OLED architecture and tried instead to revert the fabrication order of the bottom-emission QDLEDs published in [155].

However, reverting a bottom-emission architecture is not necessarily trivial since it requires to change the stacking order of layers made of very different materials. In the process, we have encountered many issues related to adherence, wetability, uniformity and material compatibility that prevented us from simply inverting the bottom-emission design of Refs. [155]. The following section details our choices, the techniques we tried to make each layers, the problems that we encountered and how we solved it. In the end,

our final structures turned out to be quite different from what we had originally in mind.

3.2.2 Fabrication of working and reliable top-emission QDLEDs

The cross-section of our top-emission QDLEDs is depicted in Figure 3.2b. It consists of a bottom cathode, an ETL, an active CQD film, a HTL and a transparent anode through which light is emitted. In practice, we fabricate the LEDs on 1 cm x 1 cm substrates. The substrates are either made of glass or made of Si coated by an insulating layer of silica deposited by Plasma Enhanced Chemical Vapor Deposition (PECVD) at 380 kHz, 300 ^{o}C and a deposition rate of 11 Å/s. The glass substrates and the silica-covered Si substrates can be used interchangeably in our fabrication process. We fabricate 12 independent LEDs on each 1 cm x 1 cm sample by creating a matrix of 4 longitudinal cathode stripes and 3 vertical anode stripes. The other layers between the anodes and cathodes cover the sample homogeneously. The following subsections discuss the material choice and fabrication for each of the layers and a detailed summary of the whole fabrication procedure can be found in Appendix C.

Fabrication of cathode

For the bottom electrode, which is a cathode in our case, we select Al as the material for injecting electrons into the active layer. As illustrated in Figure 3.2c, the working function of the cathode should be as small as possible so as to facilitate the injection of electrons into the active layer. Unlike other good conducting metals, Al has a low working function of ≈ 4.3 eV compared to Au (≈ 5.3 eV), Ag (≈ 4.6 eV), Cu (from 4.5 - 5.1 eV depending on the crystal phase), and Pt (≈ 5.8 eV) [174]. In fact, the exact workfunction of our Al electrodes is slightly modified by the fact that the samples are exposed in air, resulting in a thin layer of natural oxide at the Al surface. In order to generate four 500 µm in wide Al stripes, we aligned our substrate with a shadow mask comprising four rectangular voids at the location of the cathodes. We have tried two vacuum based techniques: the first one consisted in DC sputtering Al at 8 µbar in inert gas; however with this technique we

sometimes obtained stripes with black terminations caused by an uncontrolled source of contamination. For this reason, we permanently switched to electron-beam evaporation under better vacuum conditions (p $\approx 10^{-5}$μbar). Al is evaporated at a rate of 12 Å/s to minimize the surface roughness. Finally, four Al stripes (80 nm thick, 500 μm wide and 1 cm long) are generated with e-beam evaporation without any thermal post-treatment. It is noted that Al has a higher thermal expansion coefficient than other noble metals so that it is more difficult to maintain a constant evaporation rate if one does not heat the Al source gradually.

Fabrication of the electron transport layer

The ETL is chosen based on some guidelines. First, the ETL should have a suitable energy bandgap diagram so that the electrons originating from Al cathode can be injected into this transport layer while blocking the migration of the holes originating from the top anode. The transport layer should also have a decent conductivity either through good carrier mobility or electron tunneling. With these requirements in mind, we have selected TiO_2 as the ETL which has the ionization potential (valence band level) at approximate 7.8 eV, its band gap 3.9 eV, and carrier mobility of 1.7 x 10^{-4} cm^2 V^{-1} s^{-1} [164]. For this transport layer, we tried three different approaches to realize it.

First, we tried sputtering a Ti target (99.99%, Kurt J. Lesker) in a Denton chamber with O_2 reactive gas in DC mode at a rate of 0.2 Å/s and percentage of Oxygen in total gas is 42 %. This recipes give us a layer of TiO_x. An Energy-dispersive X-ray (EDX) spectroscopic analysis is performed with a Philips XL 30S machine and confirmed that the chemical composition of Ti and Oxygen are almost the same at different positions of the sample (atomic percentage of Ti and Oxygen on average are 30.28% and 69.72%, respectively, corresponding to $Ti:O_{2.3}$). The advantage of this technique is that we can obtain a uniform thin film of TiO_x with very low surface roughness. Yet, as will be shown later with Figure 3.11, we discovered that such TiO_x coatings had very poor conducting properties and lead to unstable device performance. These problems can be attribted to

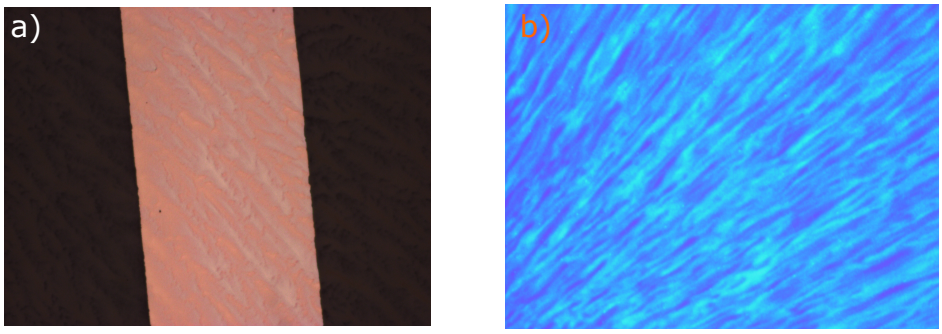

Figure 3.3: The striation defect as spincoating TiO_2 occurred in open spincoater. a) TiO_2 solution is spincoated on Al cathode. b) It was coated on a bare substrate. This problem disappears if the layer is spincoated in a saturated air of parent solvent with a closed spincoater.

the fact that we do not control the phase of TiO_x with this method: as is well-known, only the anatase phase of TiO_x leads to interesting electronic and optoelectronic properties. In comparison, the other possible phase of TiO_x (the rutile phase) as well as amorphous titania are known to perform poorly and are not adapted to optoelectronic devices.

The second attempt that we have made to achieve a better conducting thin film of TiO_2 is spincoating an anatase crystalline form of TiO_2 paste purchased from Dyesol (Titania paste, 18NR-T). Unfortunately, this product is meant for realizing thick films of TiO_2 and the film needs to be sinterred to achieve the desired conductivity. Efforts of further diluting the Titania paste to reduce the thickness of the film wer not successful.

The third strategy which finally brought us satisfaction both in terms of thickness and electrical conductivity is fabricating a mesoporous TiO_2 film by spin-coating a solution of anatase titania nanoparticles (10-12 nm in diameter) in ethanol purchased from Solaronix on the sample. We have tried this approach after having discovered that it had been successfully used in [175]. However, the first attempts proved only partially satisfying because spin-coating the titania solution always resulted in a macroscopic striation pattern, as illustrated in Figure 3.3. This striation causes a significant modulation of the thickness across titania film and arises from non-uniform solvent evaporation during the

spin-coating step. Striation is a problem commonly encountered while spin-coating liquid solutions onto a substrate and a number of strategies had been proposed to eliminate this problem [176, 177, 178]. For example, a secondary solvent with lower volatility and higher surface tension compared to the parent solvent EtOH (Acetonitrile, Iso-propanol etc) may be included in the solution so that the secondary solvent will evaporate before EtOH. Another technique relies on saturating the atmosphere with the parent solvent by pouring the parent solvent in the bowl of the spincoater and covering the sample with a big cup. It worked in other works but not in our case even if we have tried with two different batches of anatase titania. Finally, we were able to eliminate the striation defects totally by completely changing our physical spincoating conditions. We switched to another spin-coater that operates with a closed lid instead of an open lid, covered the spin-coater bowl with an ethanol-soaked tissue to saturate the atmosphere with EtOH and dispersed a pure Solaronix solution at 5000 rpm for 60s to obtain the layer. As will be shown in Figure 3.7a, the layers thus obtained are of high quality.

Fabrication of the active layer

Upon completion of the electron transport layer, we coated it with a granular film of PbS CQDs by spincoating a solution of PbS nanocrystals in toluene purchased from Evident Technologies at 2000 rpm for 15 seconds. The concentration of dots in the solution is 26 mg/ml, their diameter is 5.3 nm and they are surrounded by 2 nm of trioctylphosphine oxide (TOPO) ligands. After spin-coating the solution in a fume hood under ambient atmosphere and performing a hot-plate bake at 150 C for 3 mins, a CQD film with an average thickness of 15 nm was obtained.

Figure 3.4 shows high-magnification top views of our films, showing excellent self-assembly and no cracks. Note that contrarily to other groups, we did not try to increase the compactness of the film by changing the initial TOPO ligands with shorter chains.

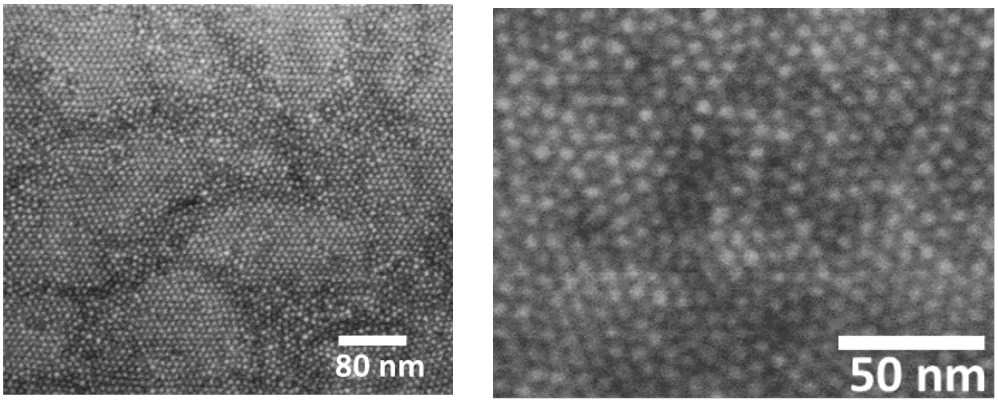

Figure 3.4: The carpet of PbS CQDs film. The SEM images of PbS QD film show a continuous assembly of the dots was formed after spincoating, and there is no big voids that might cause electrical short circuits.

Fabrication of the hole transport layer

The next layer in the stack is the HTL. Similarly to the electron transport layer, the HTL is selected in such a way that it satisfies two requirements. The bandgap diagram of the hole transport material should have proper energy values so that it favors hole injection within the CQD films while at the same time preventing electrons originating from the bottom Al cathode from recombining outside the CQD zone. There are a number of materials that can be selected to satisfy these requirements and our first choice has been dictated by identifying those that were the easiest to process.

Our first attempt has been to fabricate a HTL with the pi-conjuguated conductive polymer PEDOT:PSS in a aqueous solution. We used two different sources of PEDOT:PSS for our tests, one from Sigma-Aldrich and the other from Heraeus Precious Metals. PEDOT:PSS is a choice material in optoelectronics because it can be simply spin-coated on the sample and has excellent semiconducting properties. In the QDLED literature, in particular, it is very often used as a HTL for bottom-emission architectures. In bottom-emission architecture, the CQD film is coated after fabrication of the PEDOT:PSS layer while the reverse is true in our case. As it turned out, reversing the order of fabrication of the two layers resulted in intractable problems.

The first issue that we encountered while trying to apply a layer of PEDOT:PSS on top of our CQD film is a problem of wetability that resulted in highly inhomogneous coatings. This problem arises because of the very high surface tension of PEDOT:PSS dispersed in water. In order to remedy this problem, we have made several tries that are feasible in our cleanroom. For example, we repeated the spincoating multiple times until it fully covered the QDs film. However, the problem of uniformity was still high with this technique and the average film thickness too high for efficient carrier injection. Another way to reduce the surface tension of PEDOT:PSS is to introduce an additive in the parent solution of PEDOT:PSS such as monovalent alcohols (ethanol, iso-propanol) which does not change the conductivity of PEDOT:PSS film [179] while improving the wetability. With this technique, we were able to obtain a uniform thin film of filtered PEDOT:PSS on our CQD films. Alternatively, we found that we could also reduce the surface tension of the polymer film by spincoating EtOH or IPA prior to PEDOT:PSS application so as to modify the surface states of the CQD film.

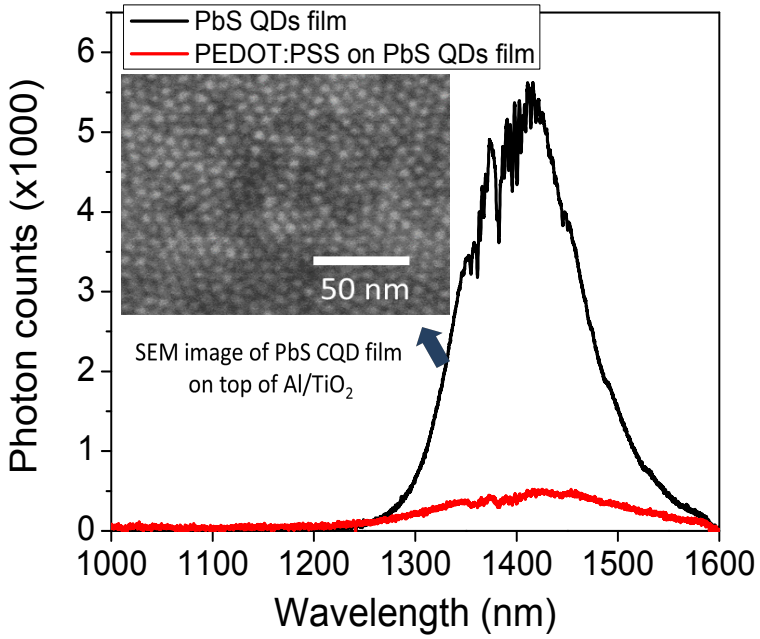

Figure 3.5: PL of PbS QDs film with and without PEDOT:PSS layer on top. The black curve is the PL of CQD film by spincoating. The inset shows the top view image of CQDs. The red curve denotes the PL after a layer of PEDOT:PSS had been coated on top of the CQD film.

However, despite this success, we realized afterwards that the PEDOT:PSS solution is so acid (pH $\approx$ 1.8) that it dissolved the PbS CQDs rested underneath. This problem can be seen on Figure 3.5 which shows that the photoluminescence (PL) spectrum of a PbS CQD film disappears almost entirely after coating a layer of PEDOT:PSS on it, indicating that the dots are either dissolved or melted by the pi-conjugated polymer.

Failure of using PEDOT:PSS as a HTL pushed us to find an alternative material for transporting the holes. Based on the available literature, we identifed MoO_x as a viable replacement. MoO_3, or MoO_x, in the case of oxygen deficiency, is used in QDLED devices and typically formed by either thermal or e-beam evaporation of molybdene oxyde [118, 180, 181, 182, 183]. Because this material is not available in the various deposition machines of the IEF cleanroom, we opted to grow the HTL by sputtering a Mo target in the presence of oxygen in a Denton sputterer. To reduce the impact of oxygen on the CQD film, a tradeoff had to be found between the sputtering power and the sputtering time. The lower the power used, the better for keeping the quality of the CQD film because it minimizes the collisions on the sample. However, lowering the power leads to a lower deposition rate, which in turn imposes a longer exposure time of the CQD film to oxygen. The conditions that we finally adopted were sputtering a Mo target (99.98 %, Kurt J. Lesker) in a (15% O_2 and 85% Ar) gas environment at a relative pressure 10 µbar and a rate 0.2 Å/s. EDX analyses of our sputtered layers reveal that the oxide is made of MoO_2 and MoO_3.

Fabrication of the top anode

The top anode is made of Indium Tin Oxide (ITO), an optically transparent material currently used in optoelectronics. Similarly to the four bottom Al cathodes, we use a shadow mask to define 3 ITO stripes per sample. These stripes are rotated by 90 degrees with respect to the Al cathodes, resulting in a matrix of 12 LEDs after completion of the sample.

The ITO deposition is made with the same Denton sputterer previously used for

growing the MoO_x HTL. This step has proven suprisingly difficult to harness because of several competing factors that had to be satisfied simultaneously. First, the resistivity of the ITO layer must be as low as possible. This can be in principle achieved with amorphous ITO coatings or polycrystaline coatings with large grains that have much less trap states than polycrystaline coatings with small grains. Second, the ITO electrodes are patterned on top of a multilayer structure so it is important to minimize the internal stress that may compromise the stack. Such conditions are usually met with polycrystaline ITO coatings with very small grains, i.e. with poor conductivity.

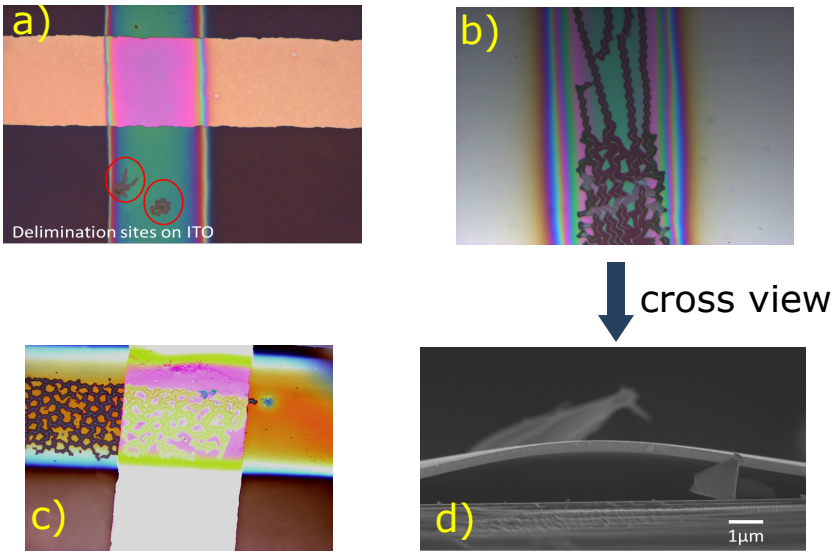

Figure 3.6: Delimination defects of sputtered ITO on soft film of PEDOT:PSS. a) Delamination sites appear immediately after sputtering. b) The delamination of ITO on PEDOT:PSS immediately after sputtering or in some cases the delamination was a consequence of propagation of delaminated sites due to the applied potential. c) The delamination appears outside and onsite of the overlapping between ITO and Al electrodes. d) The cross section view of ITO delamination on PEDOT:PSS, where delaminated ITO does not adhere on Pedot.

In order to solve these conflicting requirements, we conducted a series of tests on samples with PEDOT:PSS as the underlying HTL. As explained above, PEDOT:PSS turned out to be a wrong choice and we eventually switched to MoO_x but we did not realize this while we were developing our recipe for the ITO electrodes. However, the following discussion and conclusion remain valid for samples with MoO_x as the underlying

HTL.

Sasabayashi *et al* showed that a powerful mean to control the composition of ITO coatings was to adjust the pressure conditions during sputtering [184]. For polycrystalline films, the higher sputtering power, the larger grain size of ITO can be obtained, thus a better conductivity but typically a larger internal stress ensues. We first try to sputter ITO at a moderate pressure (8 µbar), for which a 100 nm thick polycrystal is formed, and with a power density 1.75W/cm^2 at a rate of 2.7 Å/s. However, the ITO stripes always showed delamination with this recipe, as illustrated on Figure 3.6. The delamination can be seen as soon as we finish sputtering ITO, either at isolated sites as in Figure 3.6a, or in a more invasive way as in Figure 3.6b. And even if the initial delamination is low, is will spread over all the electrode upon application of a bias voltage as shown on Figure 3.6c. For the sake of documentation, we show in Figure 3.6d a scanning electron micrograph of a sample cross-section exhibiting delamination: clearly, the ITO is bent above the underlying HTL, a sure sign of high internal stress.

To enhance the mechanical adhesion between the ITO anode and the HTL, we have adopted a two-step sputtering deposition in sequence at the same pressure condition of 8 µbar. The first step is carried out at lower power density (0.65 W/cm^2, rate 0.5 Å/s) so that smaller ITO grains are formed on top of the HTL, resulting in a 10-nm thick layer with less internal stress. We then sputtered a thicker (80 nm) and less resistive layer at the power 1.75 W/cm^2 and a deposition rate of 2.7 Å/s. As showed in Figure 3.7, ITO sputtered by this two-step technique completely solved the delamination problem.

All these developments were performed with PEDOT:PSS as the underlying HTL. We kept the same two-step strategy after we switched to HTLs made of MoO_x and were equally successful.

It is noted here that when ITO is sputtered as the last layer of the stack, its work function is significantly smaller than the values reported in the literature. In devices where ITO is used as the bottom electrode, it is typically processed with surface treatments such as an ozone bath and/or oxygen plasma to increase the working function to 4.6 - 4.8 eV.

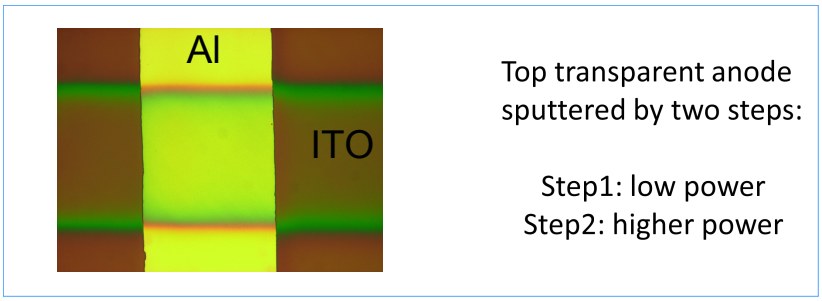

Figure 3.7: Delamination-free sputtered ITO was achieved by two-step processing instead of one sputtering process. A two step procedure of sputtering with lower power first and increasing the power after that reduced the mechanical stress to maintain a good stitching with the layer underneath.

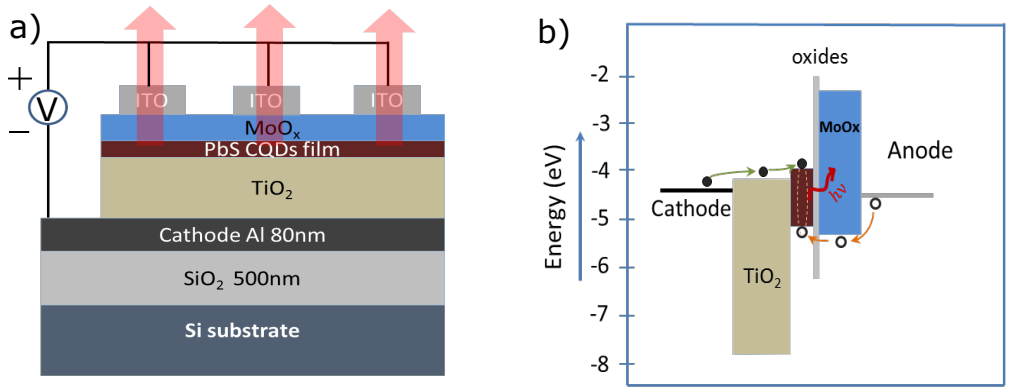

Figure 3.8: Schematic of the final QDLED device and its working principle. This final architecture is quite different from our initial design based on related articles in the literature. a) The final architecture of top emitting QDLED begins with a reflective cathode of Al, a layer of transporting electrons - TiO_2, an emitting layer of PbS QDs, a layer of transporting holes - MoO_x, and top layer is a transparent anode ITO. b) The energy level diagram of the device and the charge direct injection is responsible for the working mechanism of the device.

In contrast, it has been documented that as-sputtered ITO without any further surface treatment has a lower work function of 4.3 eV [185, 186]. Such is the case of our samples and this lower work function creates a higher potential barrier between the MoO_x HTL and the ITO anodes. To reduce this barrier, it is possible to insert a thin buffer layer of high work function metal (e.g. Pt, Pd or Au) between the MoO_x and ITO layers [187, 188]. We have verified that this strategy also worked in our case and resulted in LEDs with lower resistivities. However, we preferentially worked without this extra buffer

layer for two main reasons—first, to speed up the fabrication cycle and second, because even a non-continuous thin film of Pt, Pd or Au significantly increased the opacity of the stack.

3.2.3 Summary

To sum up the fabrication procedure, we finally obtained a viable architecture after numbers of trials and errors. The final composition of our top-emitting QDLEDs is illustrated in Figure 3.8a. It includes an opaque Al cathode (80 nm), an ETL of mesoporous anatase TiO_2 with a thickness of 60 nm, an emitting layer of PbS CQDs with a thickness of approximately 15 nm, a 10 nm thick HTL from MoO_x, and a 90 nm thick transparent anode made of a bilayer of ITO. We can plot roughly the energy level diagram of the device, as shown in Figure 3.8b. The energy diagram of the inorganic QDLED ensures that the operation of the LED is only through the direct charge injection, where the closed black circle denote injected electrons from cathode, whereas opened circles illustrates the injected holes from anode. A detailed recipe of the working devices is given in Appendix C. Now it is time to discuss and quantify the behavior of the devices that we have made.

3.3 Characterization of top-emission QDLEDs

To characterize our samples, we rely on a combined photoluminescence (PL) and electroluminescence (EL) measurement setup depicted in Figure 3.9. There are two kinds of sources to pump the QDLEDs: one is a continuous He-Ne laser emitting at 632.8 nm to characterize the PL spectra of QDs, the other is Keithley 2636A sourcemeter for taking EL images and recording EL spectra.

The PL or EL signal originating from the sample is collected by an IR-coated objective mounted to a microscope (Olympus BX51 WI) and sent either towards an IR camera (Xenics-Infrared Solutions) for imaging or towards a Jobin-Yvon grating spectrometer coupled to a nitrogen-cooled InGaAs detector (Jobin-Yvon Symphony II) to obtain spectral

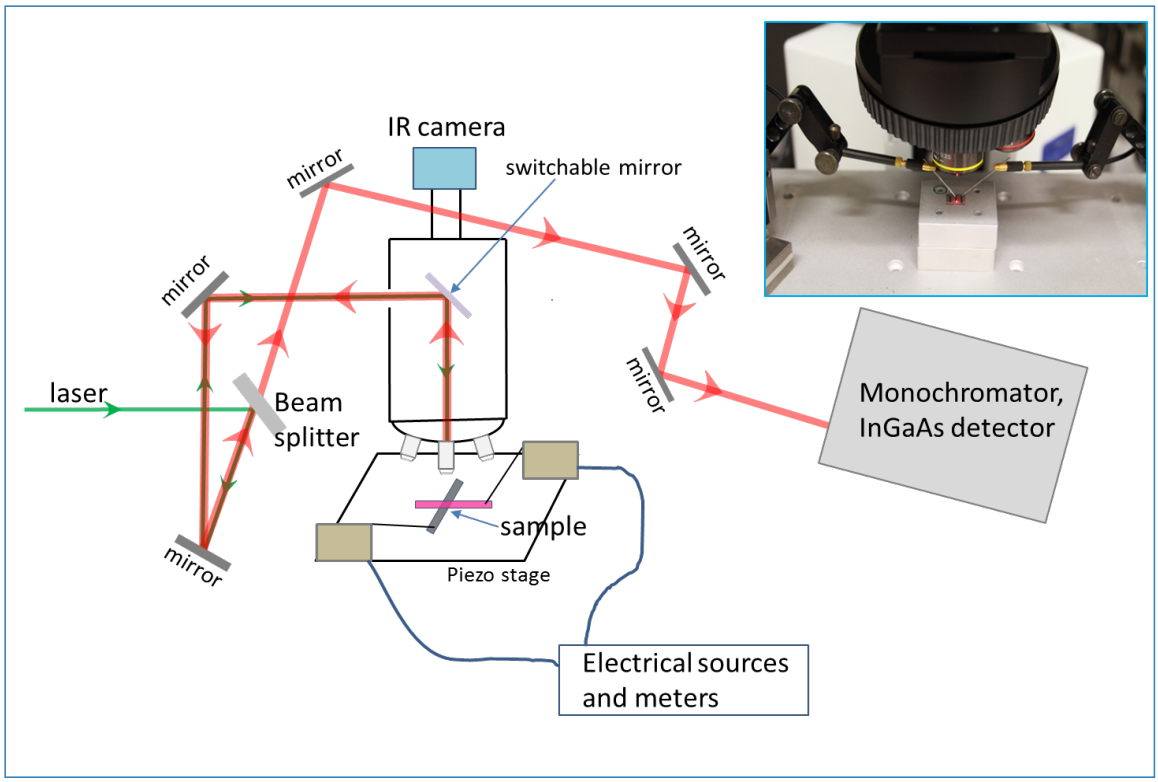

Figure 3.9: Experimental setup used for measuring the EL images, EL and PL spectra. Since we are working with top-emission QDLEDs, it is not necessary to require an inverted microscope. A normal microscope is the central part of the setup to perform all tasks. The inset captures a part of the setup while recording PL spectrum.

information. A switchable metal-coated mirror is used for switching between recording EL images and collecting EL spectra and a special beam splitter is used to separate the red laser light pump from infrared signal of the CQD. The inset of Figure 3.9 displays an image of a part of setup while imaging EL and collecting EL spectral data.

We first briefly comment on the QDLEDs that used sputtered TiO_x as an ETL. Figure 3.10b shows that the device lights up under positive bias voltage with a square pattern that corresponds to the intersection of the ITO and Al. We also verified that no light appears under reverse bias voltage. Combined with current-voltage characteristics of this devices, plotted as a black curve in Figure 3.11, we can state that our QDLED has rectifying behavior, proving that we have successfully fabricated an all-inorganic QDLED. Yet, a considerable limitation of this LED with sputtered TiO_x serving as ETL is its poor

stability. For example, if one keeps the voltage constant at 9 V, which is 2 V higher than the threshold level of this device, the infrared light of the QDLED fades quickly away and become almost dark after 15 minutes, see Figure 3.10b.

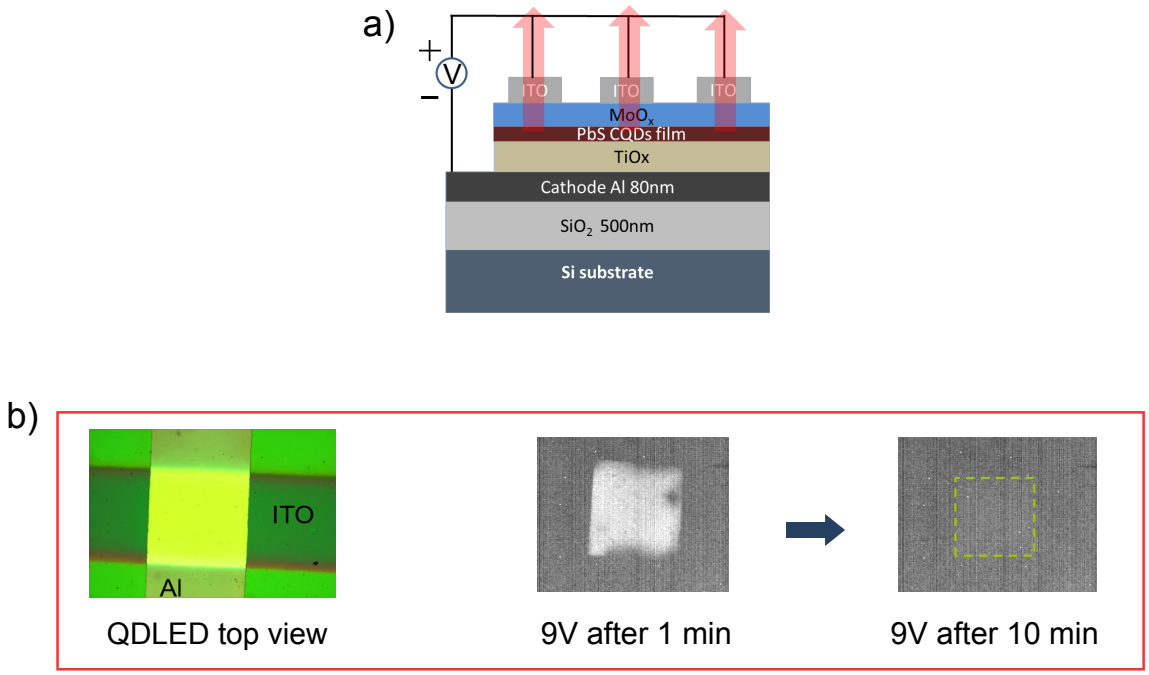

Figure 3.10: The performance of the all-inorganic QDLED with sputtered TiO_x serving as the electron transport layer. a) The architecture of the device. b) The optical image of the device and its performance. The electroluminescence images show that the luminescence fades away very fast.

As explained in the previous section, the main culprit for these poor performances is that our ETL made of sputtered TiO_x is not in an anatase phase, which is the only phase that is compatible for electronics and optoelectronics. For this reason, we have permanently switched to ETLs made of mesoporous layers of anatase TiO_2 nanoparticles. Figure 3.11 compares the characteristics of QDLEDs with sputtered TiO_x and anatase TiO_2 ETLs: clearly, both the I-V curve and the infrared light intensity are significantly better in the latter case. In addition, QDLEDs with anatase TiO_2 ETLs are stable, as will be discussed later with Figure 3.13.

At this stage, we have experimentally demonstrated that we were able to produce a stable and working top emitting QDLED. To further optimize the device, we have adjusted the thickness of the MoO_x HTL, as shown in Figure 3.12 where the current characteristics

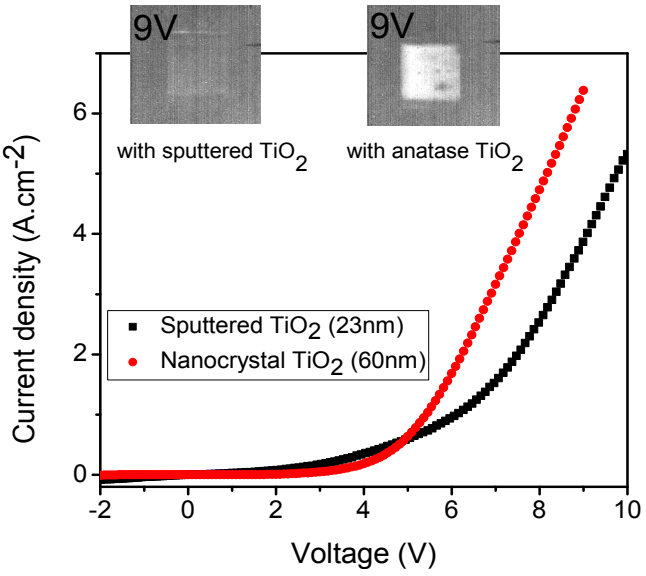

Figure 3.11: The comparison of the QDLED's performance between two materials serving as ETL: a thin (23 nm) sputtered amorphous TiO_x and a thicker (60 nm) anatase spin-coated TiO_2 nanoparticles. The current-voltage comparison of the devices with two ETL materials and the EL images of the corresponding device. Note here that all the other layer are processed in the same batch, experience the same conditions except the ETL. The images are EL of QDLEDs recorded at 9V after 5 minutes.

of two structures with 40 nm and 10 nm of MoO_x are plotted. The I-V of the QDLED with 10 nm of MoO_x (red curve) shows a better rectifying behavior and a higher current compared to the device with a thicker (40 nm) MoO_x layer. We also observed that the luminescence of the QDLED with 10 nm of MoO_x is more stable compared to that with 40 nm of MoO_x.

Finally, Figures 3.13 and 3.14 detail the characteristics of the final structures whose architecture is given in section 3.2.3. Figure 3.13a shows the I-V characteristics of the QDLEDs as the bias voltage is cycled through positive and negative values. The I-V stays stable after several ramping up and ramping down sequences but exhibits a hysteresis behavior that we attribute to the presence of TiO_2 in the stack (TiO_2 is a well-known memristive material [189]). Another aspect of stability was shown in Figure 3.13b. The EL images illustrate the stability of our QDLEDs over time for a bias voltage slightly higher than the turn-on voltage for EL. This stability is probably the most valuable feature of

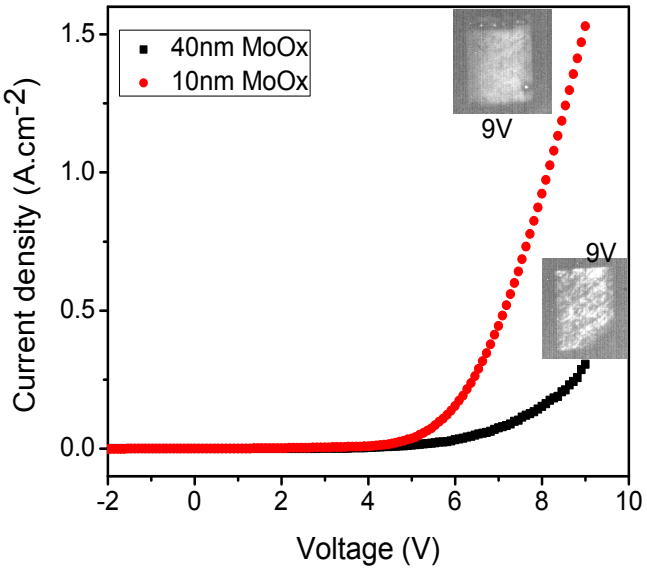

Figure 3.12: A comparison of the QDLED's performance with different thickness of the hole transport layer. The black I-V curve is for 10 nm thick of MoO_x, whereas the red is for 40 nm thick of MoO_x. Although their luminescence are quite equal, the thinner MoO_x is preferred because a better rectifying behavior might offer a lower turn-on voltage and more stability.

our QDLEDS because it guaranties that their properties do not change while we measure them. Figure 3.14a and 3.14b show the optical image and EL image of the junction at 10X, respectively, taken by a 10X objective. Figure 3.14c simultaneously displays the EL intensity and current density as a function of the applied voltage (to simplify the discussion, we have not plotted the hysteresis): it can be seen that the turn-on voltage occurs approximately at 6.5 V. In comparison, the state-of-the-art infrared QDLEDs in the literature so far operating with PbS CQDs have a turn-on voltage at approximately 2V [150]. We attribute the poorer performances of our devices by the fact that we work with commercial CQDs and uncontrolled atmosphere. However, we will see in the next chapter that it will not be an issue for the final goals of this thesis. The EL and PL spectra of our devices are plotted in Figure 3.14d and are well superimposed: both exhibit a peak around 1400 nm, as expected given the material (PbS) and size (5.3 nm) of the CQDs used in the device. It should be noted that the pronounced wiggles exhibited by the spectra in the 1350-1430 nm window are measurements artifacts due to water absorption

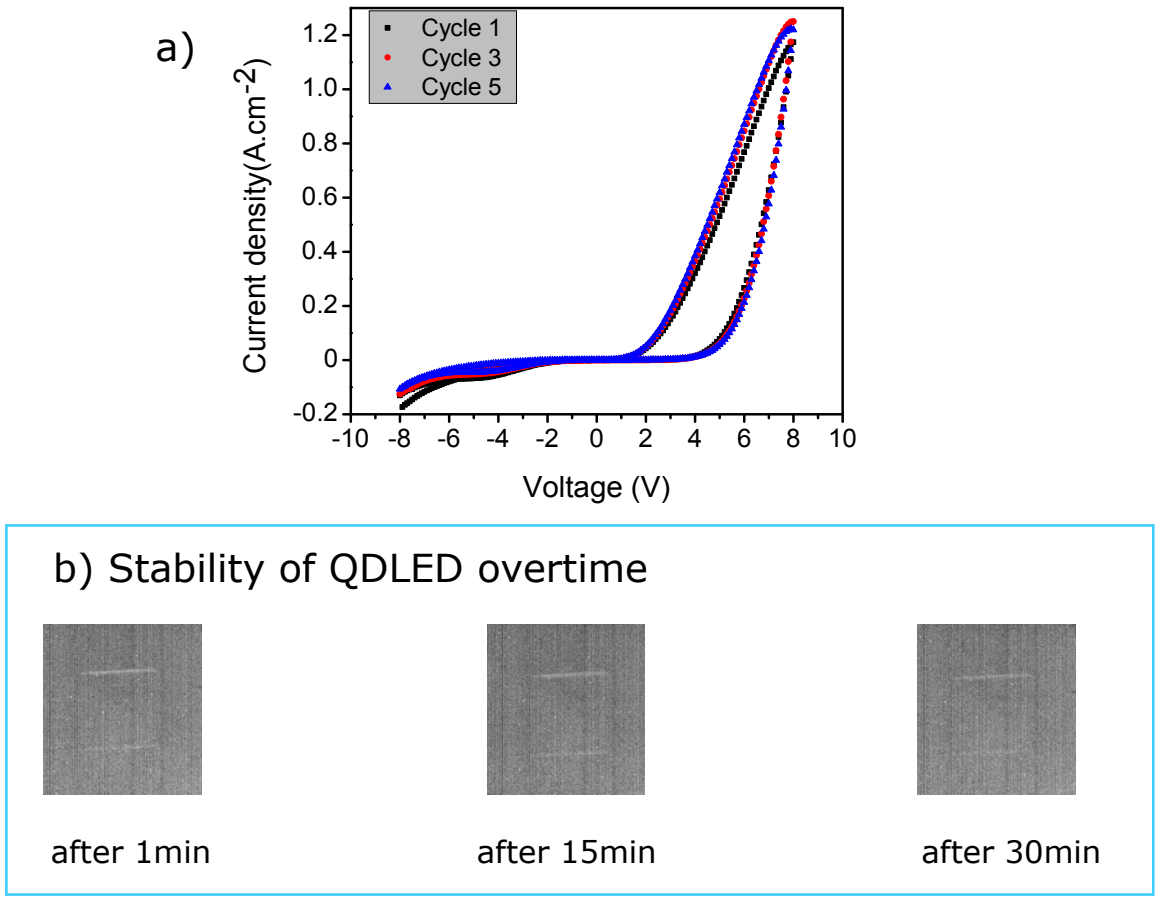

Figure 3.13: The complete hysteresis (-8V to 8V) of QDLED for the optimized configuration: Al 80 nm/anatase TiO_2 60 nm/QDs 15 nm/MoO_x10 nm/ITO 90 nm. The LED shows typical I-V curve with turn-on voltage around 6.0 V. b) The stability of LED at a voltage slightly higher than the turn-on voltage.

lines in the atmosphere.

In addition, we verified that all the characteristics of Figure 3.13 and 3.14 were stable over days if not weeks and also that they were reproducible if one repeats the fabrication process. Such stability and reproducibility are not straightforward results for two reasons. First, we have seen in chapter 2 that the same PbS CQDs are subject to photoactivation and a systematic blue-shift over time when they are embedded in a sol-gel matrix. Here, in contrast, the spectra shown in Fig. 3.14b do not change over time, indicating that the stack is chemically stable. Second, we process our samples under ambient atmosphere rather than in an inert glove-box environment as most other teams do. As a result, each layer of the stack is exposed to oxygen before being covered by the next one, resulting in

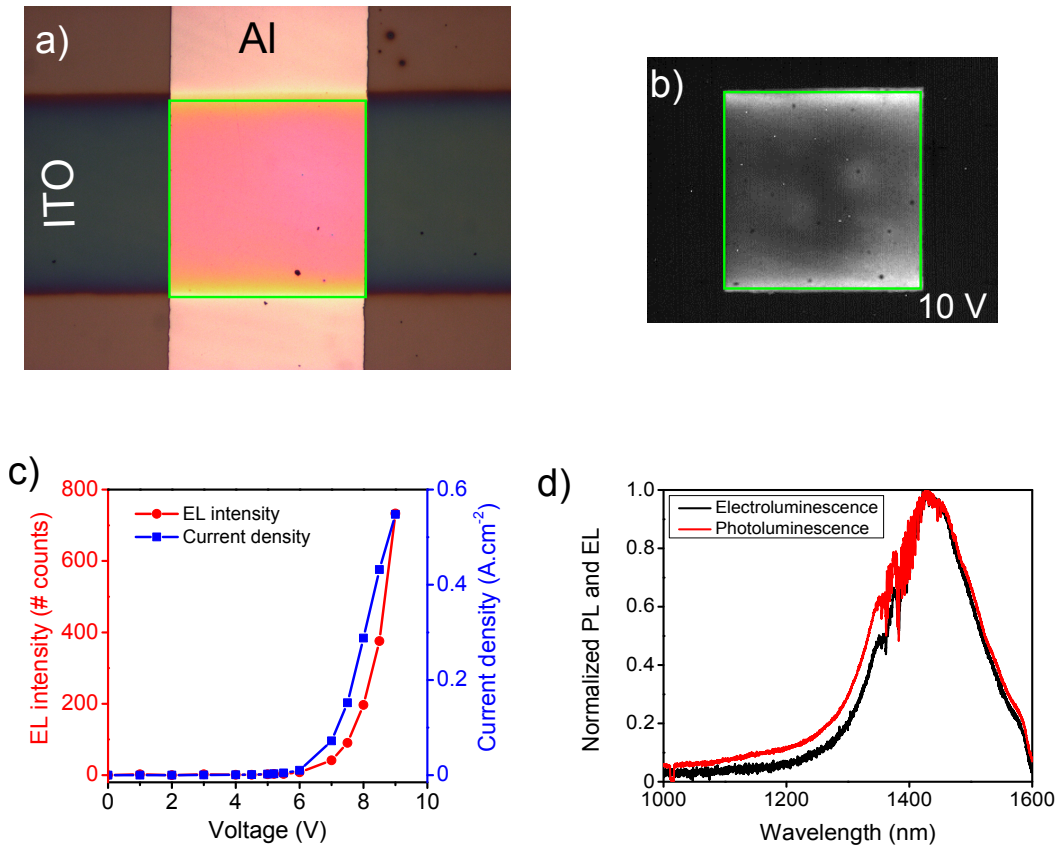

Figure 3.14: Summary of the basic characteristics of the optimized QDLED. a) The optical image of the device. b) A pretty uniform EL image of the optimized QDLED at 9V.c) The current density - voltage (J-V) and light-voltage (L-V) of the QDLED are traced simutaneously. d) The EL and PL spectra of the QDLED.

uncontrolled oxidation that could have led to high rate of unreliability from one sample to another. We attribute the high stability of our structures by the fact that most layers are inorganic oxides. Moreover, it is probable that the most sensitive layer, that is, the film of PbS CQDs, is passivated when exposed to the plasma that we use to cover it with sputtered MoO_x.

3.4 Conclusion and Remarks

In this chapter, I have learned and developed an expertise on QDLEDs that did not exist in my group. In addition, I have worked on a QDLED configuration emitting light through the top of the structure rather than by the substrate. I could not simply reproduce

a design already published in the literature because such top-emitting devices did not exist at the starting time of the project. The QDLEDs that we have fabricated are not state-of-the-art devices: for example, their EL turn-on voltage is around 6.5 V, which is approximately 3 times higher than the best infrared PbS-based QDLEDs reported in the literature. Nevertheless, our samples are stable and reproducible and therefore can serve as a reliable platform to develop new hybrid metamaterial/CQD optoelectronic devices. These developments are described in the next chapter: in particular, we will see that the introduction of a suitably-designed metamaterial within the architecture of our QDLEDs transform them in a radical manner.

Chapter 4

Metamaterial QDLEDs

In this chapter, we will show that metamaterials and CQD films can be hybridized to form a new type of active artificial medium for optoelectronic applications. Before describing these findings, it is worth noting that our goals were rather modest at first. Originally, our main target was merely to enhance the electroluminescence (EL) of the QDLEDs developed in chapter 3 by taking advantage of the plasmon resonances of the Au nanoparticle arrays studied in chapter 2. Similar efforts have been undertaken by other groups who have reported moderate EL enhancement by embedding plasmonic nanoaparticles within various QDLED architectures [190, 191]. In these studies, the plasmonic nanoparticles are colloids that are randomly distributed within one of the charge transport layers bounding the active CQD film. This approach makes it possible to boost the EL by a few times with no noticeable changes in the electrical and spectral properties of the QDLEDs. Moreover, it does not overly complicate the fabrication process since plasmonic colloids are compatible with the low-cost deposition techniques such as spin-coating that are typically used to fabricate QDLEDs.

In this thesis, in contrast, we have opted to work with lithographied nanoparticles rather than plasmonic colloids because we can precisely control the shape and respective positions of the different inclusions. In order to maximize the interactions with the CQD film, we have tried to place the Au nanoparticle arrays at various positions within the top-

emitting QDLEDs of chapter 3. Our initial attempts were inspired by two considerations: (i) the Au nanoparticles should not be too close from the bottom Al electrode which would otherwise perturb the plasmonic resonances and (ii) the Au nanoparticles should not be in direct contact with the CQD film in order to avoid non-radiative energy transfer (quenching). As it turns out, all our initial efforts resulted in a suppression of EL rather than the expected enhancement. These failures came as a surprise based on our experience in photoluminescence experiments developed in chapter 2: for systems that are pumped optically, the presence of metallic inclusions in the vicinity of emitters almost always lead to an enhancement of the luminescence. Clearly, this is not the case for electrically pumped systems, probably because the exact location of the plasmonic arrays strongly influences the efficiency of electrical injection.

Eventually, we realized that it was necessary to coat the CQD film directly on the metallic inclusions to observe a boost in the EL intensity. This is the configuration that is described in the present chapter. We will first discuss the fabrication and exact geometry of the devices and then explain that it does not only lead to a tremendous enhancement of the EL intensity, but also to radical changes in the operation principle of our QDLEDs. Finally, we will show that such plasmonic nanoparticle arrays coated with CQDs represent a true novel form of artificial active medium that makes it possible to weave complex light-emitting metasurfaces.

4.1 Fabrication of metamaterial QDLEDs

The fabrication procedure is exactly the same as the one described in chapter 3 for conventional QDLEDs, except that we insert an array of Au nanoparticles between the mesoporous TiO_2 layer and the film of PbS CQDs, as schematically shown on Figure 4.1b. As before, we work with samples fabricated on 1 x 1 cm^2 insulating substrates, with a total of 12 independent LEDs on each of them. For each sample, we insert a Au nanoparticle array in the architecture of 10 of the LEDs and leave the last 2 LEDs without metal

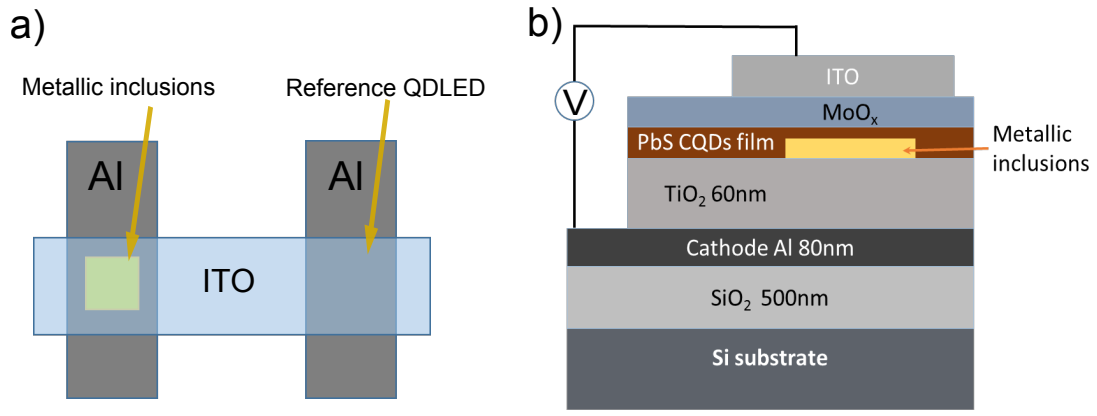

Figure 4.1: The design of metamaterial QDLED. a) Top view of the structure with Al cathode at the bottom, ITO anode on the top and the metamaterial will be integrated in between. b) A side view of the full designed architecture of metamaterial QDLED.

structuration so as to serve as reference devices. This arrangement is schematically shown in Figure 4.1a which depicts two independent LED devices, one with metallic inclusions and the other without. All the details of the fabrication can be found in Appendix D.

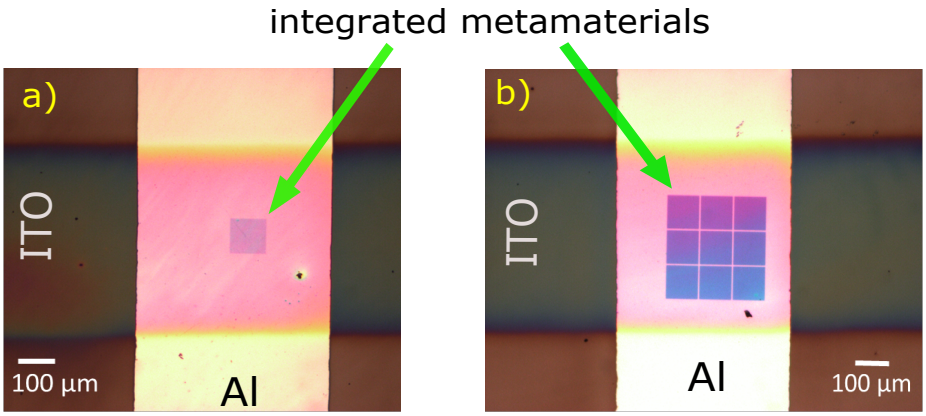

Figure 4.2: The optical view of fabricated samples as the metamaterials are integrated within the QDLED. a) The optical top view of a QDLED with a 100 x 100 μm^2 array of nanorods is integrated inside. b) The optical image of a metamaterial QDLED where a 3x3 matrix of 100 µm x 100µm arrays of nanoring is inserted inside.

The arrays of Au nanoparticles considered here are thinner than those studied in chapter 2 (the Au thickness is only 25 nm) but otherwise their fabrication follows the same combination of electron-beam lithography, Ti/Au deposition and lift-off. The only additional difficulty is that the Au nanostructures must be placed at the precise location of the LEDs, i.e. where the Al cathodes and ITO anodes overlap (Figures 4.1a and 4.2). To

this end, we have developed an alignment procedure whereby we use the scanning electron microscope of the lithography setup to manually locate the Al cathodes that are buried under the TiO_2 layer. We then define the local coordinates of each Au nanostructure array with respect to the cathode positions and with respect to the location of the ITO anodes that will be patterned at the end of the fabrication process.

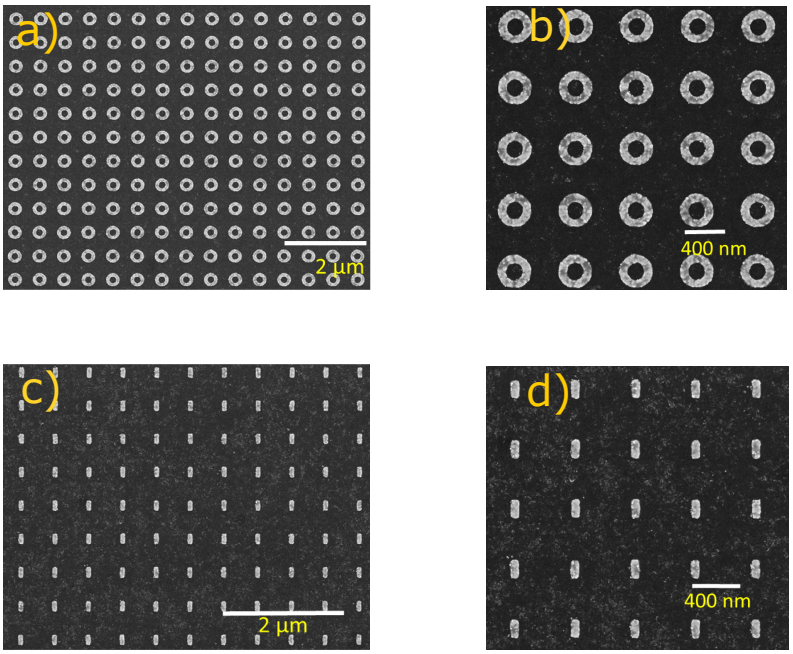

Figure 4.3: The nanostructures fabricated on a mesoporous thin film of anatase TiO_2. Two different shapes including a) nanoring structure, b) magnified nanorings, and c) array of nanorod, d) a magnified view of the nanorod array.

Figure 4.3 shows SEM micrographs of representative nanoparticle arrays. We have worked with nanorings as in chapter 2 as well as with nanorods that will be used for their polarization properties. Besides chosen for polarization, the nanorods exhibiting the resonance closely at the emissive wavelength of the quantum dots is another reason that the structure is selected, see Appendix E for further discussions. These images show the good quality of our structures, a result all the more remarkable that they are not fabricated on a smooth, conventional substrate, but on a mesoporous layer of spin-coated TiO_2 nanoparticles (see chapter 3 and appendix D).

To gain quantitative insight on the surface roughness of the TiO_2 layer and why it

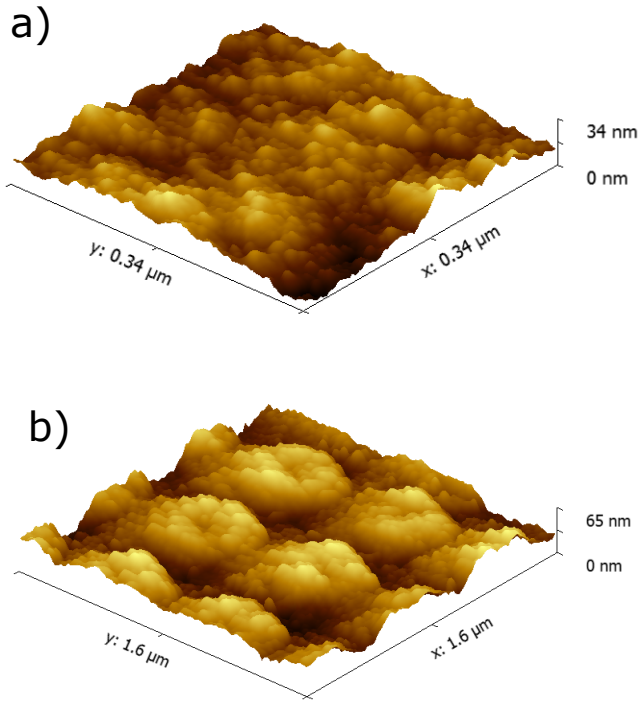

Figure 4.4: AFM characterization of morphology of nanorings on TiO_2 thin film. (a) AFM image of the surface of the anatase TiO_2 thin film. Mean (arbitrary) altitude: 17 nm and RMS roughness = 4.6 nm. (b) AFM image of the surface TiO_2 with gold nanorings patterned on top of the film. It is noted that the center of nanorings are not well resolved due to the cumbersome size of AFM tip.

can serve as an efficient support for high-quality lithographied metallic patterns, we have characterized our samples with atomic force microscopy (AFM). Figure 4.4a shows that the RMS roughness of the bare TiO_2 surface is approximately 4.6 nm—a value consistent with the fact that the diameter of the particles forming the TiO_2 mesoporous film is on the order of 5 nm. When coated by the 25 nm thick Au nanostructures, Figure 4.4b, the size of the surface inhomogeneities increases and become dominated by the metallic grains, explaining why the resulting patterns are very similar to those obtained on the smooth glass substrates of chapter 2.

As explained in the introduction and illustrated in Figure 4.1, all the effects that will

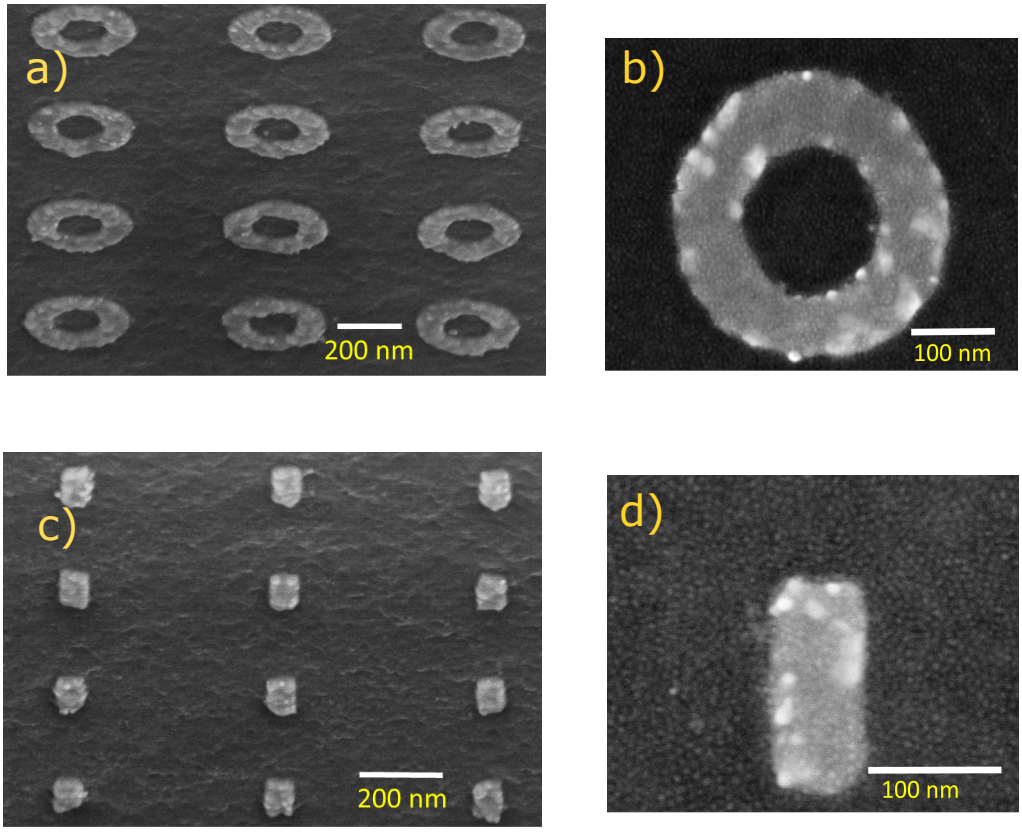

Figure 4.5: The SEM view of nanoparticle arrays coated by a PbS CQDs film. a) A titled view of PbS CQDs coated on top of nanorings. b) A magnified view of PbS CQDs coating a nanoring seen at normal incidence. c) A titled view of PbS CQDs films coated on arrays of nanorods; d) A magnified view of PbS CQDs distributed with respect to a nanorod at normal incidence.

be described below result from the fact that the PbS CQDs are directly coated on the plasmonic nanoparticle arrays. Therefore, it is important to understand how the CQDs self-organize when they are spin-coated on the sample. We have used the same spin-coating parameters as those utilized to fabricate our conventional QDLEDs in chapter 3: namely, we spincast a 26 mg/mL solution of PbS CQDs in toluene at 2000 rpm onto the sample and perform a soft-bake at 150 ^{o}C in air, which results in a 15 nm thick CQD film. Figures 4.5a and 4.5c are SEM micrographs of the coating of PbS CQDs on top of nanorings and nanorods at a tilted angle and a magnification of 70kX. At this magnification, it is not possible to distinguish the dots and we clearly see the Au nanostructures due to the small thickness of the CQD film. To have a more quantitative

idea of the local organization of the PbS dots, we have imaged the structures at normal incidence and 250 kX (Figures 4.5b and 4.5d). One can see that the CQDs form a uniform coating both on the Au inclusions and on the underlying TiO_2 substrate.

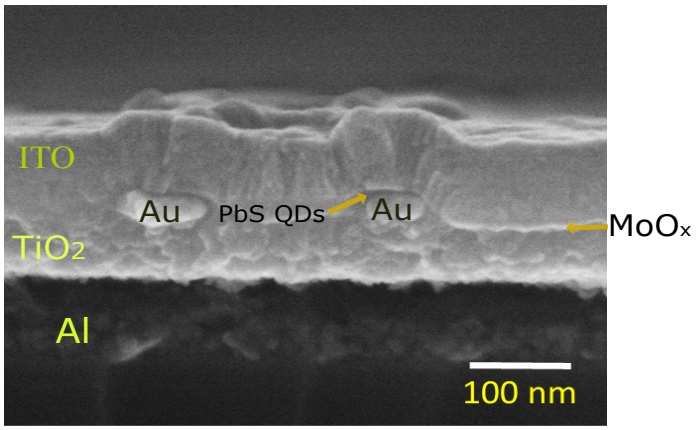

Figure 4.6: The cross section view of a completed metamaterial QDLED. The sample was prepared on Si substrate with approximately 80 nm of Al stripe, followed by 60 nm of TiO_2, 25 nm thick of lithographed Au nanorings, 15 nm ± 4 nm of PbS QDs, 10 nm of MoO_x and 80 nm thick of sputtered ITO.

To summarize the fabrication procedure, we show in Figure 4.6 a cross-section of a finished device. This cross-section has been made in the middle of a Au nanoring, so we see two gold regions corresponding to each side of the ring. Most of the layers composing the stack are clearly visible, to the exception of the film of PbS CQDs and the MoO_x HTL which are too thin to be clearly resolved and also probably compressed by the cut. Interestingly, the layers coated on top of the Au nanoring are conformed above it, but the resulting internal stress is too weak to delaminate the sample.

4.2 Metamaterial QDLEDs: qualitative observations

In this section, we characterize the behavior of our metamaterial QDLEDs with the same EL and PL setup that we used in the previous chapter. We first consider a QDLED with a gold nanoring array with period 450 nm, inner ring radius of 30 nm and outer ring

radius of 88 nm in its architecture, as displayed in the image inset in Figure 4.7a. These geometrical parameters are such that the Au inclusions have a filling factor of 11 %. The surface occupied by this array is limited to 200 by 200 µm, so it is smaller than the overlap between the Al and ITO electrodes (we remind the readers that the electrodes are 500 µm wide, so that each LED has a total area of 500 µm by 500 µm). This particularity can be seen on the optical image of Figure 4.7a where the ring array appears as a dashed purple square within the larger orange-shaded LED.

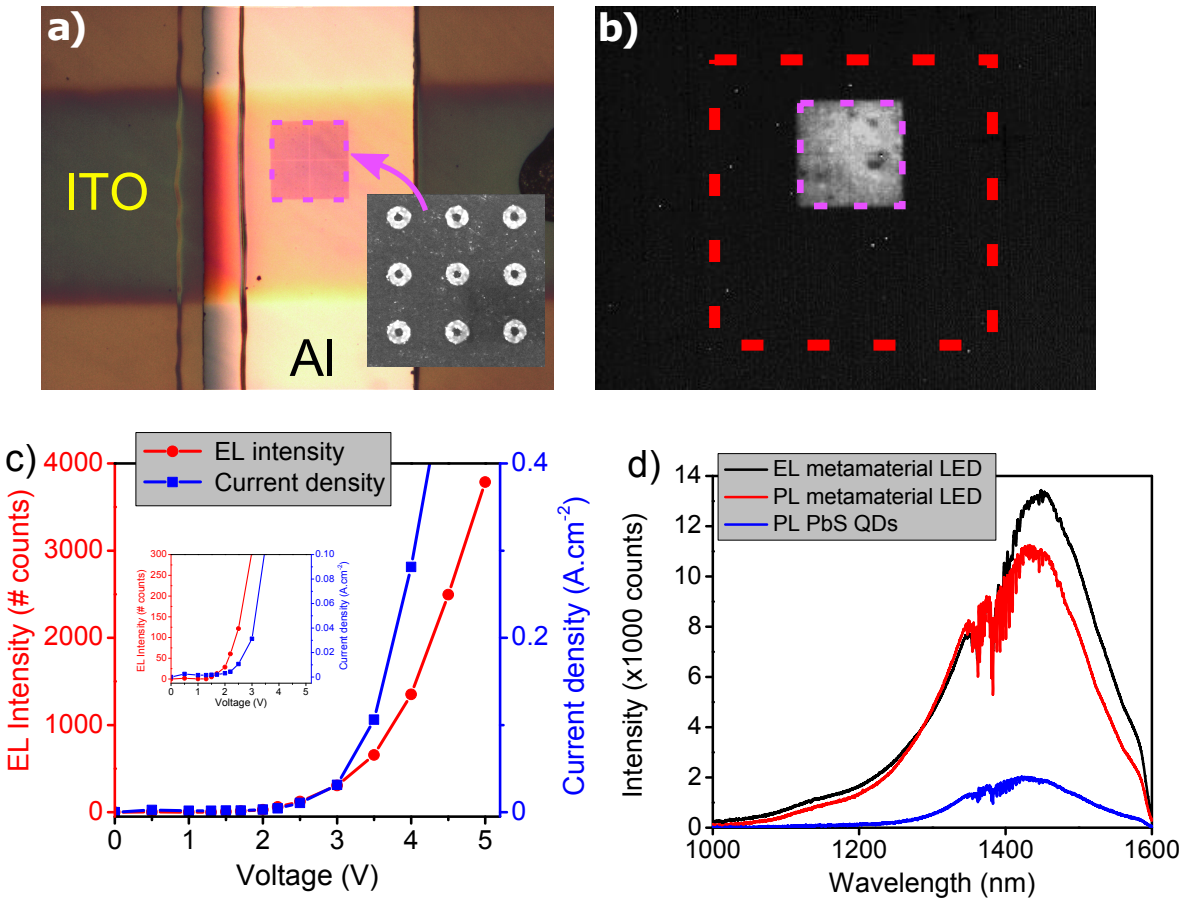

Figure 4.7: Images of metamaterial QDLED and its characteristics. a) Optical image of the metamaterial QDLED. The 200 x 200 µm^2 of Au nanorings (inner, outer radii and thickness are 30, 88, and 25 nm, respectively) integrated within the overlapping area of ITO and Al electrodes. b) The infrared electroluminescence image from the metamaterial QDLED. c) The L-V and J-V of the metamaterial QDLED taken simultaneously. d) PL and EL spectra of PbS QDs and of the metamaterial QDLED.

The emission characteristics of such a device are very different from that of the conventional QDLEDs studied in chapter 3: when subjected to a positive bias voltage, light

emission occurs only above the region occupied by the ring array (Figure 4.7b) rather than over the whole LED area defined by the overlap of the Al and ITO electrodes. To gain more quantitative insight, we plot in Figure 4.7c the electroluminescence intensity (L-V) and the current density(J-V) of the devices as a function of the applied voltage (here the current density is calculated by normalizing the current to the area occupied by the metallic arrays instead of the whole junction). Figure 4.7c shows a dramatic change of the L-V and J-V characteristics compared to those of the conventional QDLEDs of chapter 3 (cf. Figure 3.14). In particular, the EL turn-on voltage, which used to be approximately 6 V for our conventional LEDs, is reduced to 1.5 V as shown better in the inset of Figure 4.7c. This, to our knowledge, is the lowest turn-on voltage ever reported for PbS-based QLEDs operating under ambient air and is in line with the most state-of-the-art QDLEDs operating under the N_2 environment [150, 192]. It is accompanied by an L-V curve that is much steeper than in the case of the conventional LED so that, the electroluminescence intensity, at any given voltage, is enhanced by several orders of magnitude compared to our conventional QDLEDs.

Figure 4.7d shows the EL and PL spectra of the metamaterial QDLED as well as the PL spectrum outside the metallic patterns. The PL above the Au inclusions shows a significant enhancement, demonstrating that the CQDs are not quenched by the metal, probably because of their long ligand chains (2 nm). It is also worth noting that the spectral signature is similar to that of the PbS CQDs outside the metallic array but we will see later with other structures that it is generally not the case. Last, one can notice that the 1350-1450 nm spectral window is again perturbed by the absorption lines of water present in the atmosphere, just as in chapter 3.

In a next step, we show that these properties are independent from the total size of the nanoparticle arrays. Figure 4.8 shows the light emission from metamaterial QDLEDs with the same geometrical parameters of the nanorings used in Figure 4.7, except that the total size of the plasmonic array varies from 100x100 μm^2 to 400x400 μm^2 with an increment of 100x100 μm^2. In all cases, the bias voltage is 4V and one can see that the light

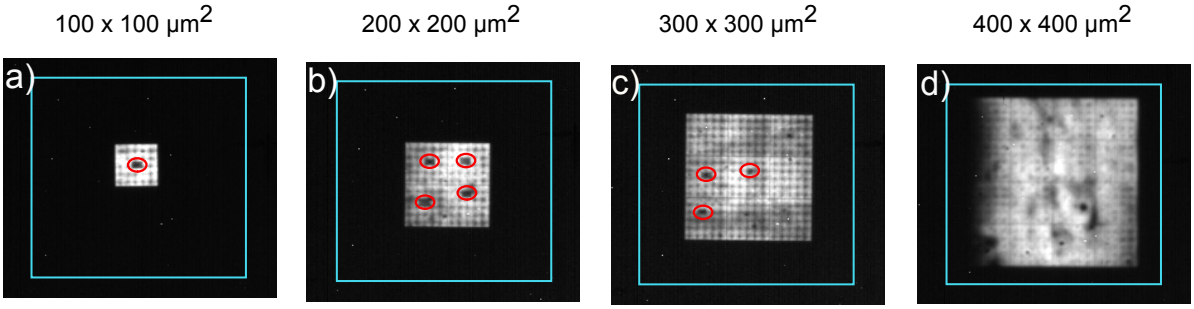

Figure 4.8: Electroluminescence with small nanoring QDLED. a), b), c), and d) are the electroluminescence images of the small nanoring metamaterial LEDs with areas ranging from 100x100 to 400x400 μm^2, respectively. All the images were recorded at the same applied voltage 4V. Note that small red ellipses marked in a), b) and c) corresponding to the dead zone, no light appearing, due to the carbon contamination while exposed to high energy electron-beam of the SEM imaging.

intensity is constant from one structure to another. Before providing more quantitative data, we note in passing that all QDLEDs have small dark inhomogeneities (circled in red on the figure): these darker spots correspond to the zones that were observed by SEM microscopy prior to CQD deposition and that have thus been exposed to a slight carbon contamination [193]. These observations illustrate the high sensitivity of the phenomena that take place within the structures.

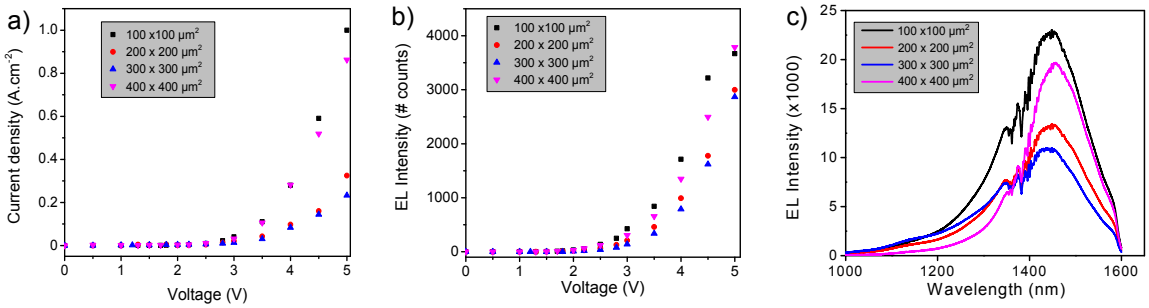

Figure 4.9: The J-V (a) and L-V (b) curves and EL spectra (c) of metamaterial QDLEDs as the ring array area is varied from 100x100 μm^2 to 400x400 μm^2.

Figure 4.9a shows the current density-voltage characteristics of the same series of metamaterial LEDs. All J-V curves are very similar, further demonstrating that the characteristics of the devices are largely independent of the size of the nanoparticle array. It might be argued that the curves seem to be regrouped in two sub-groups but

we attribute this effect to experimental errors because we have noticed that the measured current density depends on the exact location of the electrical probe on the ITO electrode—because our ITO has a significant resistivity, the current density falls if the probe is too far away from the LED junction. As for the EL intensity-voltage (L-V) curve, Figure 4.9b reveals that it is also very constant from one structure to the other, in good agreement with the images of Figure 4.8. In addition, we note that the L-V curves are strongly correlated with their current density-voltage (J-V) behavior since the current flowing through the LEDs begin to rise at about the same biases as the turn-on voltages where light emission occurs. To complete this qualitative description, Figure 4.9c plots the spectra of the four metamaterial QDLEDs. Similarly to the J-V curves of figure 4.9a, there are a few variations among the different spectra but no monotonous trend as the size of the nanoparticle array increases. Again, we attribute these small changes to experimental uncertainties.

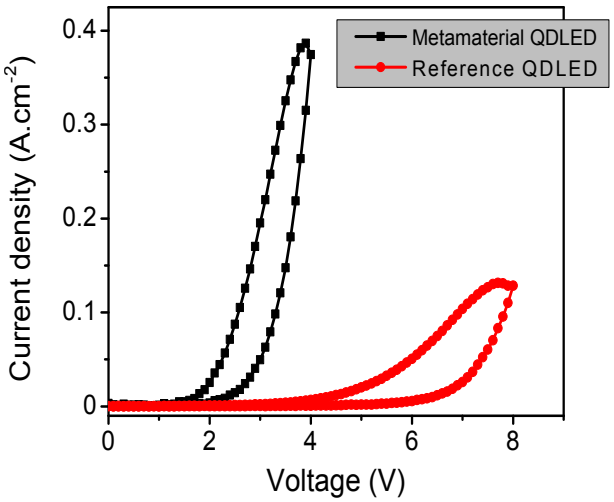

Figure 4.10: The hysteresis comparison of metamaterial and reference QDLED. The hysteresis of the metamaterial QDLED is plotted from 400x400 μm^2 of the nanorings.

Finally, we emphasize here that, as was the case for our conventional QDLEDs in chapter 3, both the J-V and L-V curves exhibit an hysteresis due to the presence of TiO_2 in the architecture of our devices—a material known for his memristive properties [189]. This effect is illustrated in Figure 4.10 that shows the full J-V curve of the sample with the ring array having the largest area (400x400 μm^2) along the J-V characteristic of a

reference QDLED without metal structuration.

We next repeat these experiments for a new series of metamaterial QDLEDs in which the Au rings and their period is larger (inner radius 73 nm, outer radius 157 nm and period 600 nm, corresponding to a higher filling factor of 17%). The fabrication of this set of devices was a little less successful as the previous one, resulting in noticeable defects within the structures. Figure 4.11 illustrates this point by showing the light emission as the area of the nanoring array is increased from 100x100 μm^2 to 400x400 μm^2. Nevertheless, each structure features good areas that are large enough to extract meaningful data from these samples.

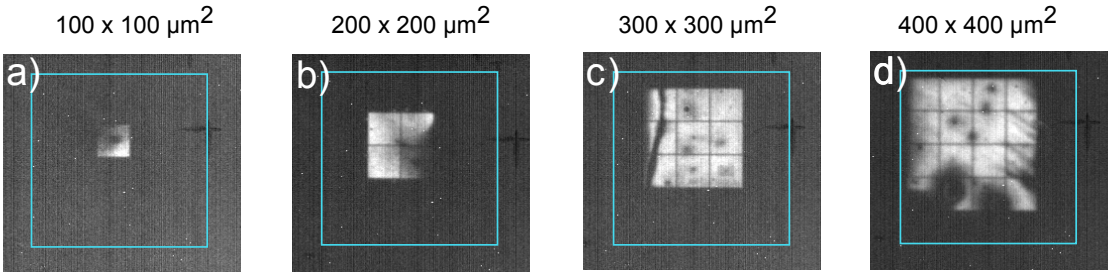

Figure 4.11: Electroluminescence with arrays made of larger nanorings (big rings: inner and outer radii and period are 73, 157 and 600 nm, respectively). a)-d) displays the electroluminescence of metamaterial QDLEDs with nanoring arrays ranging from 100x100 μm^2 to 400x400 μm^2, respectively. The electroluminescence images are recorded at 4 V, the cyan square lines denote the boundary of the full QDLED.

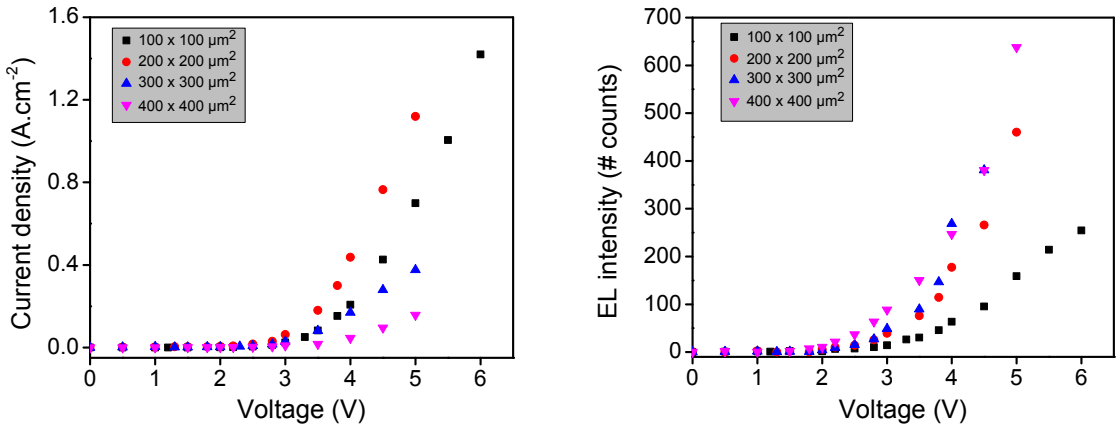

Figure 4.12: The J-V (a) and L-V (b) curves of the corresponding metamaterial QDLEDs of Figure 4.11.

Figure 4.12 shows that with this geometry also, the J-V and L-V curves are largely

independent of the size of the nanoring array. However, the threshold voltage is higher than the structures with smaller rings studied previously (around 2V instead of 1.5 V, which is still much lower than the threshold voltage of the conventional QDLEDs of chapter 3). Moreover, the spectral signature of this series of QDLEDs is also different, as shown with the EL and PL spectra of Figure 4.13 where a pronounced shoulder can be observed at a wavelength of 1270 nm in addition to the main peak located at 1430 nm. As a corollary, the EL and PL spectra of the metamaterial QDLEDs are significantly different from the spectrum of the PbS CQDs located far from the ring array (plotted in in black on Figure 4.13b).

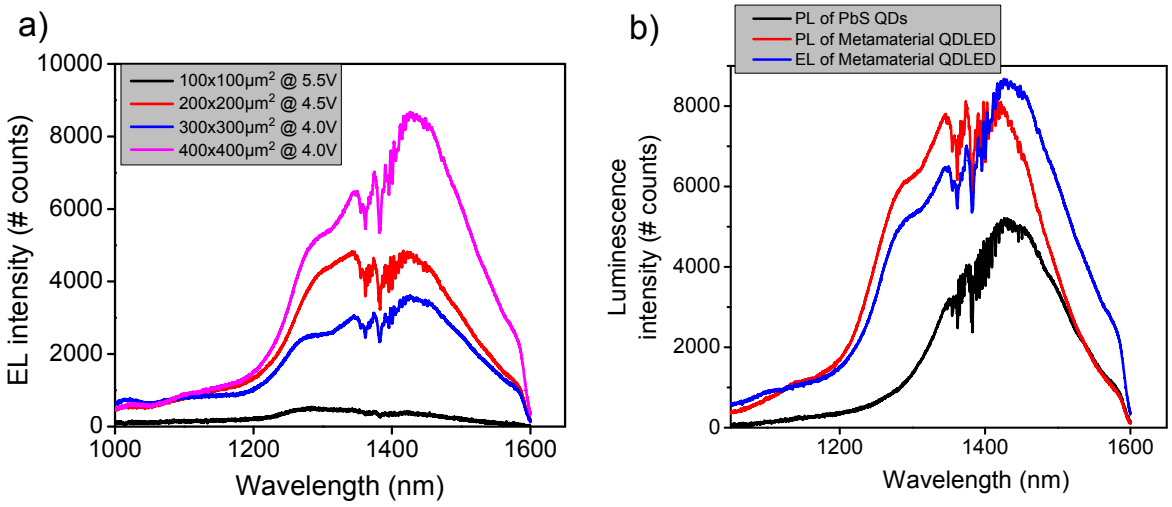

Figure 4.13: The luminescence spectra of metamaterial QDLEDs and a pure QDLED. a) The EL spectra of metamaterial QDLEDs as the ring array area is varied. b) A spectral comparison of pure QDLED and metamaterial QDLED.

To conclude this descriptive section, we have presented the characteristics of two series of metamaterial QDLEDs and observed in all cases that light was only emitted above the Au nanoparticle arrays and that the geometry of the latter (but not their total area) had a strong influence on the optical and electrical characteristics of the devices. The next section will clarify this behavior with more systematic comparisons.

4.3 Metamaterial QDLEDs: mechanism hypothesis

To gain insight into the metamaterial QDLED operation, we compare in a quantitative way the behavior of the different structures that we have considered so far (that is, the metamaterial QDLED with small rings and filling factor 11%, the metamaterial QDLED with large rings and filling factor 17% and a reference QDLED without metal nanostructure). Figure 4.14 shows the L-V and J-V curves of the three types of devices, clearly

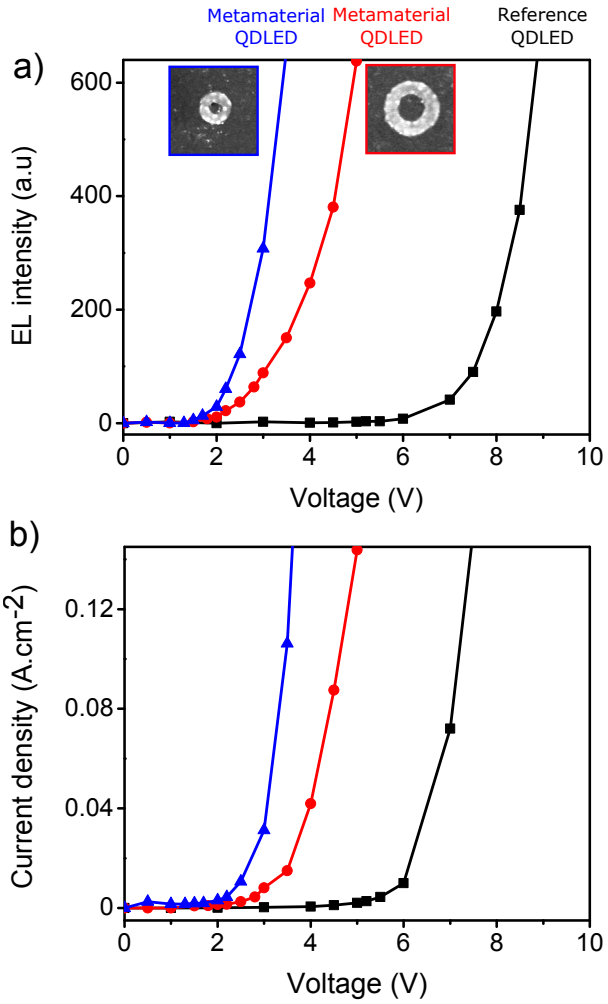

Figure 4.14: Comparing L-V and J-V of QDLED in the presence and absence of the metamaterials. a) The metamaterial QDLEDs shows a pronounced enhancement of EL intensity compared to the standard QDLED. However, the order of EL enhancement depends on the inner geometry used. b) The current densities of the corresponding devices exhibit a similar trend in which much higher current passes through the devices with metamaterials and the increase of the current is also dependent of the geometry used within their devices. The same color code is used for both graphs.

illustrating the benefit of inserting metallic nanostructures in the design of the QDLED.

4.3.1 Role of plasmonic resonances

Figure 4.15a superimposes the EL spectra of the different devices. The reference QDLED is characterized by a broad spectrum centered around 1450 nm (green curve), the EL spectrum of the metamaterial LED with small rings is slightly shifted toward longer wavelengths (blue curve), while the metamaterial LED with larger rings exhibits much more complex features such as the apparition of three new peaks at smaller wavelengths (red curve).

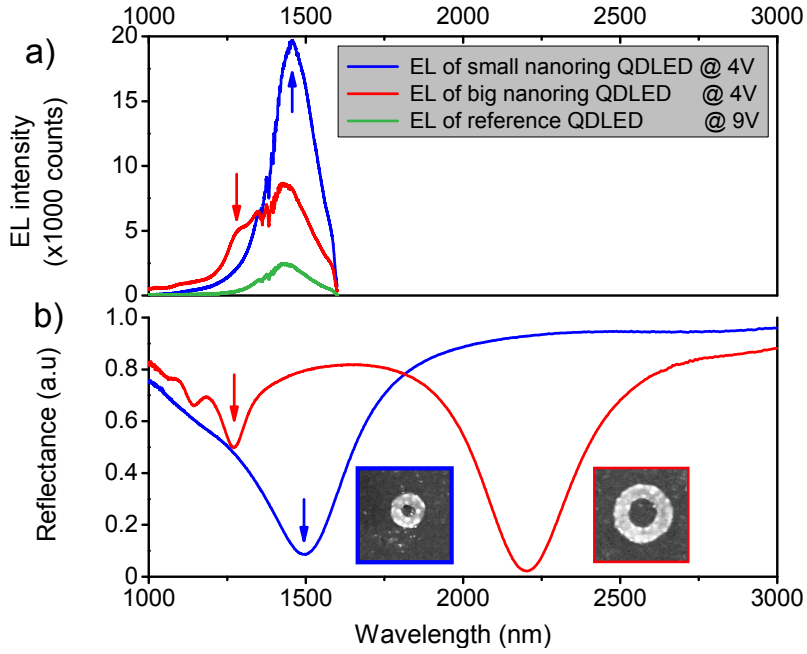

Figure 4.15: Comparison of the EL spectra with the reflectance signals of the metamaterial QDLED. a) The EL spectra of small and large nanorings. b) The reflectance spectra of the corresponding structures. The spectra of both panels have the same color codes with the blue and red curves corresponding to small and big nanorings, respectively. A green curve is the EL of the reference QDLED.

The strong dependence of the EL spectra on the ring geometry indicates that the metamaterial LEDs operate through the excitation of localized surface plasmons. To confirm this hypothesis, we have measured the reflectance spectra of the structures by Fourier Transform Infrared (FTIR) spectroscopy and found the same resonances, as shown

in Figure 4.15b. In these experiments, the structures are illuminated from the ITO side. Due to the presence of the Al electrodes on the bottom side, most of the incoming light is either reflected back toward the objective and the FTIR spectrometer or, if a surface plasmon resonance is excited, scattered and absorbed, producing a distinctive minimum in the reflection spectrum, see Appendix E for further discussion of the decreased reflectance. The experimental curves of Figure 4.15b are in excellent agreement with the EL spectra of Figure 4.15a. The metamaterial LED with small rings exhibits a broad minimum at 1500 nm, which corresponds to the fundamental plasmon mode of the nanorings. In contrast, the fundamental resonance of the structure with larger rings and period is shifted outside the spectral range of emission of the LED but one can see that three higher-order plasmon resonances are excited at the same wavelengths as the EL maxima of Figure 4.15a. Such spectra with higher order modes can be reproduced with numerical simulations, as the group has shown for example in Ref. [59] . These features explain why the metamaterial LED with small rings is the brightest device (Figure 4.15a): the surface plasmon resonances, occurring at 1500 nm, are almost exactly matched with the intrinsic electroluminescence of the PbS CQDs (black curve of Figure 4.15a). In contrast, the plasmonic boost provided by the larger rings of the second metamaterial LED occur at wavelengths where the PbS CQDs emit less light, so even if the relative enhancement is similar, the absolute intensity is smaller.

It is remarked that the plasmonic resonances can be directly seen in the electroluminescence spectra (i.e. without significant shift or change in the linewidth of the peaks) is not a trivial result. As discussed in chapter 2 for PbS CQDs embedded in a dielectric host matrix, it may well indicate that the dots emit through surface states in addition to their intrinsic excitonic transitions. Further studies are needed to clarify this point. In any case, our measurements prove at the very least that the Purcell effect is a major cause of the enhanced performances of our metamaterial QDLEDs. The enhancement is so strong that charge injection, and thus conductivity, are also grealy boosted. In the next section, we discuss the possibility that other mechanisms also contribute to the device behavior.

4.3.2 Influence of the metallic nanostructures on electrical injection

One legitimate question is whether the enhanced properties are not simply due to the fact that the gold inclusions favor electrical injection in the QLED. According to previous studies, the contact between PbS CQDs and a gold surface is ohmic, or, said otherwise, no depletion region is created that would hamper the injection of electrons within the dots [194]. To investigate this possibility, we reproduce in Figure 4.16a the J-V curves of Figure 4.14 along with the J-V characteristic of a device where the Au nanoparticle array has been replaced with a continuous gold film (green curve), the optical image is shown in Figure 4.17a). Such a structure does not support any surface plasmon resonance and instead acts as a metallic mirror, as can be seen from its reflectance spectrum plotted in Figure 4.16b. Its J-V characteristic has an even better conductivity than the metamaterial LEDs, indicating that the presence of gold in the stack does indeed induce a path of least resistance where the current preferentially flows.

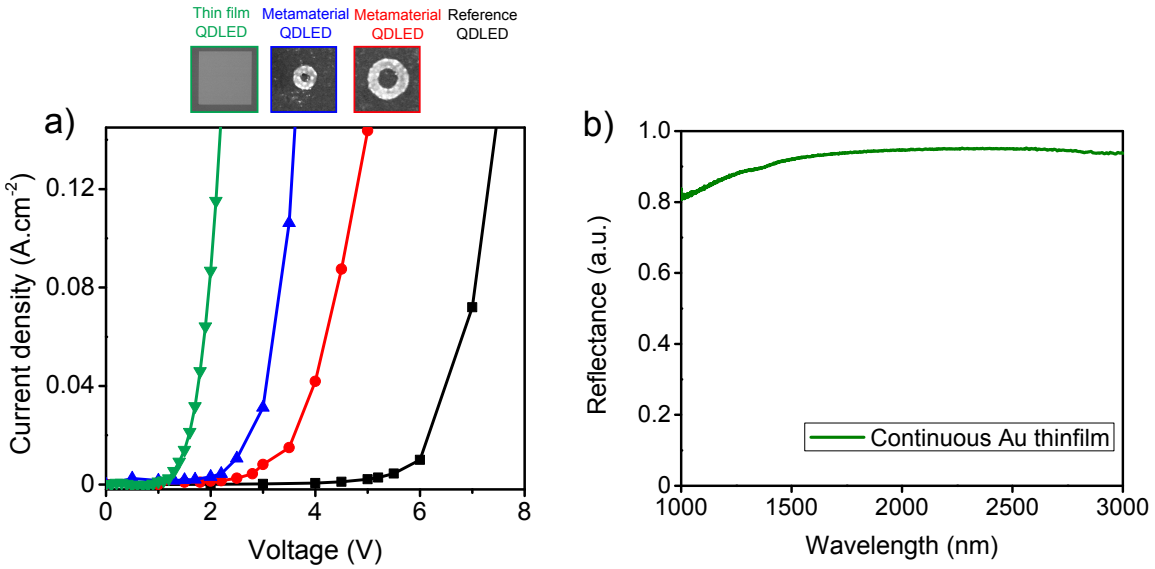

Figure 4.16: The electrical characteristic of a continuous Au thin film (300 µm x 300 µm intergrated inside QDLED instead of a textured nano-array. a) The J-V curve of the QDLED with the continuous thin film is plotted with those of the reference and metamaterial QDLEDs. b) The reflectance of the QDLED with the continuous thin film.

However, this mechanism alone does not explain the operation of the metamaterial

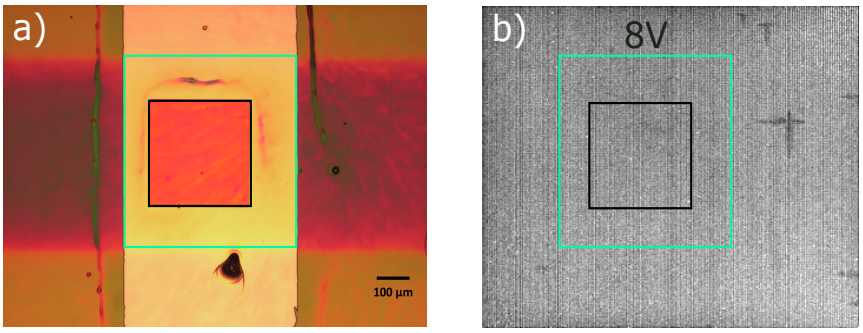

Figure 4.17: The electroluminescence characterization of the continuous Au thin film (300µm x 300µm QDLED. a) The optical image of a QDLED with a continuous gold film integrated inside. b) No light has been observed with thin film QDLED at 8V and higher voltage. The cyan and black square lines denote the QDLED boundary and the continuous thin film area, respectively.

LEDs because the device with the continuous metal film does not emit light at all, even at high voltages, as demonstrated in Figure 4.17b. In addition, the metamaterial LED with the highest brightness and conductivity (small rings and period 450 nm, blue curves of Figures 4.15a and 4.16a) is the one where the fraction occupied by the gold patterns is the smallest (11% of the total ring array, as opposed to 17% for the metamaterial LED with larger rings and larger period characterized in the same panels).

4.3.3 Influence of the separation between the Au nanoparticle arrays and the CQD film

Here we study three devices proving that the CQD film must be coated directly onto the Au nanoparticle arrays. Figure 4.18 shows the carton depiction of three metamaterial LEDs in which a thin layer (5 nm) of sputtered TiO_x is inserted at different positions, corresponding to devices A, B, and C.

In device A, the TiO_x layer is placed between the Au nanostructures and the CQD film. Device B is the standard metamaterial QDLED without the presence of the 5 nm thick sputtered TiO_x layer. As for the last diode, the thin layer of TiO_x is inserted between the CQD film and MoO_x. The detailed description of the layers within each device is

provided below:

Device A: Glass substrate/Al stripe 80 nm/TiO_2 60 nm/Au nanostructure arrays 25 nm/TiO_x 5nm/QDs film 15 nm/MoO_x 10nm/ITO 80nm.

Device B: Glass substrate/Al stripe 80 nm/TiO_2 60 nm/Au nanostructure arrays 25 nm/QDs film 15 nm/MoO_x 10nm/ITO 80nm.

Device C: Glass substrate/Al stripe 80 nm/TiO_2 60 nm/Au nanostructure arrays 25 nm/QDs film 15 nm/TiO_x 5nm/MoO_x 10nm/ITO 80nm.

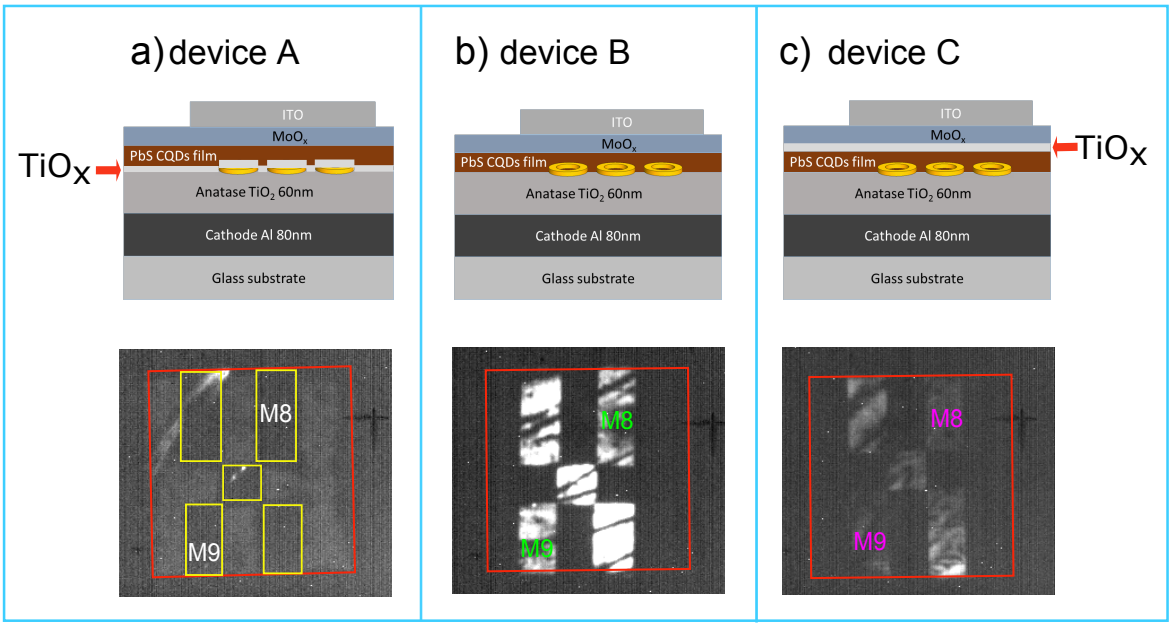

Figure 4.18: Behavior of metamaterial QDLEDs when a thin layer of TiO_x is inserted at different positions in the vertical stack. a) EL image of device A at 10.5V. b) EL image of device B at 5V. c) EL image of device C at 10.5V. Red squares line denotes the QDLED boundary.

Figure 4.18 shows the electroluminescence of the three devices. We have deliberately patterned each LED with several Au nanoparticle arrays in order to demonstrate that our results do not depend on the exact geometry of the Au nanostructures. Each device A, B and C have two nanoring arrays in common, denoted M8 and M9 on Figure 4.18. We will focus on these particular arrays to make quantitative comparisons between the three samples.

Figure 4.18a shows that the luminescence is extremely dim for device A. Although it

may not be visible on the printed version of this thesis, a closer inspection of this image reveals that EL actually occurs everywhere, *except at the location of the Au nanoparticle arrays.* This behavior is in sharp contrast with the metamaterial QLEDs in which the CQDs are directly coated on the Au nanostructures, see previous figures and also the behavior of device B in Figure 4.18b. This result clearly shows the importance of coating the dots directly on the nanostructures to benefit from the Purcell effect and the resulting plasmonic boost.

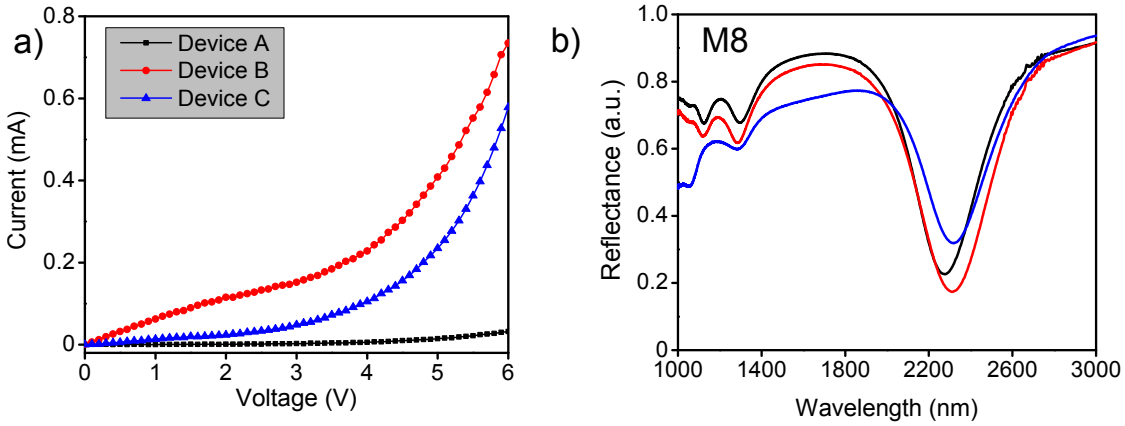

Figure 4.19: Electrical and optical measurements of devices A, B, and C. a) the I-V curves of these devices. b) The reflectance spectra of Motif 8 (arrays of nanorings). The same color code is used for both graphs.

It may be argued that the absence of light above the Au nanostructures of device A results from a degraded carrier injection because of the presence of the thin TiO_x layer. While we cannot completely discard this possibility, the results of device C, shown in Figure 4.18c, suggest that it is not the case. In device C, the thin TiO_x layer is placed on top of the CQDs, which is probably the worst configuration for electrical injection since it acts as a barrier for the holes coming from the MoO_x hole transfer layer. Yet, Figure 4.18c reveal that light is only emitted above the structures, just as for device B, even if the EL is understandably dimmer.

Figure 4.19a plots the I-V curves of these devices. Here also, we see that the EL of Figure 4.18 is strongly correlated to the current flows. Specifically, the absence of electroluminescence on top of the nanoparticle arrays in device A is accompanied by a

very low current flowing through the device. In contrast, the current flowing through device B is the highest of all three samples while the current flowing through device C lies in between these two extremes.

As a final control experiment, Figure 4.19b confirms the excitation of the same plasmonic resonances in all three devices. For the clarity, we only plot the reflectance of one nanoring structure (M8) of these devices though the reflectance curves for M9 are similar profiles but sift slightly at different wavelengths.

4.3.4 Role of the CQD film

All the metamaterial LEDs discussed so far have been made with a 15 nm thick layer of quantum dots, corresponding to 1-2 monolayers of PbS nanocrystals. The importance of the hybrid has been demonstrated in the previous section, and in this section we focus on studying the impact of the quantum dot film on the hybrid. To this, we fabricated a series of samples with devices with and without CQD film. The devices are numbered from 1-4 and their architectures are described as following:

Device 1: Glass substrate/ Al stripes 80 nm/Anatase TiO_2 60nm/ MoO_x 10nm/ ITO 80nm.

Device 2: Glass substrate/ Al stripes 80 nm/Anatase TiO_2 60nm/PbS QDs 15nm/ MoO_x 10nm/ ITO 80nm.

Device 3: Glass substrate/ Al stripes 80 nm/Anatase TiO_2 60nm/ Au nanostructure arrays 25 nm/ MoO_x 10nm/ ITO 80nm.

Device 4: Glass substrate/ Al stripes 80 nm/Anatase TiO_2 60nm/ Au nanostructure arrays 25 nm/ PbS QDs 15nm/ MoO_x 10nm/ ITO 80nm.

The stacked configuration of each device and their electroluminescence responses are depicted and displayed in Figure 4.20. Device 1 is the device where both the Au nanoparticle arrays and the CQD film are absent. Device 2 is the reference QDLED as routinely discussed in chapter 3, whereas device 3 is the control device in the presence of metallic nanoparticles but absence of quantum dots film. The last device, Device 4, is the meta-

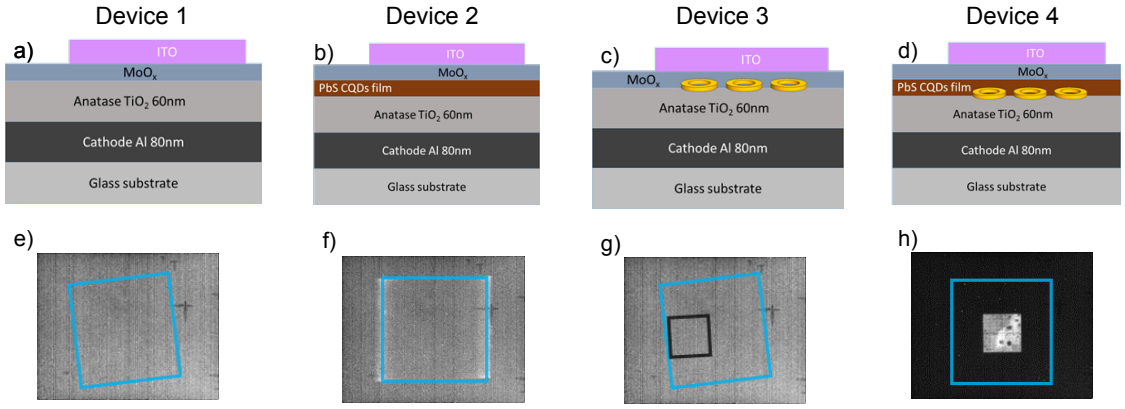

Figure 4.20: Stacked layer of control experiment in the absence and presence of the QD film. a) Device 1 without film of PbS QDs and Au nanoparticles, b) Device 2 with the presence of Au nanoparticles but without PbS QDs film, c) Device 3 with the presence of PbS QDs film but without the Au nanoparticles, and d) Device 4 (Metamaterial LEDs) with the hybridization of CQDs film and Au nanoparticles. e) - h) are the electroluminescent images of the corresponding diodes in a forward bias. Note that the cyan open squares are the overlapping between Al and ITO stripes. A small black square in g) is the area of the similar nanoring array used in h).

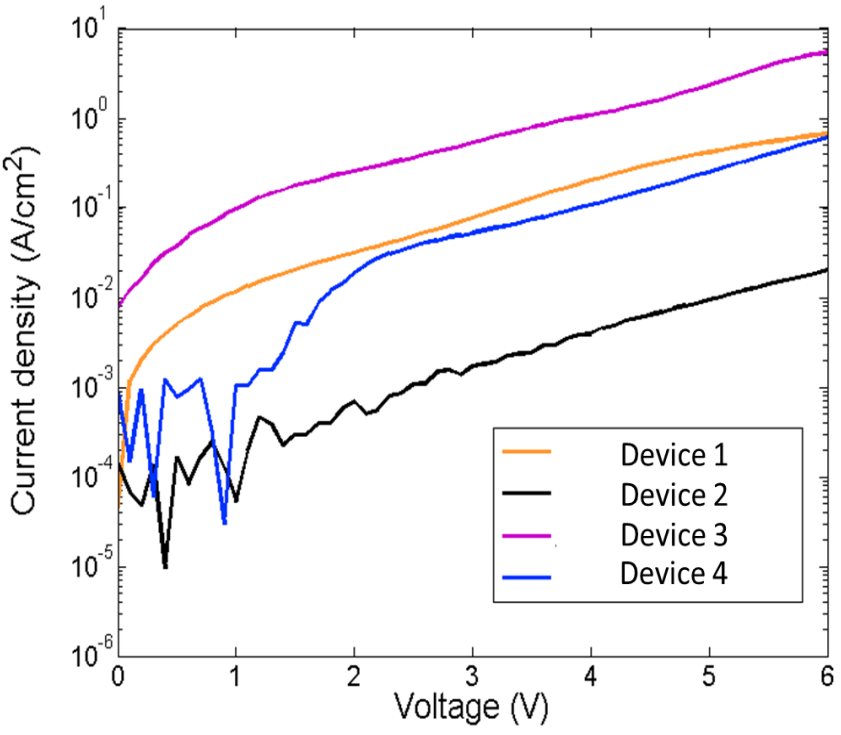

Figure 4.21: The electrical characteristics of the four control devices in Figure 4.20.

material LED. The EL images of devices 1-4 at 9V, 8V, 8V, and 4V, respectively, are shown in Figures 4.20 e-f. The big cyan squares are the borders of the overlapping areas

between Al and ITO stripes. Device 2 gave us the usual electroluminescent image, Figure 4.20f, where the light shape corresponds to the overlapping area between the electrode stripes. Device 4 also gave us the expected result where the light only appears above on the area occupied by the nanoparticles. In contrast, device 3, which contains the Au nanoparicle array but not the carpet of quantum dots does not emit any light, as shown Figure 4.20g. Lastly, light was not observed either for device 1 when both quantum dot carpet and nanoparticles were removed.

Figure 4.21 shows the current densities of the four devices investigated in Figure 4.20. Let's assume the case of device 1 as reference. When a layer of quantum dot film is added between two carrier transport layer (Device 2), the current is dropped significantly due to the poorly conductive layer of the quantum dot carpet. Yet, if the metallic nanoparticles are added in that place instead of the quantum dot layer, we saw an increased current within the device 3. The carrier injection enhancement of the metallic nanoparticles has compensated for the electrically poor conductive of the quantum dot film, as a result the current passes through the device 4 is pretty equal to that of the device 1.

Until now, we have seen that the hybridization of nanoparticle/QDs is a requirement to sustain the operation of metamaterial LEDs, it is also critical to see whether the thickness of the quantum dot film can influence the operation. The following section investigates the response of the metamaterial LEDs as a function of the thickness of the quantum dot film. Specifically, we consider the case of 3-5 monolayer thick films, obtained by spin-coating a solution of PbS CQDs with a concentration of 46 mg/mL. We also made another sample with the usual thickness (15nm corresponding to 1-2 monolayers) for comparison. Figure 4.22a displays a usual metamaterial QDLED that lights up on top of the nanoparticle arrays. As before, we have patterned several arrays with different geometries within the same LED in order to extend the generality of our observations (SEM images corresponding to the distribution of the CQDs on the nanostructures are displayed in Figure 4.22c). If we now repeat the same experiment with the thicker layer of PbS CQDs, as shown in Figure 4.22b, we totally lose the benefits of the metal nanostructures because there is no

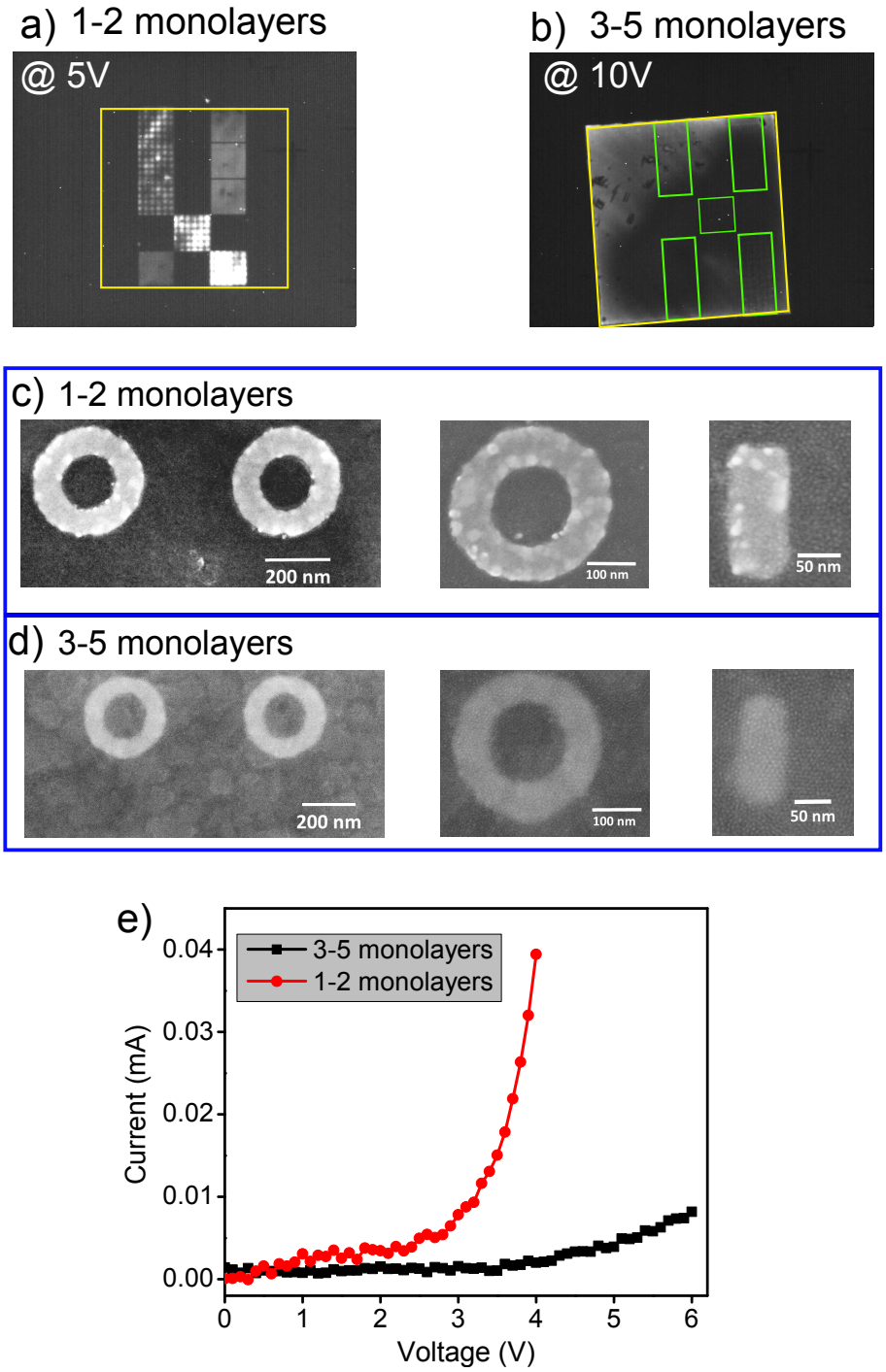

Figure 4.22: Probing the role of QD film thickness on the operation of metamaterial QDLEDs. a) The EL image of metamaterial QDLED in which the QD film is only composed of one to two monolayers of quantum dots. b) The EL image of the same metamaterial QDLED but with an active layer comprising three to five monolayers of quantum dots. c) The SEM images of the Au nanostructures covered by 1-2 monolayers of quantum dots. d) The same SEM images but the nanostructures covered by 3-5 monolayers of quantum dots. e) A J-V graph comparing the current voltage characteristics of the metamaterial QDLED with different number of monolayers of quantum dots.

preferential light emission above the Au inclusions regardless of the exact geometry and period of the arrays. In addition, the turn-on voltage is pushed to higher values and the EL intensity is much weaker since the image of Figure 4.22b has been obtained at 10V while the much brighter image of Figure 4.22a has been recorded at 5V. The assembly of quantum dots in the device of Figure 4.22b are shown in Figure 4.22d. The SEM images indicate that the nanostructures are well buried under the layer of quantum dots.

The fact that the Au nanostructures have no influence on the EL in the case of a thicker layer of CQDs further illustrates the stringent conditions that must be met to observe the effects discussed above. We interprete these results by the fact that thicker CQD films are mainly composed of dots that are too far from the metal inclusions to benefit from the Purcell effect, creating a barrier that prevents increased charge injection in the few monolayers of PbS nanocrystals placed in the near-field of the surface plasmons. This interpretation is supported by the fact that samples with thicker CQD films have a much weaker conductivity, as illustrated with the I-V curves of Figure 4.22e. In other words, these data provide another confirmation that the excitation of a plasmonic resonance is not a sufficient condition to boost the properties of the metamaterial QDLEDs and that it is also necessary to maintain a decent carrier injection in the device.

4.3.5 Influence of the metal

Last, we briefly discuss the influence of the metal used in the fabrication of the nanoparticle arrays. Figure 4.23a and 4.23b display EL images for two metamaterial QDLED with metallic nanoparticle arrays made of Al and Au, respectively. In these images, we outine with orange boxes the location of the metallic patterns. As before, several arrays with different geometries are included within each LED in order to show that our results have a large degree of generality. The arrays used in the Al metamaterial QDLED have all the same period P=600 nm and are made of rings with increasing size. They are denoted M1, M2, M5, M8 and M9 on Figure 4.23a and there reflectance spectra appear in Figure 4.23c. The Au metamaterial QDLED contains five different structures with two kinds of shapes:

nanorings and nanorods. The nanorod arrays are denoted R1, R2 and R3 and are made of Au inclusions of increasing length. As for the nanoring arrays, they are the same M8 and M9 structures as those patterned on the Al metamaterial QDLED so we will focus on these two specific arrays whenever we make quantitative comparisons between the two types of metals.

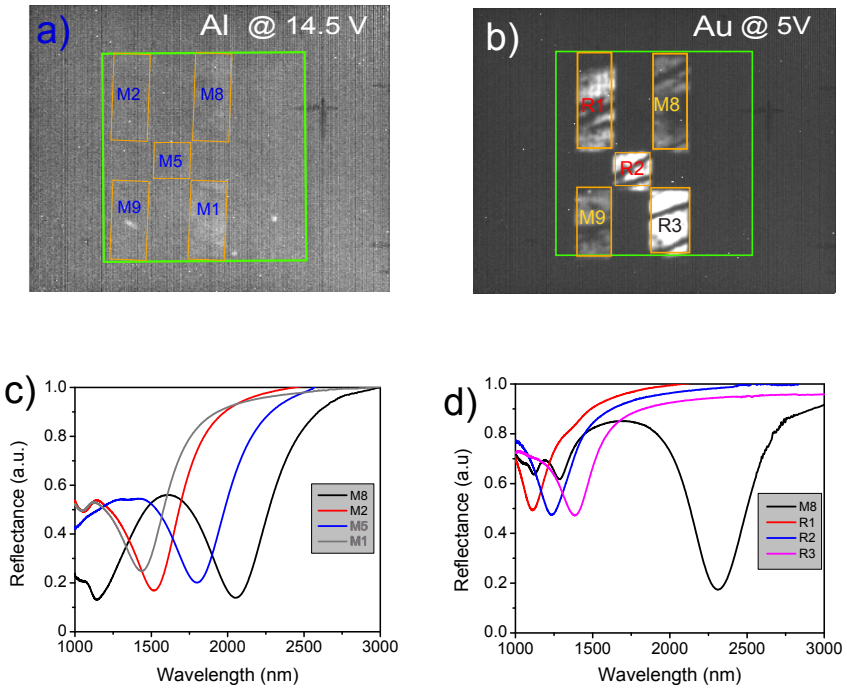

Figure 4.23: The role of metal materials on operation of metamaterial QDLED. a) The EL image of aluminum metamaterial QDLED with different nanoring structures at 14.5 V. b) An EL image of gold metamaterial QDLED with different structures at 5V. c) Reflectances of major aluminum structures. d) Reflectances of major gold structures.

Figures 4.23a and 4.23b clearly show that Al metamaterial QDLEDs perform much more poorly than their Au equivalent. Although light is only emitted above the Al patterns, as what we have observed with Au so far, it is necessary to drive the LED with a voltage exceeding 13V to generate any light. In the example of Figure 4.23a, for example, the image was taken at an applied bias voltage of 14.5V and yet the EL intensity remains very weak compared to the control sample of Figure 4.23b which was driven at 5V.

Although these observations are valid for all metallic patterns, we now solely focus

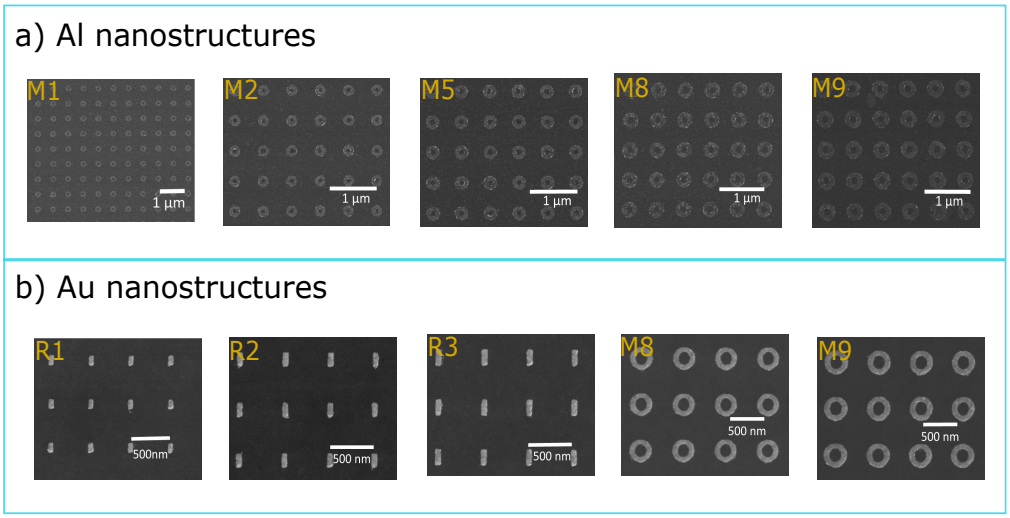

Figure 4.24: The Al and Au nanostructures investigated in Figure 4.23. a) Al nanoring arrays that are incorporated in the samples of Figure 4.23. From left to right are nanorings of increasingly larger sizes while the period is kept constant at 600 nm. b) Au nanorod and nanoring structures. Arrays of nanorings (M8 and M9) have the same dimensions as those in Figure 4.18. Arrays of nanorods R1, R2 and R3 have the same period p = 500 nm, width = 50 nm and thickness = 25 nm, but the length is varied from 125 nm, 150 nm, and 175 nm, respectively.

on structure M8 which is common to both the Al and Au samples, as shown in Figure 4.24. The reflectance spectra of Figures 4.23c and 4.23d show that in both the Al and Au cases, the M8 structure operates through higher order plasmonic modes in the frequency range of interest (i.e. in the 1000-1500 nm window). However, it can be seen that the Al structure exhibits much more losses since the reflectance in the 1000 - 1500 nm spectral range is much lower than for the case of Au, even far from the plasmonic resonances. This conclusion is consistent with the known values of the complex permittivities of Al and Au in the near-infrared since the dielectric loss tangent of Al is typically 5 times higher than Au in this regime [195]. In other words, it is reasonable to attribute part of the much poorer performances of the Al-based metamaterial QDLEDs to the fact that the Al structures have a much higher damping factor in the near infrared.

This being said, there may be other factors contributing to the high inefficiency of Al-based metamaterial QDLEDs. In particular, Al and Au have different work functions

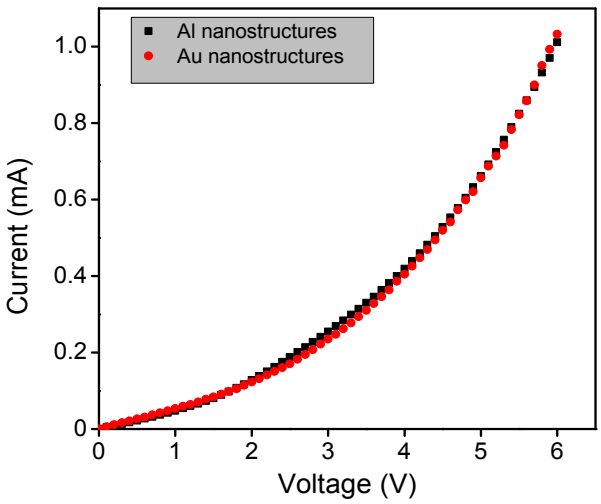

Figure 4.25: The current-voltage responses of metamaterial QDLEDs as the integrated nanostructures are made of Al and Au metals.

(Al ≈ 4.2 eV, Au ≈ 5.3 eV) and the nature of the contact between the metallic inclusions and the PbS CQDs should depend on this parameter. We did not have the time to study this issue during this thesis and so we do not know whether the contact between the PbS CQDs and the Al inclusions is ohmic or Schottky (according to the literature, the nature of the contact between Au and PbS CQDs is ohmic [194]). However, we note that the current-voltage characteristics of Al-based and Au-based metamaterial QDLEDs are almost identical, as evidenced on Figure 4.25, suggesting that electrical injection is similar in both cases and that this factor does not play a major role in the much poorer performances of Al-based structures.

4.3.6 Lifetime of optimized devices

Here we go back to the working Au-based structures of sections 4.1 and 4.2 and discuss how their characteristics vary over time when pumped by a continuous and constant bias voltage. Figure 4.26 shows the result for an applied voltage of 4V by simultaneously plotting the current density and light intensity over three consecutive hours.

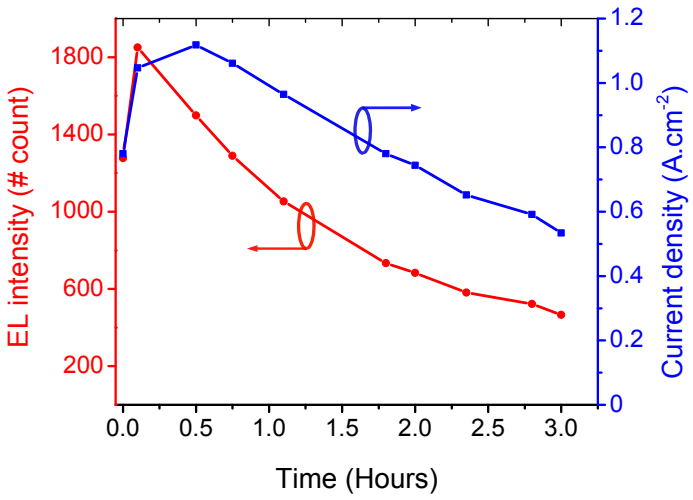

Figure 4.26: Lifetime of metamaterial LEDs with small rings. The voltage was kept constant at 4V.

One can see that the current density and light intensity follow the same behavior, namely they first increase and then decrease with different decline slopes. This behavior is similar to that of the conventional QDLEDs of chapter 3 and those of other works [196, 197, 198]. The initial increase of the curves can be mainly attributed to the memristive behavior of the TiO_2 electron transfer layer while the gradual decrease is generally ascribed in the literature to charging effects that account for increased difficulties of carriers passing through the devices overtime. Specifically, the long dot inter-distance, defects in the dots and at their surface gradually lead to carrier trapping which in turn creates an increasingly higher charge barrier that prevents the movement of the charges, causing a reduction of the current and a decline in EL.

With these measurements, we put our qualitative description of the metamaterial QDLEDs to an end. All the parameters that we have varied reveal one important thing—namely, that very stringent conditions must be met so that the metallic arrays play a role in the QDLED operation. A slight deviation in the thickness of the CQD film, or in the spacing between the CQDs and the metallic particles, or in the metal used to fabricate the latter structures, is enough to kill the effects described in sections 4.1 and 4.2. However, once the optimal conditions are met, the results presented in this chapter

are fully reproducible, included with PbS CQDs with different diameters and excitonic band gap as will be shown later. Although we have tried to offer a reasonable explanation of the operation mechanism, which involves a delicate balance between the excitation of surface plasmon resonances, good injection and relatively low losses, further studies are needed to fully clarify the physics at work in our structures.

4.4 Metamaterial QDLEDs: a novel form of active metasurfaces.

In this section, we will show that the metamaterial QDLEDs do not only lead to better performances than conventional QDLEDs, but also that they represent a true novel form of artificial active medium. To this end, we now consider metamaterial QDLEDs having arrays of gold nanorods with dimensions of 150 nm long, 70 nm wide and 25 nm thick, and a period of 500 nm.

Figure 4.27 shows that the basic properties of this new geometry are essentially similar to those already discussed for Au nanorings. In particular, the EL intensity does not depend on the area occupied by the nanorod arrays and the onset of light emission occurs at approximately 2V.

However, due to their geometry, the plasmonic resonances supported by nanorods can only be excited and reemit light with an electric field parallel to their long axis, as evidenced with the FTIR spectrum of Figure 4.28a. This polarization dependence dominates the response of the metamaterial QLED, as shown in Figure 4.28b where most of the light emitted by the structure is polarized along the long axis of the rods. This result is all the more remarkable that the nanorods occupy a small fraction of the total surface of the array (4.2 %), implying that the CQDs that are not coupled to them are not active. For comparison, we show in Figure 4.28c the photoluminescence spectra of the device for the two same orthogonal polarizations. In this experiment, a 632 nm laser beam is focused on the sample with a 50X objective that excites all the dots under the focus

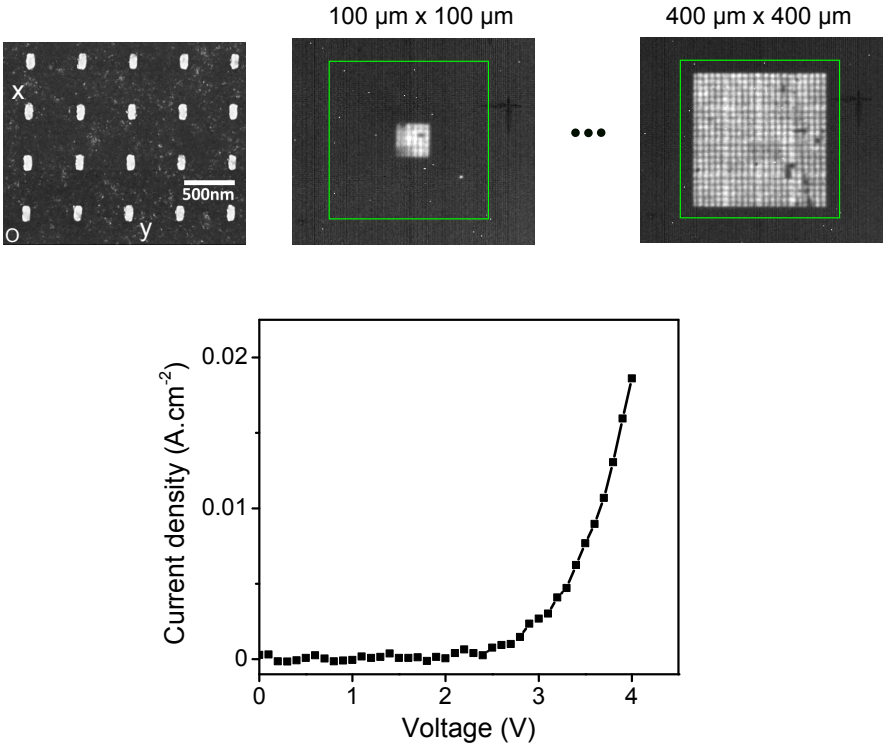

Figure 4.27: The electrical charateristics of nanorod arrays. a) a SEM image of nanorod used in this study. b) Electroluminescence from 100 x 100 μm nanorod arrays with a green square representing the area of the QDLED. c) Electroluminesncence from 400 x 400 μm nanorod arrays. d) The current density-voltage of the 400 x 400 μm nanorod arrays.

spot (i.e. those that are coupled to the rods and those that aren't). The resulting spectra are also sensitive to the polarization but in a strikingly less marked way than in Fig. 4.28b, implying that the vast majority of the dots are not coupled to the nanorods and emit unpolarized light. This conclusion is reinforced by the fact that the PL spectrum of the structure with the polarization perpendicular to the rods is almost undistinguishable from the PL spectrum of PbS CQDs far from any metal structuration (also plotted in Figure 4.28c).

In other words, the combined results of Figures 4.28b and 4.28c indicate that most of the dots between the gold nanostructures are likely not emitting when pumped electrically (which is in contrast with optical pumping). These data demonstrate a new kind of structural electroluminescence with discrete, subwavelength elements. Not only can we tailor the electrical and optical properties of the structure, as seen before, but we can also

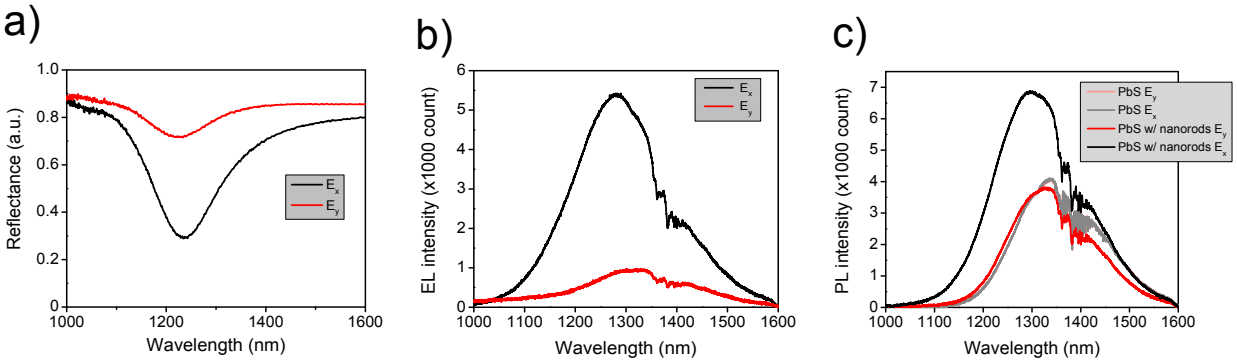

Figure 4.28: Characterization of 400 x 400 μm^2 nanorod arrays. a) Reflection spectra of the nanorods with two polarization E_x and E_y. b) EL spectra recorded at 4V when the polarizer is placed along the nanorod length (E_x) in black and perpendicular to the nanorod (E_y) in red. c) The PL spectra of PbS QDs of a reference device and a device with the presence of the rod arrays

consider that each gold inclusion and the dots in its immediate proximity form active pixels of subwavelength dimensions that can be used to weave complex light-emitting surfaces. As an illustration, we have fabricated a metamaterial QDLED displaying different words depending on the polarization through which we look at the structure: the word "Nano", appearing in black over a white background, and the word "Saclay", appearing in white over a black background. The structure contains two arrays, one made of vertically-oriented nanorods with voids corresponding to the word "Nano" and the second with horizontally-oriented nanorods shaping the word "Saclay". The structure is shown in Figure 4.29.

Figure 4.30 shows the light emitted from the device for the two orthogonal polarizations. At a given voltage, each of the encoded words will appear depending on the polarization: the word "Nano" in Figure 4.30a emerging in black, corresponding to the voids where there are no vertical nanorods, over a white luminescence square background. In the same block position, as one switches polarization to 90°, the word "Saclay" appears in white, corresponding of the PbS coupled with horizontal nanorods, on a black background without horizontal nanorods. Clearly, each word appears distinctively for one polarization only, demonstrating that the nanorods coupled with their surrounding dots act as discrete pixels as intended.

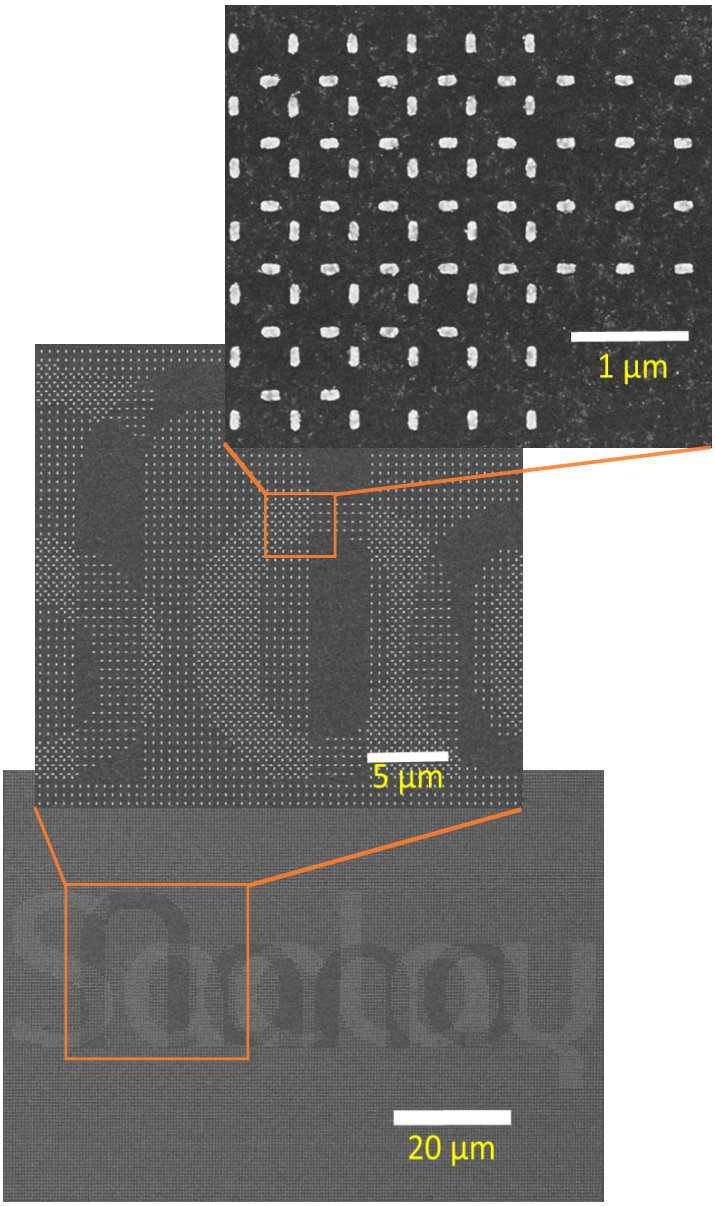

Figure 4.29: The SEM image of the "NanoSclay" structure. The words "Nano" and "Saclay" are patterned in a single 100 x 100 μm^2 area comprised of two arrays of orthorgonal nanorods. The voids in a vertically-oriented nanorod array constitute "Nano", whereas the horizontally-oriented nanorods make the word "Saclay".

Figures 4.30c and 4.30d are a repetition of the same demonstration above with two intertwining arrays with the same nanorod dimensions, but using a different batch of PbS CQDs with a smaller diameter and thus a slightly blue-shifted emission. These images show that the concepts introduced in this chapter are reproducible as long as the stringent conditions are met as discussed in the previous section. Until here, it is necessary

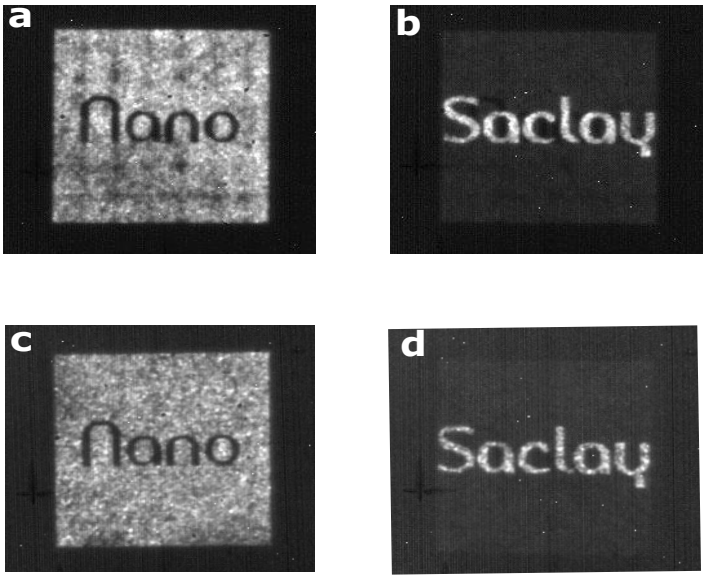

Figure 4.30: The EL images of NanoSaclay at 4V. a) The image of the black "Nano" word is captured with the polarizer placed along the vertical nanorods. b) The word "Saclay" appears in white on a black background by switching the polarizer by 90°. c) and d) are the repeated device with slightly smaller quantum dots.

to stress out that our devices can be regarded as genuine metamaterial. Why? Because as discussed in section 4.4, each metallic nanoparticle (150 nm in length) and its surrounding QDs acting as a discrete pixel emitting light at around 1500 nm and the inter distance between the intertwining nanoparticles is only 140 nm. Therefore, these pixels are highly subwavelength and very close to each other led to a homogeneous lightening surface whose individual pixels are not distinguishable. The infrared metamaterial devices also satisfy the definitions of metamaterials in the sense that all the macroscopic properties of the devices (emission color, emission image, polarization, and even electrical property) are controlled by the geometry of the metallic nanoparticles.

4.5 Conclusion

In this chapter, we have have successfully incorporated Au nanoparticle arrays in the architecture of PbS based LEDs resulting in metamaterial LEDs. We have demonstrated dramatically enhanced performances, including the lowest threshold voltage ever observed

for a PbS-based infrared LED, as well as an unprecedented control over the electrical, spectral and polarization properties of the structures. More importantly, we have shown that the active layer cannot be considered as formed by only the CQD film or metallic nanoparticles, but rather by a hybrid metamaterial resulting from the coupling between two types of artificial atoms—the PbS nanocrystals and the unit cells of the metallic Au arrays. As a result of this coupling, light is emitted by subwavelength, nanosize pixels that can be individually tuned to exhibit independent optoelectronic properties. Such elementary building blocks can be arranged at will to form intricate artificial structures, radically increasing the functionalities of imaging devices. In the example used in Figure 4.30 to illustrate this claim, we used a set of identical light-emitting elements but one can also create pixels of different colours by tuning the geometry of the gold inclusions, as demonstrated with several figures of section 4.3. It should also be possible to enable phase coherence between the different plasmonic resonances and thus achieve a collective behaviour to shape complex beams or generate holographic images. The results shown here lay the foundation for future works, both for having a better understanding of the processes at work in the light emission and for fully exploring the possibilities offered by this new form of artificial electroluminescence.

Chapter 5

Conclusion and future outlooks

5.1 Thesis summary

In this dissertation, we have hybridized two classes of artificial structures by introducing metamaterial quantum dot light-emitting-diodes. The findings from this work have brought a new form of structural electroluminescence where power consumption, color, intensity and polarization of the light emitted from the diodes were controlled by the design of the metamaterials. This result represents the first electrically-pumped metamaterial structures ever demonstrated in the optical regime.

To obtain these results, we have performed a number of intermediate steps that helped us become familiar with CQDs and plasmonic nanostructures. Firstly, we performed a series of PL measurements under different conditions to understand the behavior of PbS quantum emitters embedded in a host matrix. We studied the coupling efficiency as well as the interactions between PbS CQDs and plasmonic nanoring antennas. We also introduced the two-level system that is widely used in describing the interactions of optical antennas and quantum emitters and showed that it was not adapted to our system. This discrepancy has been explained by the inhomogeneous broadening of the dots and the existence of at least two distinct channels of emission associated with CQDs that are not in the assumption list of the two-level model. A new theoretical framework developed by

Prof. J.-J. Greffet was then shown to provide a satisfying description of our experimental findings.

Secondly, we learned how to fabricate a CQD-based optoelectronic device. All-inorganic top-emission infrared quantum-dot light-emitting-diodes were successfully fabricated to meet the characterization equipments available in the laboratory. Although the devices operate at high voltage and with low brightness, we were able to fabricate stable and reproducible QDLEDs that have served as solid platforms for the final goal of this dissertation, namely to hybridize these structures with metamaterials.

Finally, we incorporated the nanoparticle arrays into our top emission QDLEDs. We presented a detailed discussion about the fabrication of the full devices and explained that it is the combination of the plasmonic arrays and the CQDs that constitutes a new form of artificial active medium, or metamaterial. We found remarkably that the electroluminescence only occurs in the zone of the metamaterial/CQDs hydrid. Besides, light pattern was controlled by geometry of the nanoparticles, and we also observed a number of different changes taking place simultaneously, i.e. a dramatic reduction of the turn-on voltage, a sharp enhancement of the emission intensity, altered color and polarization of the light emission of the LEDs. A series of control experiments were carried out the find out the origins of the all the observed effects.

5.2 Future outlooks

Although a series of controlled experiments were performed to reveal the operating mechanisms of the metamaterial QDLED, the full physics at work in the metamaterial/CQD hybrids is far from being well understood. One of the most immediate follow-ups of this thesis is therefore to fully clarify how these devices operate. Besides macroscopic measurements, a number of nanoscale probing experiments are envisioned in collaboration with other groups of the Paris Saclay area such as STM-induced electroluminescence studies.

Incorporating plasmonic arrays offered a novel approach to reduce significantly the

operational voltage of QDLEDs. In other words, the metamaterials transformed a bad LED (turn-on voltage at 6.5 V) to an excellent one (turn-on at 1.3 V) which is in line with other state-of-the-art QDLEDs (turn-on at 1.2 V) [192] that optimize the energy band diagram and increase the conductivities of the involved layers. If one combines the two approaches, the idea of extremely low-power consumption optoelectronics with a turn-on voltage of just a few hundreds mV may be very feasible in near future. It would put the threshold voltage below the thermodynamic limit set by the bandgap energy, a prowess that has already been obtained in the visible for other QDLED designs.

Metamaterial QDLEDs might provide a solution for ultrahigh resolution displays. Recent breakthroughs on the race of ultrahigh resolution displays have recorded 5 μm as the smallest white light pixel [199]. A set of three metallic nanostructures within a single unit cell can be served as sub-pixels for three basic blue, green, and red colors to hold a promise of white light pixel in the range of 1-2 μm.

Metamaterial QDLEDs do not only improve the performance and efficiency, but they provide additional control to the light emission since they operate through discrete nanoscale pixels. It should be possible to use this approach to design a metasurface in which the light will be emitted in a preferred orientation and/or the phase of the light will be tailored to create complex light beam such as spiral vortex or hologram. Lasing from an array of nanoantennas coupled with quantum emitters by a complex and cumbersome optical systems was demonstrated recently [40]; our results suggest that much more compact designs are at hand following our approach.

One of the major applications of films of CQDs fall in the regime of light harvesting devices such as photodiodes and photovoltaics. Our findings should also be applicable for these applications by operating the diodes in reverse bias. In particular, it would be interesting to use the same metamaterial approach to build sensors with nanoscale pixels and to exploit the plasmonic enhancement to obtain ultra-short responses-a much needed property at infrared wavelengths where ultra-fast CCD cameras do not operate.

For the field of plasmonics and metamaterials, this first demonstration of electrically-

driven nanostructures can be regarded as an alternative approach for applications requiring or replacing the cumbersome optical systems by compact electrically-driven components.

I close this thesis by emphasizing that only applications immediately beneficial from this work are discussed here. More generally, our research shows the enormous synergy of combining different types of artificial matter and suggests that many other opportunities will arise by taking a unified view of the various artificial media developed by the physics, chemistry and engineering communities.

Appendix A

Fabrication of the samples studied in Chapter 2

Step-by-step recipe for fabricating samples that comprises a glass substrate, the nanoring arrays, a thin SiO_2 spacer, a layer of HSQ doped with PbS CQDs and a pure, undoped layer of HSQ:

1. Substrate preparation

- 1x1 cm glass pieces are prepared by cutting 2-inch wide and 300 μm thick glass substrates with a dicing machine.

- The 1x1 cm glass substrates are soaked in acetone and cleaned in an ultrasonic bath for 3 hours at 40 ^{o}C. The substrates are then rinsed immediately with Acetone, Isopropanol (IPA), and DI water before drying them with N_2 gas.

2. Fabricating the Au nanoring arrays

- A beaker (or a vial) is kept in an oven at 120 ^{o}C overnight to dehydrate it before it is used for preparing the e-beam resist.

- A 1.215 ml mixture of positive e-beam resist ZEP-520A (ca 5.5%wt) and Anisole thinner, dilution DR=2.0, is mixed in the baked beaker.

- Microprimer Adhesion promoter is spun on the sample at 2600 rpm during 1 minute.

- The prepared e-beam resist is applied on the sample through a 0.24 μm filter and

spun at 2600 rpm during 1 minute. The thickness of the resist is around 60 nm.

- The e-beam resist is soft-baked at 190 ^{o}C for 3 minutes on a hotplate.

- A conductive layer (Espacer 300Z) that will evacuate charges during e-beam writing is finally spun on top of the resist at 4000 rpm for 30 seconds.

- The conductive layer is baked at 90 ^{o}C for 2 minutes on a hotplate.

- Marks at corners of the sample are made manually with diamond scribe to find the focus values for e-beam writing.

- Masks of the structure are designed with Raith GDSII graphic editor and fractured with Nanobeam Pattern.

- The e-beam is generated at voltage 80 kV and current 2.0 nA. To write the structures of chapter 2, the resist is exposed with a dose of 3 C/m^2.

- After e-beam exposure, the conductive layer on the sample is removed by dipping the sample in DI water for 20 seconds and blowing it with N_2.

- Development: The substrate is soaked in ZED-N50 for 40 seconds, Methyl IsoButyl Ketone (MIBK) : IPA(1:3 %v) for 30 seconds. Stopping the development by immersing the substrate in IPA for 30 seconds and blowing with N_2.

- Metal deposition: A Plassys E-beam evaporator is used for depositing an adhesion layer of 2 nm of titanium at 7x10^{-8} Torr followed by 33nm of gold evaporated with a rate of 1 Å/s at 8x10^{-8} Torr.

- The metal parts covering the unexposed resist are lifted-off by immersing the sample in 2-Butanone solution overnight. An ultrasonic bath of 5 seconds is used to remove the unwanted metals completely. Samples are continuously rinsed with 2-Butanone, IPA, and DI water before drying with N_2.

- The fabricated nanorings are visualized by Scanning Electron Microscopy (SEM Hitachi SU8000). To minimize charging effects, it is necessary to coat the sample with a conductive layer, ESPACER 300Z, by spinning at 4000 rpm for 30 seconds and baking at 90 ^{o}C for 2 minutes. This layer is subsquently removed to continue the fabrication process.

3. Covering the nanorings with a dielectric spacer

Plasma Enhanced Chemical Vapor Deposition is employed for generating silica spacer of the nanorings with quantum dots. Low frequency (f = 138 KHz) mode is used with deposition rate: 1 Å/s.

4. Applying the HSQ layer doped with PbS CQDs

- 400 μl of 6%wt hydrogen silsesquioxane (HSQ, purchased from Dow Corning under the commercial name XR-1541) are mixed with 200 μl of MiBK (98% purity) in a dehydrated vial. 150 μl of PbS QDs in toluene (concentration 5mg/mL) purchased from Evident Technologies are then added to the solution.

- The resulting solution is filtered (with a 0.24 μm filter), spun onto the sample at 3000 rpm for 1 minute, and soft-baked at 150 ^{o}C for 2 minutes. This creates a 100nm thick layer of SiO_2 sol-gel containing PbS quantum dots.

5. Symmetryzing the sample with a pure layer of HSQ

Finally, the sample is coated by a pure undiluted XR1541 resist spun at 1000 rpm and baked at 150 ^{o}C for 2 minutes. The resulting thickness of the SiO_2 sol-gel is 190 nm.

Appendix B

Determining the apparent PL enhancement

Each PL Enhancement Spectrum (PLES) was obtained according to the following formula: PLES = (PL above the structure - PL background)/(PL above glass - PL background) where PL above the structure and PL above glass are the collected signal emitted by the CQDs in the presence and absence of the plasmonic nanorings arrays, respectively, and PL background is the noise recorded in the absence of pumping. As an example, the PLES procedure for one of our structures, which is unrelated to the graphs showed in the main text, is illustrated in Figure S1. PL recorded above the structure, PL recorded above the bare glass, and the background are the red, the blue, and the black curves, respectively (Figure S1a). The actual emission signal of the QDs on the structure and on the bare glass after substrating the background are the red and blue curves of the Figure S1b. Finally, the ratio of these two quantities is plotted in Figure S1c.

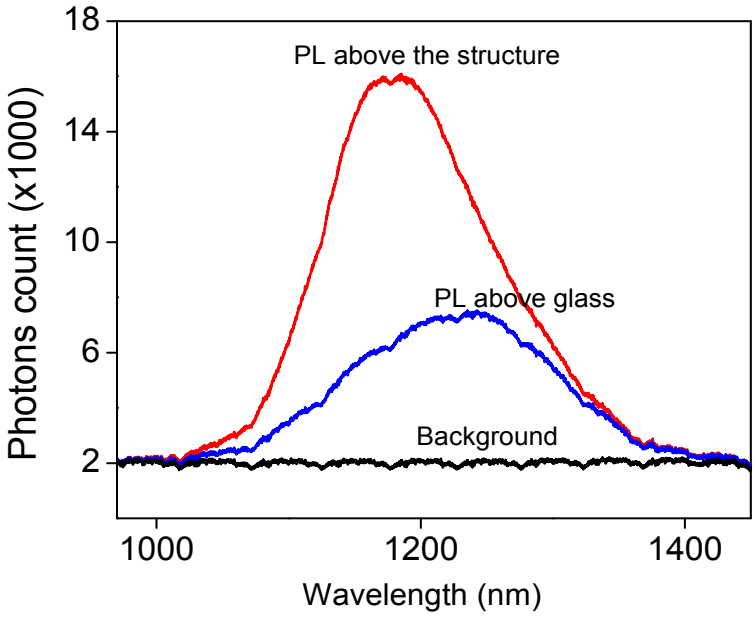

Figure B.1: PL spectra of dots in the presence and in the absence of the nanorings accompanying with the background

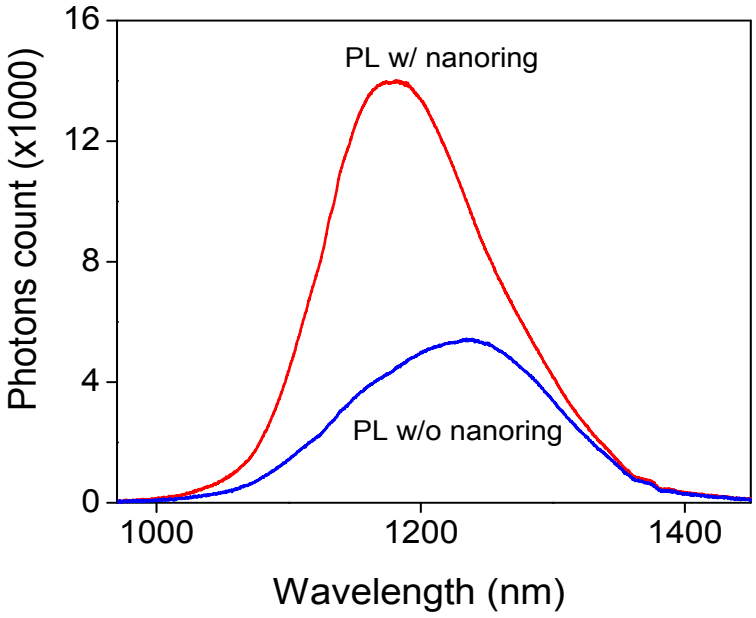

Figure B.2: PL spectra of dots in the presence and in the absence of the nanorings after subtracting the background

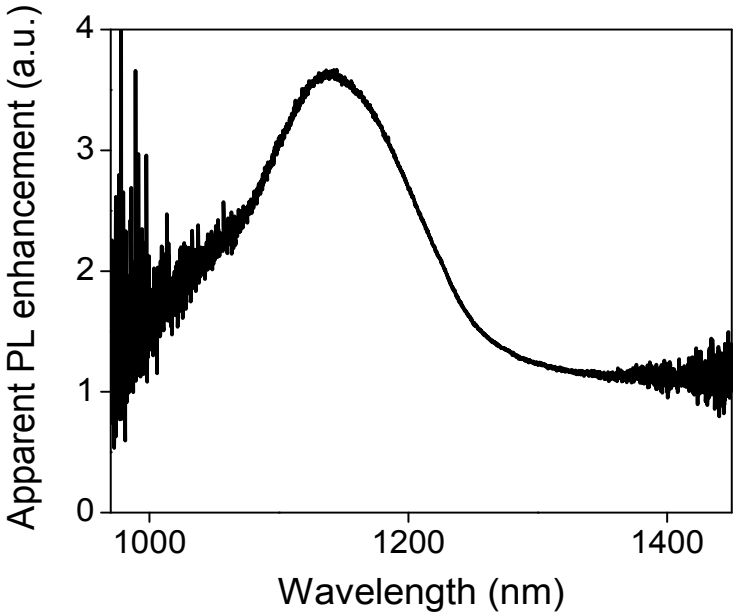

Figure B.3: PL enhancement after normalization

Appendix C

Fabrication of top emission infrared QDLEDs

1. Substrate preparation (glass or Si)

- 1x1 cm glass pieces are prepared by cutting 2-inch wide and 300 μm thick glass wafer with dicing saw.

- 1x1 cm Si substrates are prepared by cutting 2-inch wide and 300 μm thick one-face polished Si wafer with dicing saw.

- Both glass and Si substrates are soaked in acetone and cleaned in an ultrasonic bath for 1 hour. The substrates are then rinsed immediately with Acetone, Isopropanol (IPA), and DI water before drying them with N_2 gas.

- The Si pieces are treated with Piranha solution (H_2SO_4 96% : H_2O_2 30% 3:1%v), rinsed thoroughly in N_2 soaked DI water sink and dried out with N_2 gun. They are then coated with SiO_2 by Plasma Enhanced Chemical Vapor Deposition (PECVD) at 300 °C and low frequency mode (384 KHz) at a rate of 11 Å/s until reaching 500 nm of SiO_2.

- All substrates are finally cleaned with Oxygen plasma 10 min (DC mode, 160 W, 5 mbar).

2. Creating Aluminum cathodes

- A copper foil shadow mask is firmly hold on top of each substrate pieces to make

the Al cathodes. Al is evaporated through the mask with Plassys e-beam evaporator at pressure 7x10^{-8} torr and velocity 12 Å/second. After removing the mask, 4 aluminum strips are obtained with width = 500 μm, thickness 80 nm and distance between two electrodes is 1.5 mm.

3. Covering Aluminum cathodes with a mesoporous TiO_2 electron transport layer

- A thin Kapton tape is applied on one side of the samples so as to protect one end of the Al electrodes.

- 70 μl of anatase TiO_2 nanoparticles in solution (Ti-Nanoxide HT-L/SC, Solaronix) are spincoated at 5000 rpm for 60 seconds in a closed spincoater saturated with EtOH vapor followed by baking at 200 ^{o}C for 15 minutes in air. The resulting mesoporous TiO_2 layer has a thickness of 60 nm.

4. PbS CQDs film

A thin film of PbS CQDs in toluene (conentration 26 mg/ml, purchased from Evident Technologies) is spincoated in an open spincoater with a ramping speed of 400 rpm/s and a constant speed of 2000 rpm for 15 seconds, followed by a hot bake at 150 ^{o}C for 3 minutes.

5. MoO_x Hole transport layer

MoO_x is deposited by RF magnetron sputtering mode in a Denton sputtering system. We used a 3 inch wide Mo target (Mo 99.98%, Kurt J. Lesker) in a reactive gas environment with $\%O_2/(Ar + O_2)$ = 15% and power of 50W. The final gas pressure for sputtering is 10 μbar and rate of deposition is 0.2 Å/s. To enhance the uniformity of MoO_x we rotate the sample holder at a speed of 20 rpm.

6. Transparent anode-ITO

Before sputtering ITO, the same shadow mask used for defining the Al cathodes is placed on the sample but rotated by 90^{o} with respect to the Aluminum strip direction. As

discussed in the main text, to enhance the mechanical stability of ITO on the underneath layer, it is sputtered in a two-step process, with the beginning step at low power and the second sputtering at higher power.

ITO is sputtered in pure Ar enviroment with a 3 inch wide target ITO (99.99 % Kurt J. Lesker) and pressure of sputtering is maintained at 8 μbar.

- The first step is proceeded with 30W of power in RF mode, as a result the deposition rate is around 0.5 Å/s until it is 10 nm thick.

- The second step is carried out with a higher power of 80W in RF mode, corresponding to a deposition rate of 2.7 Å/s. It is stopped after 80 nm of ITO are deposited.

Appendix D

Fabrication procedure of Metamaterial QDLEDs

The fabrication procedure is actually inherited from previous the fabrication processes for nanorings in Chapter 2 and colloidal quantum dot light-emitting-diodes in Chapter 3. As analyzed with different SEM images at different stages during the fabrication, the metamaterial LED architecture can be visualized with the following cartoon:

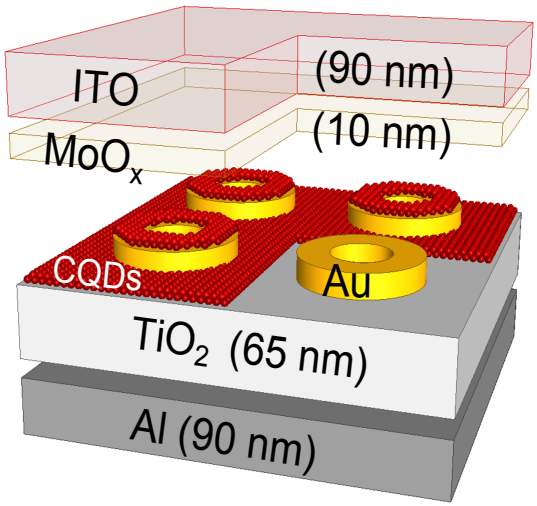

Figure D.1: The cartoon of metamaterial LED with nanorings as a cellular element.

Following is the detailed procedure for fabricating the metamaterial LEDs.

1. Substrate preparation (Glass or Si)

- 1x1 cm glass pieces are prepared by cutting 2-inch wide and 300 μm thick glass wafer with dicing saw.

- 1x1 cm Si substrates are prepared by cutting 2-inch wide and 300 μm thick one-face polished Si wafer with dicing saw.

- Both glass and Si substrates are soaked in acetone and cleaned in an ultrasonic bath for 1 hour. The substrates are then rinsed immediately with Acetone, Isopropanol (IPA), and DI water before drying them with N_2 gas.

- The Si pieces are treated with Piranha solution mixing H_2SO_4 96% with H_2O_2 30% (3:1%v) and rinsed well in N_2 soaked DI water sink and dry out with N_2 gun. They are then coated with SiO_2 by Plasma Enhanced Chemical Vapor Deposition (PECVD) at 300 ^oC and low frequency mode (384 khz) at a rate of 11 Å/s until reaching 500 nm of SiO_2.

- All substrates are finally cleaned with Oxygen plasma 10 min (DC mode, 160W, 5 mbar).

2. Creating Aluminum cathodes

- A copper foil shadow mask is put and firmly hold on top of each substrate pieces to make the Al cathodes. Al is evaporated with e-beam evaporator at pressure $7x10^{-8}$ torr and velocity 12 Å/second. After removing the mask, 4 aluminum strips are obtained with a width = 500 μm and the distance between two electrodes is 1.5 mm.

3. Covering Aluminum cathodes with electron transport layer: spincoating anatase TiO_2.

A thin Kapton tape is applied on one side of the samples so as to protect one end of the Al electrodes.

- 70 μl of anatase TiO_2 nanoparticles in solution (Ti-Nanoxide HT-L/SC, Solaronix) are spincoated at 5000 rpm for 60 seconds in a closed spincoater saturated with EtOH vapor followed by baking at 200 ^oC for 15 minutes in air. The resulting mesoporous TiO_2 layer has a thickness of 60 nm.

4. Fabricating nanostructure arrays by e-beam lithography on granular TiO_2 surface.

- Preparing e-beam resist in a dehydrated beaker: a 1.215 ml mixture of positive e-beam resist ZEP-520A (ca 5.5%wt) and Anisole thinner, dilution DR 2.0.

- A thin Kapton tape is applied on protected side of the samples to protect the Al electrode contacts.

- Spinning Micro primer as adhesion promoter for e-beam resist at 2600 rpm during 1 minute.

- Spinning the filtered e-beam resist with 0.24 μm filter at 2600 rpm during 1 minute. The thickness of the resist is around 60 nm.

- Soft bake the e-beam resist at 190 ^{o}C for 3 minutes on a hotplate.

- Coating a conductive layer: Espacer 300Z is spinned at 4000 rpm for 30 seconds.

- Soft bake the conductive layer at 90 ^{o}C for 2 minutes on a hotplate.

- Marks on the baked resist on top of Al cathodes are made with diamond knife to find the focus values for e-beam writing.

- A manual alignment is performed with the edge of each Al stripe as origins and the distance between one structure to the other structure on the same Al stripe is 2 mm.

- Masks of the structure are designed with Raith GDSII graphic editor and fractured with Nanobeam Pattern.

- The e-beam is generated at voltage 80kV and current 2.0 nA. To write the structures in the chapter 2, the resist is exposed with a dose of 3 C/m^2.

- After e-beam exposure, the conductive layer on the sample is removed by dipping in DI water for 20 seconds and blow with N_2.

- Development: Soaking the substrate in solutions of ZED-N50 for 40 seconds, Methyl IsoButyl Ketone (MIBK) : IPA(1:3 %v) for 30 seconds. Stopping the development by immersing the substrate in IPA for 30 seconds and blow with N_2.

- Metal deposition: A Plassys E-beam evaporator is used for depositing an adhesion layer of 2 nm of titanium at 7x10^{-8} Torr followed by 25nm of gold evaporated with a rate

of 1 Å/s at 8x10^{-8} Torr. In the case of Al: 25 nm of aluminum is deposited (1.2 Å/s) at 8x10^{-8} Torr.

- The metal parts covering the unexposed resist are lifted-off by immersing the sample in 2-Butanone solution overnight. An ultrasonic bath of 5 seconds is used to remove the unwanted metals completely. Samples are continuously rinsed with 2-Butanone, IPA, and DI water before drying with N_2.

- The samples with fabricated nanostructure arrays are now ready for further characterization and fabrication step.

5. PbS CQDs thin film.

A thin film of PbS CQDs in toluene (concentration 26 mg/ml, purchased from Evident Technologies) is spincoated in an open spincoater with a ramping speed of 400 rpm/s and a constant speed of 2000 rpm for 15 seconds, followed by a hot bake at 150 ^{o}C for 3 minutes.

6. Hole transport layers.

- A thin Kapton tape is applied on protected side of the samples to protect the Al electrode contacts.

- MoO_x is deposited by RF magnetron sputtering mode in a Denton sputtering system. We used a 3 inch wide Mo target (Mo 99.98%, Kurt J. Lesker) in a reactive gas environment with $\%O_2/(Ar + O_2) = 15\%$ and power of 50W. The final gas pressure for sputtering is 10 μbar and rate of deposition is 0.2 Å/s. To enhance the uniformity of MoO_x we rotate the sample holder at a speed of 20 rpm.

7. Transparent anode-ITO.

Before sputtering ITO, the same shadow mask used for defining the Al cathodes is placed on the sample but rotated by 90^{o} with respect to the Aluminum strip direction. As discussed in the main text, to enhance the mechanical stability of ITO on the underneath layer, it is sputtered in a two-step process, with the beginning step at low power and the second sputtering at higher power.

ITO is sputtered in pure Ar enviroment with a 3 inch wide target ITO (99.99 % Kurt J. Lesker) and pressure of sputtering is maintained at 8 μbar.

- The first step is proceeded with 30W of power in RF mode, as a result the deposition rate is around 0.5 Å/s until it is 10 nm thick.

- The second step is carried out with a higher power of 80W in RF mode, corresponding to a deposition rate of 2.7 Å/s. It is stopped after 80 nm of ITO are deposited.

Appendix E

Changes of metallic inclusions in QDLEDs

The past decades have witnessed huge advances in nanofabrication in which nanostructues are typically patterned on a flat substrate. However, to the best of our knowledge, we are the first to have attempted to make nanostructures on a mesoporous layer of TiO_2 rather than on a smooth substrate. As discussed in the text, the RMS of our TiO_2 layers is 4.6 nm according to AFM measurements. Although such a roughness is small compared to the typical size of the grains forming the Au nanoparticles, one can wonder how it affects the plasmonic resonances. This appendix will briefly discuss this point as well as how the plasmonic resonances evolve when they are integrated in a full device.

Figure E1 displays the reflectance spectra of arrays of nanorings embedded in different environments. The graphs show that the lithographied nanorings fabricated on a flat glass substrate (black curve) have a narrower resonance compared to those fabricated on a mesoporous TiO_2 layer (red curve). These differences are even more marked if the nanorings are covered by a top layer of nanoparticle TiO_2 (blue curve).

Now we turn to discuss the evolution of the plasmonic resonances as we integrate the lithographied nanoparticle arrays inside our QDLED's architecture. The left graph of Figure E.2 displays the reflectance of nanorings embedded in TiO_2. At the plasmonic

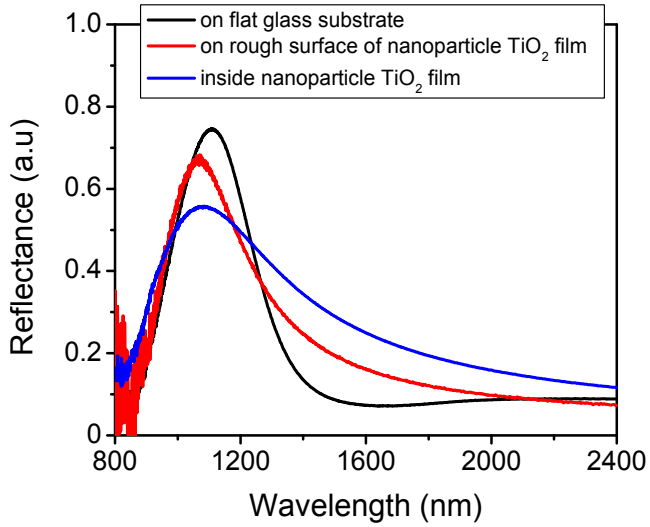

Figure E.1: Response of Au nanoring arrays in different environments. The average inner, outer diameter, and height of the Au nanorings are 110nm, 230nm and 33 nm, respectively. The distance from center of one nanoring to center of another nanoring is 400nm. Black curve: reflectance spectrum when the nanorings are fabricated on flat glass substrate and then covered by approximately 300 nm of SiO_2 sol-gel so as to symmetrize the system. Red curve: reflectance when the same nanorings are fabricated on a mesoporous TiO_2 layer. Blue curve: reflection of these nanorings when they were covered by an extra layer of mesoporous TiO_2.

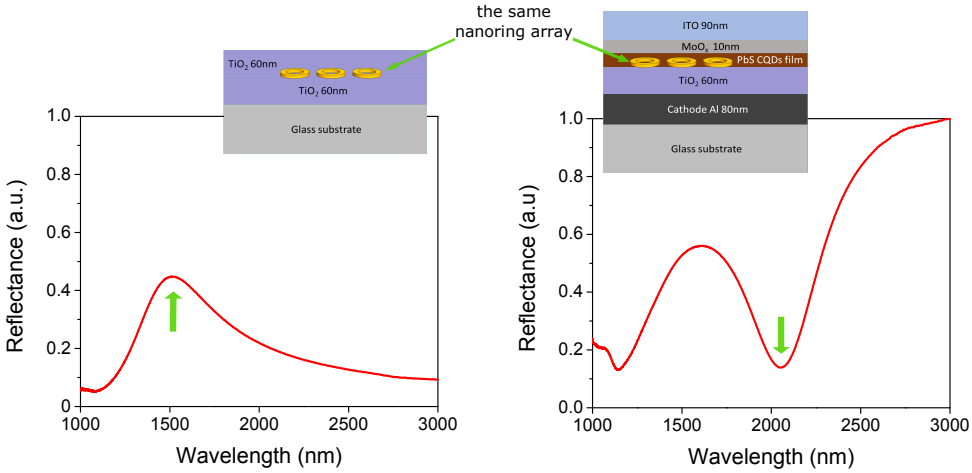

Figure E.2: Response of the same Al nanoring arrays embedded in mesoporous TiO_2 (left) and embedded in the full QDLED structure (right).

resonance, light is resonantly scattered, resulting in a maximum in reflection. The right graph of Figure E.2 shows the reflectance spectrum of the same nanorings but embedded in

a full architecture of the QDLED. The presence of the underlying metallic plane transforms the reflection maximum into a reflection minimum at the plasmonic resonance frequency. It also strongly shifts the resonance frequency to the red (indicated by a green arrow). These changes can be attributed to the interaction of the nanoring resonances with their reflective images due to the metallic planes [200, 201, 202].

Bibliography

[1] Buji Khalifa tower. Dubai, United Arab Emirates. `http://www.skyscrapercenter.com/building/burj-khalifa/3`. Accessed: 2015 Dec 7.

[2] T.C. Harman, P.J. Taylor, M.P. Walsh, and B.E. LaForge. Quantum dot superlattice thermoelectric materials and devices. *Science*, 297(5590):2229, 2002.

[3] Kuei Fang Hsu, Sim Loo, Fu Guo, Wei Chen, Jeffrey S. Dyck, Ctirad Uher, Tim Hogan, E.K. Polychroniadis, and Mercouri G Kanatzidis. Cubic $AgPb_mSbTe_{2+m}$: Bulk Thermoelectric Materials with High Figure of Merit. *Science*, 303(5659):818, 2004.

[4] Mildred S. Dresselhaus, Gang Chen, Ming Y. Tang, R.G. Yang, Hohyun Lee, D.Z. Wang, Z.F. Ren, J.-P. Fleurial, and Pawan Gogna. New directions for low-dimensional thermoelectric materials. *Adv. Mater.*, 19(8):1043, 2007.

[5] Li-Dong Zhao, Shih-Han Lo, Yongsheng Zhang, Hui Sun, Gangjian Tan, Ctirad Uher, Christopher Wolverton, Vinayak P Dravid, and Mercouri G Kanatzidis. Ultralow thermal conductivity and high thermoelectric figure of merit in SnSe crystals. *Nature*, 508(7496):373, 2014.

[6] David R. Smith and Norman Kroll. Negative refractive index in left-handed materials. *Phys. Rev. Lett.*, 85(14):2933, 2000.

[7] Lord Rayleigh. LVI. On the influence of obstacles arranged in rectangular order upon the properties of a medium. *The London, Edinburgh, and Dublin Philosophical Magazine and Journal of Science*, 34(211):481, 1892.

[8] Jagadis Chunder Bose. On the rotation of plane of polarisation of electric waves by a twisted structure. *Proceedings of the Royal Society of London*, 63(389-400):146, 1898.

[9] Winston E. Kock. Metallic delay lenses. *Bell System Technical Journal*, 27(1):58, 1948.

[10] MMZ Kharadly and Willis Jackson. The properties of artificial dielectrics comprising arrays of conducting elements. *Proceedings of the IEE-Part III: Radio and Communication Engineering*, 100(7):199, 1953.

[11] Walter Rotman. Plasma simulation by artificial dielectrics and parallel-plate media. *Antennas and Propagation, IRE Transactions on*, 10(1):82, 1962.

[12] Georg Goubau. Surface waves and their application to transmission lines. *J. Appl. Phys.*, 21(11):1119, 1950.

[13] Sergei Alexander Schelkunoff and Harald T Friis. *Antennas: theory and practice*, volume 639. Wiley New York, 1952.

[14] J.B. Pendry, A.J. Holden, W.J. Stewart, and I. Youngs. Extremely low frequency plasmons in metallic mesostructures. *Phys. Rev. Lett.*, 76(25):4773, 1996.

[15] J.B. Pendry, A.J. Holden, D.J. Robbins, and W.J. Stewart. Low frequency plasmons in thin-wire structures. *J. Phys.: Condens. Matter.*, 10(22):4785, 1998.

[16] John B Pendry, A. J. Holden, D.J. Robbins, and W.J. Stewart. Magnetism from conductors and enhanced nonlinear phenomena. *Microwave Theory and Techniques, IEEE Transactions on*, 47(11):2075, 1999.

[17] Richard A. Shelby, David R. Smith, and Seldon Schultz. Experimental verification of a negative index of refraction. *Science*, 292(5514):77, 2001.

[18] John B. Pendry, David Schurig, and David R. Smith. Controlling electromagnetic fields. *Science*, 312(5781):1780, 2006.

[19] John Brian Pendry. Negative refraction makes a perfect lens. *Phys. Rev. Lett.*, 85 (18):3966, 2000.

[20] Hyesog Lee, Yi Xiong, Nicholas Fang, Werayut Srituravanich, Stephane Durant, Muralidhar Ambati, Cheng Sun, and Xiang Zhang. Realization of optical superlens imaging below the diffraction limit. *New J. Phys.*, 7(1):255, 2005.

[21] Viktor G Veselago. The electrodynamics of substances with simultaneously negative values of ϵ and μ. *Soviet Physics Uspekhi*, 10(4):509, 1968.

[22] J. Kim, Vladimir P. Drachev, Z. Jacob, Gururaj V. Naik, Alexandra Boltasseva, Evgenii E. Narimanov, and Vladimir M. Shalaev. Improving the radiative decay rate for dye molecules with hyperbolic metamaterials. *Opt. Express*, 20(7):8100, 2012.

[23] M. A. Noginov, H. Li, Yu A. Barnakov, D. Dryden, G. Nataraj, G. Zhu, C. E. Bonner, M. Mayy, Z. Jacob, and E. E. Narimanov. Controlling spontaneous emission with metamaterials. *Opt. Lett.*, 35(11):1863, 2010.

[24] Andrea Alù, Mário G. Silveirinha, Alessandro Salandrino, and Nader Engheta. Epsilon-near-zero metamaterials and electromagnetic sources: Tailoring the radiation phase pattern. *Phys. Rev. B.*, 75(15):155410, 2007.

[25] Cristian Della Giovampaola and Nader Engheta. Digital metamaterials. *Nature Mater.*, 13(12):1115, 2014.

[26] Bingnan Wang, Jiangfeng Zhou, Thomas Koschny, Maria Kafesaki, and Costas M Soukoulis. Chiral metamaterials: simulations and experiments. *J. Opt. A: Pure Appl. Opt.*, 11(11):114003, 2009.

[27] Nicholas Fang, Hyesog Lee, Cheng Sun, and Xiang Zhang. Sub–diffraction-limited optical imaging with a silver superlens. *Science*, 308(5721):534, 2005.

[28] Alexandre Archambault, Mondher Besbes, and Jean-Jacques Greffet. Superlens in the time domain. *Phys. Rev. Lett.*, 109(9):097405, 2012.

[29] Ulf Leonhardt. Optical conformal mapping. *Science*, 312(5781):1777, 2006.

[30] T. Bückmann, M. Thiel, M. Kadic, R. Schittny, and M. Wegener. An elasto-mechanical unfeelability cloak made of pentamode metamaterials. *Nature Commun.*, 5:4130, 2014.

[31] Xingjie Ni, Zi Jing Wong, Michael Mrejen, Yuan Wang, and Xiang Zhang. An ultrathin invisibility skin cloak for visible light. *Science*, 349(6254):1310, 2015.

[32] N.I. Landy, S. Sajuyigbe, J.J. Mock, D.R. Smith, and W.J. Padilla. Perfect metamaterial absorber. *Phys. Rev. Lett.*, 100(20):207402, 2008.

[33] Xianliang Liu, Tatiana Starr, Anthony F. Starr, and Willie J. Padilla. Infrared spatial and frequency selective metamaterial with near-unity absorbance. *Phys. Rev. Lett.*, 104(20):207403, 2010.

[34] C. Caloz and T. Itoh. *Electromagnetic Metamaterials: Transmission Line Theory and Microwave Applications*. Wiley, Hoboken, 2006.

[35] Burokur S.N. de Lustrac A. Priou A. Dhouibi, A. Compact metamaterial-based substrate-integrated luneburg lens antenna. *IEEE Antenn. Wireless Propag. Lett.*, 11:1504, 2012.

[36] Costas M. Soukoulis and Martin Wegener. Past achievements and future challenges in the development of three-dimensional photonic metamaterials. *Nature Photon.*, 5:523, 2011.

[37] Jason Valentine, Shuang Zhang, Thomas Zentgraf, Erick Ulin-Avila, Dentcho A. Genov, Guy Bartal, and Xiang Zhang. Three-dimensional optical metamaterial with a negative refractive index. *Nature*, 455(7211):376, 2008.

[38] Na Liu, Hongcang Guo, Liwei Fu, Stefan Kaiser, Heinz Schweizer, and Harald Giessen. Three-dimensional photonic metamaterials at optical frequencies. *Nature Mater.*, 7(1):31, 2008.

[39] N. Yu, P. Genevet, M. A. Kats, F. Aieta, J. P. Tetienne, F. Capasso, and Z. Gaburro. Light propagation with phase discontinuities: generalized laws of reflection and refraction. *Science*, 334(6054):333, 2011.

[40] A. Hinke Schokker and A. Femius Koenderink. Lasing at the band edges of plasmonic lattices. *Phys. Rev. B.*, 90(15):155452, 2014.

[41] Lingling Huang, Xianzhong Chen, Holger Mü hlenbernd, Hao Zhang, Shumei Chen, Benfeng Bai, Qiaofeng Tan, Guofan Jin, Kok-Wai Cheah, Cheng-Wei Qiu, Li Jensen, Thomas Zentgraf, and Shuang Zhang. Three-dimensional optical holography using a plasmonic metasurface. *Nature Commun.*, 4:2808, 2013.

[42] Y. Zhou, X.Y. Chen, Y.H. Fu, G. Vienne, A.I. Kuznetsov, and B. Luk'yanchuk. Fabrication of large-area 3D optical fishnet metamaterial by laser interference lithography. *Appl. Phys. Lett.*, 103(12):123116, 2013.

[43] Debashis Chanda, Kazuki Shigeta, Sidhartha Gupta, Tyler Cain, Andrew Carlson, Agustin Mihi, Alfred J Baca, Gregory R Bogart, Paul Braun, and John A Rogers. Large-area flexible 3D optical negative index metamaterial formed by nanotransfer printing. *Nature Nanotech.*, 6(7):402, 2011.

[44] Justyna K. Gansel, Michael Thiel, Michael S. Rill, Manuel Decker, Klaus Bade, Volker Saile, Georg von Freymann, Stefan Linden, and Martin Wegener. Gold helix photonic metamaterial as broadband circular polarizer. *Science*, 325(5947):1513, 2009.

[45] Silvia Vignolini, Nataliya A Yufa, Pedro S Cunha, Stefan Guldin, Ilia Rushkin, Morgan Stefik, Kahyun Hur, Ulrich Wiesner, Jeremy J Baumberg, and Ullrich Steiner. A 3D optical metamaterial made by self-assembly. *Adv. Mater.*, 24(10):OP23, 2012.

[46] Nina Meinzer, William L. Barnes, and Ian R. Hooper. Plasmonic meta-atoms and metasurfaces. *Nature Photon.*, 8(12):889, 2014.

[47] Reuben M. Bakker, Vladimir P. Drachev, Zhengtong Liu, Hsiao-Kuan Yuan, Rasmus H Pedersen, Alexandra Boltasseva, Jiji Chen, Joseph Irudayaraj, Alexander V. Kildishev, and Vladimir M. Shalaev. Nanoantenna array-induced fluorescence enhancement and reduced lifetimes. *New J. Phys.*, 10:125022, 2008.

[48] K. Tanaka, E. Plum, J. Y. Ou, T. Uchino, and N. I. Zheludev. Multifold Enhancement of Quantum Dot Luminescence in Plasmonic Metamaterials. *Phys. Rev. Lett.*, 105(22):227403, 2010.

[49] Jean-Jacques Grefffet. Nanoantennas for Light Emission. *Science*, 308(5728):1561, 2005.

[50] Lukas Novotny and Niek van Hulst. Antennas for light. *Nature Photon.*, 5(2):83, 2011.

[51] William L. Barnes, Alain Dereux, and Thomas W. Ebbesen. Surface plasmon subwavelength optics. *Nature*, 424(6950):824, 2003.

[52] Cherif Belacel, Benjamin Habert, Florian Bigourdan, François Marquier, J-P Hugonin, S Michaelis de Vasconcellos, Xavier Lafosse, Laurent Coolen, Catherine Schwob, Clémentine Javaux, Jean-Jacques Greffet, and Agnés Maitre. Controlling Spontaneous Emission with Plasmonic Optical Patch Antennas. *Nano Lett.*, 13(4):1516, 2013.

[53] Thang B. Hoang, Gleb M. Akselrod, Christos Argyropoulos, Jiani Huang, David R. Smith, and Maiken H. Mikkelsen. Ultrafast spontaneous emission source using plasmonic nanoantennas. *Nature Commun.*, 6:7788, 2015.

[54] Edward Mills Purcell. Spontaneous emission probabilities at radio frequencies. *Phys. Rev.*, 69:681, 1946.

[55] Konstantin Y. Bliokh, Yury P. Bliokh, Valentin Freilikher, Sergey Savelev, and Franco Nori. Colloquium: Unusual resonators: Plasmonics, metamaterials, and random media. *Rev. Mod. Phys.*, 80(4):1201, 2008.

[56] Kerry J. Vahala. Optical microcavities. *Nature*, 424(6950):839, 2003.

[57] Matthew Pelton. Modified spontaneous emission in nanophotonic structures. *Nature Photon.*, 9(7):427, 2015.

[58] A. G. Curto, G. Volpe, T. H. Taminiau, M. P. Kreuzer, R. Quidant, and N. F. van Hulst. Unidirectional emission of a quantum dot coupled to a nanoantenna. *Science*, 329(5994):930, 2010.

[59] T. V. Teperik and A. Degiron. Numerical analysis of an optical toroidal antenna coupled to a dipolar emitter. *Phys. Rev. B.*, 83(24):245408, 2011.

[60] Heykel Aouani, Oussama Mahboub, Eloise Devaux, Herve Rigneault, Thomas W. Ebbesen, and Jerome Wenger. Plasmonic antennas for directional sorting of fluorescence emission. *Nano Lett.*, 11(6):2400, 2011.

[61] Young Chul Jun, Kevin CY Huang, and Mark L. Brongersma. Plasmonic beaming and active control over fluorescent emission. *Nature Commun.*, 2:283, 2011.

[62] Heykel Aouani, Oussama Mahboub, Nicolas Bonod, Eloïse Devaux, Evgeny Popov, Hervé Rigneault, Thomas W Ebbesen, and Jérôme Wenger. Bright Unidirectional Fluorescence Emission of Molecules in a Nanoaperture with Plasmonic Corrugations. *Nano Lett.*, 11(2):637, 2011.

[63] J. Kümmerlen, A. Leitner, H. Brunner, F.R. Aussenegg, and A. Wokaun. Enhanced dye fluorescence over silver island films: analysis of the distance dependence. *Mol. Phys.*, 80(5):1031, 1993.

[64] Sergei Kühn, Ulf Håkanson, Lavinia Rogobete, and Vahid Sandoghdar. Enhancement of single-molecule fluorescence using a gold nanoparticle as an optical nanoantenna. *Phys. Rev. Lett.*, 97(1):017402, 2006.

[65] Anika Kinkhabwala, Zongfu Yu, Shanhui Fan, Yuri Avlasevich, Klaus Mullen, and W. E. Moerner. Large single-molecule fluorescence enhancements produced by a bowtie nanoantenna. *Nature Photon.*, 3(11):654, 2009.

[66] Daniel Dregely, Klas Lindfors, Jens Dorfmüller, Mario Hentschel, Merle Becker, Jörg Wrachtrup, Markus Lippitz, Ralf Vogelgesang, and Harald Giessen. Plasmonic antennas, positioning, and coupling of individual quantum systems. *Phys. Status Solidi B*, 249(4):666, 2012.

[67] Palash Bharadwaj, Bradley Deutsch, and Lukas Novotny. Optical antennas. *Adv. Opt. Photon.*, 1(3):438, 2009.

[68] Johannes Kern, René Kullock, Jord Prangsma, Monika Emmerling, Martin Kamp, and Bert Hecht. Electrically driven optical antennas. *Nature Photon.*, 9(9):582, 2015.

[69] Mickael Buret, Alexander V. Uskov, Jean Dellinger, Nicolas Cazier, Marie-Maxime Mennemanteuil, Johann Berthelot, Igor V. Smetanin, Igor E. Protsenko, Gérard Colas-des Francs, and Alexandre Bouhelier. Spontaneous hot-electron light emission from electron-fed optical antennas. *Nano Lett.*, 15(9):5811, 2015.

[70] O. Hess, J. B. Pendry, S. A. Maier, R. F. Oulton, J. M. Hamm, and K. L. Tsakmakidis. Active nanoplasmonic metamaterials. *Nature Mater.*, 11(7):573, 2012.

[71] V. V. Golubkov, A. A. Onuchenko, A. I. Ekimov, and V. A. Chekomskii. *Sov. Physics and Chemmistry of Glass*, 6:12, 1980.

[72] A. Henglein. Photo-Degradation and Fluorescence of Colloidal-Cadmium Sulfide in Aqueous Solution. *Berichte der Bunsengesellschaft für physikalische Chemie*, 86: 301, 1982.

[73] LE Brus. A simple model for the ionization potential, electron affinity, and aqueous redox potentials of small semiconductor crystallites. *J. Chem. Phys.*, 79(11):5566, 1983.

[74] Al L. Efros and M. Rosen. The electronic structure of semiconductor nanocrystals. *Annu. Rev. Mater. Sci.*, 30:475, 2000.

[75] Joshua Jongwoo Choi. *Nanocrystal quantum dots as building blocks for artificial solids and their Applications in optoelectronic devices*. PhD thesis, Cornell University, 2012.

[76] Frank W. Wise. Lead Salt Quantum Dots: the Limit of Strong Quantum Confinement. *Acc. Chem. Res.*, 33(11):773, 2000.

[77] Ludovico Cademartiri, Erica Montanari, Gianluca Calestani, Andrea Migliori, Antonietta Guagliardi, and Geoffrey A. Ozin. Size-dependent extinction coefficients of PbS quantum dots. *J. Am. Chem. Soc.*, 128(31):10337, 2006.

[78] N.F. Borrelli and D.W. Smith. Quantum confinement of PbS microcrystals in glass. *J. Non-Cryst. Solids.*, 180(1):25, 1994.

[79] R.S. Kane, R.E. Cohen, and R. Silbey. Theoretical Study of the Electronic Structure of PbS Nanoclusters. *J. Phys. Chem.*, 100(19):7928, 1996.

[80] Iwan Moreels, Karel Lambert, Dries Smeets, David De Muynck, Tom Nollet, José C. Martins, Frank Vanhaecke, André Vantomme, Christophe Delerue, Guy Allan, and Zeger Hens. Size-Dependent Optical Properties of Colloidal PbS Quantum Dots. *ACS Nano*, 3(10):3023, 2009.

[81] Margaret A Hines and Gregory D Scholes. Colloidal PbS nanocrystals with size-tunable near-infrared emission: observation of post-synthesis self-narrowing of the particle size distribution. *Adv. Mater.*, 15(21):1844, 2003.

[82] Laurent Coolen, Piernicola Spinicelli, and J-P Hermier. Emission spectrum and spectral diffusion of a single CdSe/ZnS nanocrystal measured by photon-correlation fourier spectroscopy. *JOSA B*, 26(7):1463, 2009.

[83] Jian Cui, Andrew P. Beyler, Lisa F. Marshall, Ou Chen, Daniel K. Harris, Darcy D. Wanger, Xavier Brokmann, and Moungi G. Bawendi. Direct probe of spectral inhomogeneity reveals synthetic tunability of single-nanocrystal spectral linewidths. *Nature Chem.*, 5(7):602, 2013.

[84] Xiaoyong Wang, Xiaofan Ren, Keith Kahen, Megan A. Hahn, Manju Rajeswaran, Sara Maccagnano-Zacher, John Silcox, George E Cragg, Alexander L. Efros, and Todd D Krauss. Non-blinking semiconductor nanocrystals. *Nature*, 459(7247):686, 2009.

[85] Jamie H. Warner, Elizabeth Thomsen, Andrew R. Watt, Norman R Heckenberg, and Halina Rubinsztein-Dunlop. Time-resolved photoluminescence spectroscopy of ligand-capped PbS nanocrystals. *Nanotechnology*, 16(2):175, 2005.

[86] S. F. Lee and M. A. Osborne. Brightening, blinking, bluing and bleaching in the life of a quantum dot: friend or foe? *Chemphyschem.*, 10(13):2174, 2009.

[87] Botao Ji, Emerson Giovanelli, Benjamin Habert, Piernicola Spinicelli, Michel Nasilowski, Xiangzhen Xu, Nicolas Lequeux, Jean-Paul Hugonin, Francois Marquier, Jean-Jacques Greffet, and Benoit Dubertret. Non-blinking quantum dot with a plasmonic nanoshell resonator. *Nature Nanotech.*, 10(2):170, 2015.

[88] J. Warnock and D.D. Awschalom. Quantum size effects in simple colored glass. *Phys. Rev. B.*, 32(8):5529, 1985.

[89] A. Ekimov. Growth and optical properties of semiconductor nanocrystals in a glass matrix. *J. Lumin.*, 70(1-6):1, 1996.

[90] L. Goldstein, F. Glas, J.Y. Marzin, M.N. Charasse, and G. Le Roux. Growth by molecular beam epitaxy and characterization of InAs/GaAs strained-layer superlattices. *Appl. Phys. Lett.*, 47(10):1099, 1985.

[91] D. Leonard, M. Krishnamurthy, C.M. Reaves, S.P. Denbaars, and P.M. Petroff. Direct formation of quantum-sized dots from uniform coherent islands of InGaAs on GaAs surfaces. *Appl. Phys. Lett.*, 63(23):3203, 1993.

[92] J.M. Moison, F. Houzay, F. Barthe, L. Leprince, E. Andre, and O. Vatel. Self-organized growth of regular nanometer-scale InAs dots on GaAs. *Appl. Phys. Lett.*, 64(2):196, 1994.

[93] Maria Ibáñez, Reza Zamani, Stéphane Gorsse, Jiandong Fan, Silvia Ortega, Doris Cadavid, Joan Ramon Morante, Jordi Arbiol, and Andreu Cabot. Core-Shell Nanoparticles As Building Blocks for the Bottom-Up Production of Functional Nanocomposites: PbTe–PbS Thermoelectric Properties. *ACS Nano*, 7(3):2573, 2013.

[94] Marcel Bruchez, Mario Moronne, Peter Gin, Shimon Weiss, and A. Paul Alivisatos. Semiconductor nanocrystals as fluorescent biological labels. *Science*, 281(5385): 2013, 1998.

[95] R. Rossetti, J.L. Ellison, J.M. Gibson, and LE Brus. Size effects in the excited electronic states of small colloidal CdS crystallites. *J. Chem. Phys.*, 80(9):4464, 1984.

[96] M.T. Nenadovic, T. Rajh, and O.I. Micic. Size quantization in small semiconductor particles. *J. Chem. Phys.*, 89(3):397, 1985.

[97] M.G. Bawendi, A.R. Kortan, M.L. Steigerwald, and LE Brus. X-ray structural characterization of larger CdSe semiconductor clusters. *J. Chem. Phys.*, 91(11): 7282, 1989.

[98] Wenhao Liu, Mark Howarth, Andrew B. Greytak, Yi Zheng, Daniel G Nocera, Alice Y. Ting, and Moungi G. Bawendi. Compact biocompatible quantum dots functionalized for cellular imaging. *J. Am. Chem. Soc.*, 130(4):1274, 2008.

[99] Peter M. Allen, Wenhao Liu, Vikash P Chauhan, Jungmin Lee, Alice Y Ting, Dai Fukumura, Rakesh K Jain, and Moungi G. Bawendi. InAs(ZnCdS) quantum dots optimized for biological imaging in the near-infrared. *J. Am. Chem. Soc.*, 132(2): 470, 2009.

[100] Adriana Fontes and Beate Saegesser Santos. *Quantum Dots: Applications in Biology.* Springer, 2014.

[101] Ute Resch-Genger, Markus Grabolle, Sara Cavaliere-Jaricot, Roland Nitschke, and Thomas Nann. Quantum dots versus organic dyes as fluorescent labels. *Nat. Methods.*, 5(9):763, 2008.

[102] Andrew M. Smith, Michael C. Mancini, and Shuming Nie. Bioimaging: second window for in vivo imaging. *Nature Nanotech.*, 4(11):710, 2009.

[103] Marek F. Oszajca, Maryna I. Bodnarchuk, and Maksym V. Kovalenko. Precisely Engineered Colloidal Nanoparticles and Nanocrystals for Li-Ion and Na-Ion Batteries: Model Systems or Practical Solutions? *Chem. Mater.*, 26(19):5422, 2014.

[104] Soo Hong Lee, Seung-Ho Yu, Ji Eun Lee, Aihua Jin, Dong Jun Lee, Nohyun Lee, Hyungyung Jo, Kwangsoo Shin, Tae-Young Ahn, Young-Woon Kim, Heeman Choe, Yung-Eun Sung, and Taeghwan Hyeon. Self-assembled Fe_3O_4 Nanoparticle Clusters as High-Performance Anodes for Lithium Ion Batteries via Geometric Confinement. *Nano Lett.*, 13(9):4249, 2013.

[105] Kostiantyn Kravchyk, Loredana Protesescu, Maryna I Bodnarchuk, Frank Krumeich, Maksym Yarema, Marc Walter, Christoph Guntlin, and Maksym V Kovalenko. Monodisperse and inorganically capped Sn and Sn/SnO_2 nanocrystals for high-performance Li-ion battery anodes. *J. Am. Chem. Soc.*, 135(11):4199, 2013.

[106] J. M. Caruge, J. E. Halpert, V. Wood, V. Bulović, and M. G. Bawendi. Colloidal quantum-dot light-emitting diodes with metal-oxide charge transport layers. *Nature Photon.*, 2(4):247, 2008.

[107] Tae-Ho Kim, Kyung-Sang Cho, Eun Kyung Lee, Sang Jin Lee, Jungseok Chae, Jung Woo Kim, Do Hwan Kim, Jang-Yeon Kwon, Gehan Amaratunga, Sang Yoon Lee, Byoung Lyong Choi, Young Kuk, Jong Min Kim, and Kinam Kim. Full-colour quantum dot displays fabricated by transfer printing. *Nature Photon.*, 5(3):176, 2011.

[108] Xingliang Dai, Zhenxing Zhang, Yizheng Jin, Yuan Niu, Hujia Cao, Xiaoyong Liang, Liwei Chen, Jianpu Wang, and Xiaogang Peng. Solution-processed, high-performance light-emitting diodes based on quantum dots. *Nature*, 515(7525):96, 2014.

[109] Yixing Yang, Ying Zheng, Weiran Cao, Alexandre Titov, Jake Hyvonen, Jesse R Manders, Jiangeng Xue, Paul H Holloway, and Lei Qian. High-efficiency light-emitting devices based on quantum dots with tailored nanostructures. *Nature Photon.*, 9(4):259, 2015.

[110] Gerasimos Konstantatos, Ian Howard, Armin Fischer, Sjoerd Hoogland, Jason Clifford, Ethan Klem, Larissa Levina, and Edward H. Sargent. Ultrasensitive solution-cast quantum dot photodetectors. *Nature*, 442(7099):180, 2006.

[111] Tobias Rauch, Michaela Boberl, Sandro F. Tedde, Jens Furst, Maksym V. Kovalenko, Gunter Hesser, Uli Lemmer, Wolfgang Heiss, and Oliver Hayden. Near-infrared imaging with quantum-dot-sensitized organic photodiodes. *Nature Photon.*, 3(6):332, 2009.

[112] Gerasimos Konstantatos, Michela Badioli, Louis Gaudreau, Johann Osmond, Maria Bernechea, F. Pelayo Garcia de Arquer, Fabio Gatti, and Frank H.L. Koppens. Hybrid graphene-quantum dot phototransistors with ultrahigh gain. *Nature Nanotech.*, 7:363, 2012.

[113] Gerasimos Konstantatos and Edward H. Sargent. *Colloidal quantum dot optoelectronics and photovoltaics*. Cambridge University Press, 2013.

[114] Steven A. Mcdonald, Gerasimos Konstantatos, Shiguo Zhang, Paul W. Cyr, Ethan J.D. Klem, Larissa Levina, and Edward H. Sargent. Solution-processed PbS quantum dot infrared photodetectors and photovoltaics. *Nature Mater.*, 4(2):138, 2005.

[115] Andras G. Pattantyus-Abraham, Illan J. Kramer, Aaron R. Barkhouse, Xihua Wang, Gerasimos Konstantatos, Ratan Debnath, Larissa Levina, Ines Raabe, Mohammad K. Nazeeruddin, Michael Grä tzel, and Edward H. Sargent. Depleted-Heterojunction Colloidal Quantum Dot Solar Cells. *ACS Nano*, 4(6):3374, 2010.

[116] Zhenyu Yang, Alyf Janmohamed, Xinzheng Lan, F. Pelayo Garcia de Arquer, Oleksandr Voznyy, Emre Yassitepe, Gi-Hwan Kim, Zhijun Ning, Xiwen Gong, Riccardo Comin, and Edward H. Sargent. Colloidal Quantum Dot Photovoltaics Enhanced by Perovskite Shelling. *Nano Lett.*, 15(11):7539, 2015.

[117] Patrick R. Brown, Donghun Kim, Richard R. Lunt, Ni Zhao, Moungi G. Bawendi, Jeffrey C. Grossman, and Vladimir Bulović. Energy Level Modification in Lead Sulfide Quantum Dot Thin Films through Ligand Exchange. *ACS Nano*, 8(6):5863, 2014.

[118] Jeonghun Kwak, Wan Ki Bae, Donggu Lee, Insun Park, Jaehoon Lim, Myeongjin Park, Hyunduck Cho, Heeje Woo, Do Y. Yoon, Kookheon Char, Seonghoon Lee, and Changhee Lee. Bright and Efficient Full-Color Colloidal Quantum Dot Light-Emitting Diodes Using an Inverted Device Structure. *Nano Lett.*, 12(5):2362, 2012.

[119] Randy J. Ellingson, Matthew C. Beard, Justin C. Johnson, Pingrong Yu, Olga I. Micic, Arthur J. Nozik, Andrew Shabaev, and Alexander L. Efros. Highly Efficient Multiple Exciton Generation in Colloidal PbSe and PbS Quantum Dots. *Nano Lett.*, 5(5):865, 2005.

[120] Xavier Brokmann, Laurent Coolen, Jean-Pierre Hermier, and Maxime Dahan. Emission properties of single CdSe/ZnS quantum dots close to a dielectric interface. *Chem. Phys.*, 318(1-2):91, 2005.

[121] S. Dembski, C. Graf, T. Kruger, U. Gbureck, A. Ewald, A. Bock, and E. Ruhl. Photoactivation of CdSe/ZnS quantum dots embedded in silica colloids. *Small*, 4 (9):1516, 2008.

[122] Vasudevanpillai Biju, Ryodai Kanemoto, Yuusuke Matsumoto, Sayaka Ishii, Shunsuke Nakanishi, Tamitake Itoh, Yoshinobu Baba, and Mitsuru Ishikawa. Photoinduced Photoluminescence Variations of CdSe Quantum Dots in Polymer Solutions. *J. Phys. Chem. C.*, 111(22):7924, 2007.

[123] Jan W. Stouwdam, Jingning Shan, Frank C. J. M. van Veggel, Andras G. Pattantyus-Abraham, Jeff F. Young, and Mati Raudsepp. Photostability of Colloidal PbSe and PbSe/PbS Core/Shell Nanocrystals in Solution and in the Solid State. *J. Phys. Chem. C.*, 111:1086, 2006.

[124] R. D. Schaller, M. A. Petruska, and V. I. Klimov. Tunable Near-Infrared Optical Gain and Amplified Spontaneous Emission Using PbSe Nanocrystals. *J. Phys. Chem. B.*, 107(50):13765, 2003.

[125] V. Sukhovatkin, S. Musikhin, I. Gorelikov, S. Cauchi, L. Bakueva, E. Kumacheva, and E. H. Sargent. Room-temperature amplified spontaneous emission at 1300 nm in solution-processed PbS quantum-dot films. *Opt. Lett.*, 30(2):171, 2005.

[126] Lukas Novotny and Bert Hecht. *Principles of Nano-Optics*. Cambridge University Press, New York, 2006.

[127] K. P. O'Donnell and X. Chen. Temperature dependence of semiconductor band gaps. *Appl. Phys. Lett.*, 58(25):2924, 1991.

[128] S. A. Crooker, T. Barrick, J. A. Hollingsworth, and V. I. Klimov. Multiple temperature regimes of radiative decay in CdSe nanocrystal quantum dots: Intrinsic limits to the dark-exciton lifetime. *Appl. Phys. Lett.*, 82(17):2793, 2003.

[129] M. Henini B. Hennequin L. Turyanska, A. Patanè and N. R. Thomas. Temperature dependence of the photoluminescence emission from thiol-capped PbS quantum dots. *Appl. Phys. Lett.*, 90(10):101913, 2007.

[130] Andrey A. Tolstik Nikolai A. Onushchenko Alexei A. Malyarevich Alexander M. Petrov Eugene P. Yumashev Konstantin V. Gaponenko, Maxim S. Lutich. Temperature-dependent photoluminescence of PbS quantum dots in glass: Evidence of exciton state splitting and carrier trapping. *Phys. Rev. B.*, 82(12):125320, 2010.

[131] Chizuko M. Dutta, Tamer A. Ali, Daniel W. Brandl, Tae-Ho Park, and Peter Nordlander. Plasmonic properties of a metallic torus. *J. Chem. Phys.*, 129(8):084706, 2008.

[132] A. Mary, D. M. Koller, A. Hohenau, J.J. R. Krenn, Bouhelier A., and Dereux A. Optical absorption of torus-shaped metal nanoparticles in the visible range. *Phys. Rev. B.*, 76(24):245422, 2007.

[133] J. Aizpurua, P. Hanarp, D. Sutherland, M. Käll, Garnett Bryant, and F. García de Abajo. Optical Properties of Gold Nanorings. *Phys. Rev. Lett.*, 90(5):057401, 2003.

[134] T. V. Teperik and A. Degiron. Design strategies to tailor the narrow plasmon-photonic resonances in arrays of metallic nanoparticles. *Phys. Rev. B.*, 86(24): 245425, 2012.

[135] T. V. Teperik and A. Degiron. Superradiant optical emitters coupled to an array of nanosize metallic antennas. *Phys. Rev. Lett.*, 108(14):147401, 2012.

[136] Rodney Loudon. *The quantum theory of light*. Oxford University Press, third edition, 2000.

[137] J. Azoulay, A. Débarre, A. Richard, and P. Tchénio. Quenching and enhancement of single-molecule fluorescence under metallic and dielectric tips. *Europhys. Lett.*, 51(4):374, 2000.

[138] LinLin Zhao, K. Lance Kelly, and George C. Schatz. The Extinction Spectra of Silver Nanoparticle Arrays: Influence of Array Structure on Plasmon Resonance Wavelength and Width. *J. Phys. Chem. B.*, 107(30):7343, 2003.

[139] M. Ringler, A. Schwemer, M. Wunderlich, A. Nichtl, K. Kü rzinger, T. A. Klar, and J. Feldmann. Shaping Emission Spectra of Fluorescent Molecules with Single Plasmonic Nanoresonators. *Phys. Rev. Lett.*, 100(20):203002, 2008.

[140] Jean-Sebastien G. Bouillard, Wayne Dickson, Daniel P. O′Connor, Gregory A. Wurtz, and Anatoly V. Zayats. Low-temperature plasmonics of metallic nanostructures. *Nano Lett.*, 12(3):1561, 2012.

[141] V.L. Colvin, M.C. Schlamp, and A.P. Alivisatos. Light-emitting diodes made from cadmium selenide nanocrystals and a semiconducting polymer. *Nature*, 370(6488): 354, 1994.

[142] B.O. Dabbousi, M.G. Bawendi, O. Onitsuka, and M.F. Rubner. Electroluminescence from CdSe quantum-dot/polymer composites. *Appl. Phys. Lett.*, 66(11):1316, 1995.

[143] Ching W. Tang and S. A. VanSlyke. Organic electroluminescent diodes. *Appl. Phys. Lett.*, 51(12):913, 1987.

[144] Seth Coe, Wing-Keung Woo, Moungi Bawendi, and Vladimir Bulović. Electroluminescence from single monolayers of nanocrystals in molecular organic devices. *Nature*, 420(6917):800, 2002.

[145] Kwon-Hyeon Kim, Sunghun Lee, Chang-Ki Moon, Sei-Yong Kim, Young-Seo Park, Jeong-Hwan Lee, Jin Woo Lee, June Huh, Youngmin You, and Jang-Joo Kim. Phosphorescent dye-based supramolecules for high-efficiency organic light-emitting diodes. *Nature Commun.*, 5:4769, 2014.

[146] Andrey L. Rogach, Nikolai Gaponik, John M Lupton, Cristina Bertoni, Diego E. Gallardo, Steve Dunn, Nello Li Pira, Marzia Paderi, Piermario Repetto, Sergei G. Romanov, Colm O′Dwyer, M. Sotomayor Clivia Torres, and Alexander Eychmüller. Light-emitting diodes with semiconductor nanocrystals. *Angew. Chem. Int. Ed.*, 47 (35):6538, 2008.

[147] Vanessa Wood and Vladimir Bulović. Colloidal quantum dot light-emitting devices. *Nano Reviews*, 1:5202, 2010.

[148] Yasuhiro Shirasaki, Geoffrey J. Supran, Moungi G. Bawendi, and Vladimir Bulovic. Emergence of colloidal quantum-dot light-emitting technologies. *Nature Photon.*, 7 (1):13, 2013.

[149] Xuyong Yang, Evren Mutlugun, Cuong Dang, Kapil Dev, Yuan Gao, Swee Tiam Tan, Xiao Wei Sun, and Hilmi Volkan Demir. Highly Flexible, Electrically Driven, Top-Emitting, Quantum Dot Light-Emitting Stickers. *ACS Nano*, 8(8):8224, 2014.

[150] Geoffrey J. Supran, Katherine W. Song, Gyu Weon Hwang, Raoul E. Correa, Jennifer Scherer, Eric A. Dauler, Yasuhiro Shirasaki, Moungi G. Bawendi, and Vladimir Bulović. High-Performance Shortwave-Infrared Light-Emitting Devices Using Core-Shell (PbS-CdS) Colloidal Quantum Dots. *Adv. Mater.*, 27(8):1437, 2015.

[151] C.B. Murray, David J. Norris, and Moungi G. Bawendi. Synthesis and characterization of nearly monodisperse CdE (E= sulfur, selenium, tellurium) semiconductor nanocrystallites. *J. Am. Chem. Soc.*, 115(19):8706, 1993.

[152] Ludovico Cademartiri, Jacopo Bertolotti, Riccardo Sapienza, Diederik S Wiersma, Georg von Freymann, and Geoffrey A Ozin. Multigram scale, solventless, and diffusion-controlled route to highly monodisperse PbS nanocrystals. *J. Phys. Chem. B.*, 110(2):671, 2006.

[153] Yasuhiro Shirasaki, Geoffrey J. Supran, William A. Tisdale, and Vladimir Bulović. Origin of efficiency roll-off in colloidal quantum-dot light-emitting diodes. *Phys. Rev. Lett.*, 110(21):217403, 2013.

[154] Yajie Dong, Jean-Michel Caruge, Zhaoqun Zhou, Charles Hamilton, Zoran Popovic, John Ho, Matthew Stevenson, Guo Liu, Vladimir Bulović, Peter T. Kazlas Jonathan Steckel Bawendi, Moungi, and Seth Coe-Sullivan. 20.2: Ultra-Bright, Highly Efficient, Low Roll-Off Inverted Quantum-Dot Light Emitting Devices (QLEDs). In *SID Symposium Digest of Technical Papers*, volume 46, page 270. Wiley Online Library, 2015.

[155] Liangfeng Sun, Joshua J. Choi, David Stachnik, Adam C. Bartnik, Byung-Ryool Hyun, George G. Malliaras, Tobias Hanrath, and Frank W. Wise. Bright infrared quantum-dot light-emitting diodes through inter-dot spacing control. *Nature Nanotech.*, 7(6):369, 2012.

[156] Kuo-Ju Chen, Hsin-Chu Chen, Kai-An Tsai, Chien-Chung Lin, Hsin-Han Tsai, Shih-Hsuan Chien, Bo-Siao Cheng, Yung-Jung Hsu, Min-Hsiung Shih, Chih-Hao Tsai, His-Hsin Shih, and Hao-Chung Kuo. Resonant-Enhanced Full-Color Emission of Quantum-Dot-Based Display Technology Using a Pulsed Spray Method. *Adv. Funct. Mater.*, 22(24):5138, 2012.

[157] Illan J Kramer, James C Minor, Gabriel Moreno-Bautista, Lisa Rollny, Pongsakorn Kanjanaboos, Damir Kopilovic, Susanna M Thon, Graham H Carey, Kang Wei Chou, David Zhitomirsky, Aram Amassian, and Edward H. Sargent. Efficient Spray-Coated Colloidal Quantum Dot Solar Cells. *Adv. Mater.*, 27(1):116, 2015.

[158] Hanna M. Haverinen, Risto A. Myllylä, and Ghassan E. Jabbour. Inkjet printing of light emitting quantum dots. *Appl. Phys. Lett.*, 94(7):073108, 2009.

[159] Bong Hoon Kim, Serdar M. Onses, Jong Bin Lim, Sooji Nam, Nuri Oh, Hojun Kim, Ki Jun Yu, Jung Woo Lee, Jae-Hwan Kim, Seung-Kyun Kang, Chi Hwan Lee, Jungyup Lee, Jae Ho Shin, Nam Heon Kim, Cecilia Leal, Moonsub Shim, and John A. Rogers. High-Resolution Patterns of Quantum Dots Formed by Electrohydrodynamic Jet Printing for Light-Emitting Diodes. *Nano Lett.*, 15(2):969, 2015.

[160] Matthew P. Genovese, Ian V. Lightcap, and Prashant V. Kamat. Sun-Believable Solar Paint. A Transformative One-Step Approach for Designing Nanocrystalline Solar Cells. *ACS Nano*, 6(1):865, 2011.

[161] Jiang Tang, Kyle W Kemp, Sjoerd Hoogland, Kwang S Jeong, Huan Liu, Larissa Levina, Melissa Furukawa, Xihua Wang, Ratan Debnath, Dongkyu Cha, Kang Wei

Chou, Armin Fischer, Aram Amassian, John B. Asbury, and Edward H. Sargent. Colloidal-quantum-dot photovoltaics using atomic-ligand passivation. *Nature Mater.*, 10(10):765, 2011.

[162] Alexander H. Ip, Susanna M. Thon, Sjoerd Hoogland, Oleksandr Voznyy, David Zhitomirsky, Ratan Debnath, Larissa Levina, Lisa R. Rollny, Graham H. Carey, Armin Fischer, Kyle W. Kemp, Illan J. Kramer, Zhijun Ning, Andre J. Labelle, Kang Wei Chou, Aram Amassian, and Edward H. Sargent. Hybrid passivated colloidal quantum dot solids. *Nature Nanotech.*, 7(9):577, 2012.

[163] Zhijun Ning, Oleksandr Voznyy, Jun Pan, Sjoerd Hoogland, Valerio Adinolfi, Jixian Xu, Min Li, Ahmad R Kirmani, Jon-Paul Sun, James Minor, Kyle W Kemp, Haopeng Dong, Lisa Rollny, André Lanelle, Graham Carey, Brandon Sutherland, Ian Hill, Aram Amassian, Huan Liu, Jiang Tang, Osman M. Bakr, and Edward H. Sargent. Air-stable n-type colloidal quantum dot solids. *Nature Mater.*, 13(8):822, 2014.

[164] Kyung-Sang Cho, Eun Kyung Lee, Won-Jae Joo, Eunjoo Jang, Tae-Ho Kim, Sang Jin Lee, Soon-Jae Kwon, Jai Yong Han, Byung-Ki Kim, Byoung Lyong Choi, and Jong Min Kim. High-performance crosslinked colloidal quantum-dot light-emitting diodes. *Nature Photon.*, 3(6):341, 2009.

[165] P. O. Anikeeva, C. F. Madigan, J. E. Halpert, M. G. Bawendi, and V. Bulovic. Electronic and excitonic processes in light-emitting devices based on organic materials and colloidal quantum dots. *Phys. Rev. B.*, 78(8):085434, 2008.

[166] Polina Olegovna Anikeeva. *Physical properties and Design of Light-Emitting Devices Based on Organic Materials and Nanoparticles*. PhD thesis, Massachusetts Institute of Technology, 2009.

[167] V. Wood, M.J. Panzer, J.E. Halpert, J-M Caruge, M.G. Bawendi, and V. Bulović. Selection of Metal Oxide Charge Transport Layers for Colloidal Quantum Dot LEDs. *ACS Nano*, 3(11):3581, 2009.

[168] Vanessa Wood, Jonathan E Halpert, Matthew J Panzer, Moungi G Bawendi, and Vladimir Bulović. Alternating Current Driven Electroluminescence from ZnSe/ZnS: Mn/ZnS Nanocrystals. *Nano Lett.*, 9(6):2367, 2009.

[169] Vanessa Wood, Matthew J. Panzer, Deniz Bozyigit, Yasuhiro Shirasaki, Ian Rousseau, Scott Geyer, Moungi G. Bawendi, and Vladimir Bulović. Electroluminescence from Nanoscale Materials via Field-Driven Ionization. *Nano Lett.*, 11(7): 2927, 2011.

[170] L.H. Smith, J.A.E. Wasey, and William L. Barnes. Light outcoupling efficiency of top-emitting organic light-emitting diodes. *Appl. Phys. Lett.*, 84(16):2986, 2004.

[171] Xiaodong Wu, Mustafa H. Chowdhury, Chris D. Geddes, Kadir Aslan, Roman Domszy, Joseph R. Lakowicz, and Arthur J.-M. Yang. Use of surface plasmon-coupled emission for enhancing light transmission through Top-Emitting Organic Light Emitting Diodes. *Thin Solid Films*, 516(8):1977, 2008.

[172] Michael Thomschke, Sebastian Reineke, Björn Lüssem, and Karl Leo. Highly Efficient White Top-Emitting Organic Light-Emitting Diodes Comprising Laminated Microlens Films. *Nano Lett.*, 12(1):424, 2011.

[173] Simone Hofmann, Michael Thomschke, Björn Lüssem, and Karl Leo. Top-emitting organic light-emitting diodes. *Opt. Express*, 19(S6):A1250, 2011.

[174] David R. Lide. *"Electron work function of the element", in CRC Handbook of Chemistry and Physics*. CRC Press, Boca Raton, FL, 2005. Electronic Version.

[175] Artem A. Bakulin, Stefanie Neutzner, Huib J. Bakker, Laurent Ottaviani, Damien Barakel, and Zhuoying Chen. Charge trapping dynamics in PbS colloidal quantum dot photovoltaic devices. *ACS Nano*, 7(10):8771, 2013.

[176] Xin Min, Xavier Orignac, and Rui M Almeida. Striation-free, spin-coated sol-gel optical films. *J. Am. Ceram. Soc.*, 78(8):2254, 1995.

[177] Dunbar P. Birnie. Rational solvent selection strategies to combat striation formation during spin coating of thin films. *J. Mater. Sci.*, 16(4):1145, 2001.

[178] Dunbar P. Birnie III. A model for drying control cosolvent selection for spin-coating uniformity: The thin film limit. *Langmuir*, 29(29):9072, 2013.

[179] S. Kirchmeyer, A. Elschner, K. Reuter, W. Lovenich, and U. Merker. PEDOT: principles and applications of an intrinsically conductive polymer. *CRC, Boca Raton*, 2011.

[180] Minlu Zhang, Irfan, Huanjun Ding, Yongli Gao, and C. W. Tang. Organic schottky barrier photovoltaic cells based on MoO_x/C60. *Appl. Phys. Lett.*, 96(18):183301, 2010.

[181] J. Meyer, A. Shu, M. Kröger, and A. Kahn. Effect of contamination on the electronic structure and hole-injection properties of MoO_3/organic semiconductor interfaces. *Appl. Phys. Lett.*, 96(13):133308, 2010.

[182] Hao Lin, Wei Xia, Hsiang N. Wu, Ching W. Tang, Irfan Irfan, and Yongli Gao. MoO_x as an efficient and stable back contact buffer for thin film cdte solar cells. In *Symposium V - Nanostructured and Advanced Materials for Solar-Cell Manufacturing*, volume 1447 of *MRS Proceedings*. Materials Research Society, 2012.

[183] Steven Chuang, Corsin Battaglia, Angelica Azcatl, Stephen McDonnell, Jeong Seuk Kang, Xingtian Yin, Mahmut Tosun, Rehan Kapadia, Hui Fang, Robert M. Wallace, and Ali Javey. MoS_2 p-Type Transistors and Diodes Enabled by High Work Function MoO_x Contacts. *Nano Lett.*, 14(3):1337, 2014.

[184] T. Sasabayashi, N. Ito, E. Nishimura, M. Kon, P.K. Song, K. Utsumi, A. Kaijo, and Y. Shigesato. Comparative study on structure and internal stress in tin-doped indium oxide and indium-zinc oxide films deposited by RF magnetron sputtering. *Thin Solid Films*, 445(2):219, 2003.

[185] Shahzada Qamar Hussain, Woong-Kyo Oh, ShiHyun Ahn, Anh Huy Tuan Le, Sunbo Kim, Youngseok Lee, and Junsin Yi. RF magnetron sputtered indium tin oxide films with high transmittance and work function for a-Si:H/c-Si heterojunction solar cells. *Vacuum*, 101:18, 2014.

[186] Patrick R. Brown, Richard R. Lunt, Ni Zhao, Timothy P. Osedach, Darcy D. Wanger, Liang-Yi Chang, Moungi G. Bawendi, and Vladimir Bulović. Improved Current Extraction from ZnO/PbS Quantum Dot Heterojunction Photovoltaics Using a MoO_3 Interfacial Layer. *Nano Lett.*, 11(7):2955, 2011.

[187] J.S. Kim, M. Granström, R.H. Friend, N. Johansson, W.R. Salaneck, R. Daik, W.J. Feast, and F. Cacialli. Indium–tin oxide treatments for single-and double-layer polymeric light-emitting diodes: The relation between the anode physical, chemical, and morphological properties and the device performance. *J. Appl. Phys.*, 84(12): 6859, 1998.

[188] X. M. Ding, L. M. Hung, L. F. Cheng, Z. B. Deng, X. Y. Hou, C. S. Lee, and S. T. Lee. Modification of the hole injection barrier in organic light-emitting devices studied by ultraviolet photoelectron spectroscopy. *Appl. Phys. Lett.*, 76(19):2704, 2000.

[189] K. Szot, M. Rogala, W. Speier, Z. Klusek, A. Besmehn, and R. Waser. TiO_2-a prototypical memristive material. *Nanotechnology*, 22(25):254001, 2011.

[190] Na-Yeong Kim, Sang-Hyun Hong, Kang Jang-Won, NoSoung Myoung, Sang-Youp Yim, Suhyun Jung, Kwanghee Lee, Charles W. Tue, and Seong-Ju Park. Localized surface plasmon-enhanced green quantum dot light-emitting diodes using gold nanoparticles. *RSC Adv.*, 5(25):19624, 2015.

[191] Xuyong Yang, Pedro Ludwig Hernandez-Martinez, Cuong Dang, Evren Mutlugun, Kang Zhang, Hilmi Volkan Demir, and Xiao Wei Sun. Electroluminescence Efficiency Enhancement in Quantum Dot Light-Emitting Diodes by Embedding a Silver Nanoisland Layer. *Adv. Opt. Mater.*, 3(10):1439, 2015.

[192] Zhenyu Yang, Oleksandr Voznyy, Mengxia Liu, Mingjian Yuan, Alexander H Ip, Osman S. Ahmed, Larissa Levina, Sachin Kinge, Sjoerd Hoogland, and Edward H. Sargent. All-Quantum-Dot Infrared Light-Emitting Diodes. *ACS Nano*, 9(12): 12327, 2015.

[193] Mingxia Song, G Colas des Francs, and Alexandre Bouhelier. Influence of an Electron Beam Exposure on the Surface Plasmon Resonance of Gold Nanoparticles. *Plasmonics*, 9(2):343, 2014.

[194] D. B. Strasfeld, A. Dorn, D. D. Wanger, and M. G. Bawendi. Imaging Schottky barriers and ohmic contacts in PbS quantum dot devices. *Nano Lett.*, 12(2):569, 2012.

[195] Edward D. Palik. *Handbook of optical constants of solids*. Academic press, 1998.

[196] Philippe Guyot-Sionnest. Electrical Transport in Colloidal Quantum Dot Films. *J. Phys. Chem. Lett.*, 3(9):1169, 2012.

[197] Nicole Y. Morgan, C.A. Leatherdale, M. Drndić, Mirna V. Jarosz, Marc A. Kastner, and Moungi Bawendi. Electronic transport in films of colloidal CdSe nanocrystals. *Phys. Rev. B.*, 66(7):075339, 2002.

[198] D.S. Ginger and N.C. Greenham. Charge injection and transport in films of CdSe nanocrystals. *J. Appl. Phys.*, 87(3):1361, 2000.

[199] Moon Kee Choi, Jiwoong Yang, Kwanghun Kang, Dong Chan Kim, Changsoon Choi, Chaneui Park, Seok Joo Kim, Sue In Chae, Tae-Ho Kim, Ji Hoon Kim, Taeghwan Hyeon, and Dae-Hyeong Kim. Wearable red-green-blue quantum dot light-emitting diode array using high-resolution intaglio transfer printing. *Nature Commun.*, 6:7149, 2015.

[200] W.R. Holland and D.G. Hall. Frequency shifts of an electric-dipole resonance near a conducting surface. *Phys. Rev. Lett.*, 52(12):1041, 1984.

[201] Jiaming Hao, Jing Wang, Xianliang Liu, Willie J. Padilla, Lei Zhou, and Min Qiu. High performance optical absorber based on a plasmonic metamaterial. *Appl. Phys. Lett.*, 96(25):251104, 2010.

[202] Antoine Moreau, Cristian Ciracì, Jack J. Mock, Ryan T. Hill, Qiang Wang, Benjamin J. Wiley, Ashutosh Chilkoti, and David R Smith. Controlled-reflectance surfaces with film-coupled colloidal nanoantennas. *Nature*, 492(7427):86, 2012.

université PARIS-SACLAY | ÉCOLE DOCTORALE Ondes et Matière (EDOM)

Titre : Métamatériaux opto-électroniques

Mots clés : métamatériaux, boîtes quantiques colloïdales, nano-optique, LEDs à boîtes quantiques.

Résumé : Une nouvelle génération de dispositifs électroniques et optoélectroniques combinant hautes performances et bas coût se profile grâce aux promesses des film à boîtes quantiques colloïdales (BQCs) et de leurs propriétés électriques et optiques uniques. Les BQCs sont des nanocristaux semi-conducteurs synthétisés en solution qui se comportent comme des atomes artificiels. Des progrès considérables ont été réalisés durant la dernière décennie pour développer une optoélectronique à base de films BQCs mais les performances des composants réalisés sont toujours limitées par un certain nombre de propriétés propres à ces milieux telles que leur granularité et la présence de ligands à la surface des nanocristaux. Un deuxième type de matériaux artificiels, les métamatériaux, suscite un intérêt considérable de la part de la communauté de la nano-optique en raison des perspectives qu'ils offrent pour surmonter la limite de diffraction, réaliser des capes d'invisibilités et des indices de réfraction négatif en optique. Cependant, un certain nombre des applications potentielles des métamatériaux optiques se heurtent à leurs pertes élevées et au manque de fonctionnalités actives contrôlées électriquement.

Bien que les films BQCs et les métamatériaux soient étudiés de façon indépendante et associés à deux champs de recherche distincts, leurs propriétés ont beaucoup d'éléments en commun puisqu'elles sont dans les deux cas largement dictées par leur géométrie interne. Il paraît donc intéressant d'exploiter ces analogies et de voir si les difficultés rencontrées dans chaque discipline ne peuvent pas être surmontées en combinant les deux approches.

Cette thèse se propose de jeter les premiers ponts entre films BQCs et métamatériaux et constitue une première tentative d'établir une synergie entre ces deux types de milieux artificiels.

Dans un premier temps, nous étudions des réseaux de nanoantennes plasmoniques capables d'exalter la photoluminescence spontanée de BQCs et apportons de nouveaux éléments de compréhension à ces interactions. Ensuite, nous décrivons la fabrication et la caractérisation de LEDs à BQCs inorganiques et émission par le haut. Ces LEDs sont développées de façon à servir de plateforme pour la dernière partie de ce travail qui consiste à hybrider les films BQCs et les métamatériaux. Dans cette dernière partie, nous insérons les réseaux d'antennes plasmoniques étudiés précédemment dans l'architecture des LEDs et démontrons une nouvelle forme d'électroluminescence artificielle. Celle-ci se traduit par l'émission de lumière par des nanopixels discrets qui peuvent être arrangés de façon arbitrairement complexe afin de générer toute une gamme de fonctionnalités. D'autres avantages seront présentés comme une brillance accrue, une tension de seuil extrêmement basse, des longueurs d'ondes d'émission contrôlées par la géométrie et un contrôle total de la polarisation. Une série d'expériences visant à sonder les mécanismes à l'œuvre dans ce nouveau type de LEDs sera présentée.

Ce travail illustre le très grand potentiel qu'il y a à combiner différentes classes de matière artificielle et suggère que bien d'autres opportunités découleront d'une vision unifiée des différents milieux composites développés en physique, chimie et ingénierie.

Université Paris-Saclay
Espace Technologique / Immeuble Discovery
Route de l'Orme aux Merisiers RD 128 / 91190 Saint-Aubin, France